



Targeting Gold Nanoparticles Constructs in Colorectal Cancer

*Thesis submitted in accordance with the requirements of the
Middlesex University for the degree of Doctor in Philosophy by:*

Nakul Nautam Patel

(B.Sc., M.Sc., MRSB)

M00601162

Poster Presentation

Nakul Nautam Patel, Ivan Roitt, Lucy Ghali and Richard Bayford (2017)
Exploiting Gold nanoparticles in Colorectal Cancer. Summer Research
Conference, Middlesex University

Nakul Nautam Patel, Ivan Roitt, Lucy Ghali and Richard Bayford (2019)
Targeting Gold nanoparticles Constructs in Colorectal Cancer. Nanotechnology
Research Conference, Keele University

Publications

Nanoscale Advances (2021), Exploiting the efficacy of Tyro3 and Folate
receptors to enhance the delivery of Gold Nanoparticles into Colorectal Cancer
cells *in vitro*

IEEE (2021), Locating Functionalised Gold Nanoparticles using Electrical
Impedance Tomography

Acknowledgement

First and foremost, my deepest gratitude to my supervisors, Professor Richard Bayford, Professor Ivan Roitt and Associate Professor Lucy Ghali. I am truly honoured and privileged to have received their guidance, optimism and enthusiasm over the last 4 years, they have always helped me believe in myself to continually excel in the research.

I would also like to extend my support to Dr Leonardo Puntaja Munoz who has provided excellent technical knowhow in the project; especially the technical expertise on MALDI-TOF and ICP-OES analytical techniques.

I would also like to mention the hero of my world, my father; Nautambhai Rudabhai Patel, and my mother; Manishaben Patel, who had never let me feel discouraged throughout my life and without whose support I would not have reached this milestone. Secondly, my brother and sister-in-law who have provided the support at home no matter the weather.

I would also like to dedicate the thesis to my beloved wife who selflessly supported this venture. I owe it to all of them, without their support I could not have reached this far.

Lastly, I would like to mention my truest friends Fahimullah Hayat and Nirusha Weerasinghe. My friends had helped tremendously during my research at the university. I am glad to have met them in my life and words cannot express my sincere gratitude towards them. I am also grateful to have been supported by Dr Nick Kassouf who upon asking for help has never turned me down. Also, I would like to thank everyone who has in any way helped realise this goal in my life. I could not have done this without them!

Author's declaration

I, hereby, declare the research conducted in this thesis is my own work unless stated otherwise and at the time of submission is not being considered elsewhere for any other academic qualification.

Nakul Nautam Patel

20th December, 2020

Table of Contents

ABBREVIATIONS	10
TABLE OF FIGURES	14
1. INTRODUCTION	20
1.1 CARCINOGENESIS OF CRC	20
1.1.1 Chromosomal instability	22
1.1.2 Microsatellite instability	23
1.1.3 CpG island methylator phenotype (CIMP)	25
1.2 DIAGNOSIS AND SCREENING	26
1.3 TREATMENT AND LIMITATIONS IN CRC.....	30
1.3.1 Chemotherapy in CRC	30
1.3.2 Radiotherapy in CRC	32
1.4 GOLD NANOPARTICLES	34
1.4.1 Size	36
1.4.2 Delivery.....	37
1.4.3 Internalisation.....	40
1.4.4 Toxicity	41
1.5 GNPS AND CANCER	43
1.5.1 Folate receptors	44
1.5.2 Tyro3 receptors.....	46
1.6 GAP IN THE LITERATURE.....	49
1.7 RESEARCH AIMS AND OBJECTIVES.....	50
2.1 AIM	52
2.2 INTRODUCTION.....	53

2.3 TYRO3 AND FOLATE RECEPTOR-A MABS CONJUGATION TO GNPS.....	55
2.4 METHODS AND MATERIALS.....	58
2.4.1 Cell lines.....	58
2.4.2 Culture media	58
2.4.3 Cell passage.....	58
2.4.4 Cell counting	59
2.4.5 Fixation	59
2.4.6 Immunocytochemistry	59
2.4.7 Synthesis of Folate Receptor- α and Tyro3 conjugated Gold Nanoparticles.....	60
2.4.8 Ultraviolet visible (UV-Vis) spectroscopy.....	61
2.4.9 Stability assay	62
2.4.10 Dynamic light Scattering (DLS)	62
2.4.11 Matrix Associated Laser Desorption/Ionisation – Time of flight (MALDI-TOF) Mass spectrometry (MS)	63
2.4.12 Bradford assay	64
2.5 RESULTS	66
2.5.1 FR- α expression in CRL1790, CRL2159 and HCT116 cell lines	66
2.5.2 Tyro3 expression in CRL1790, CRL2159 and HCT116 cell lines	67
2.5.3 UV-Vis spectroscopy.....	67
2.5.4 Stability assay	70
2.5.5 DLS.....	72
2.5.6 MALDI-TOF.....	75
2.5.7 Bradford assay	76
2.6 DISCUSSION	78
2.6.1 Immunocytochemistry (ICC).....	78
2.6.2 UV-Vis spectroscopy.....	78
2.6.3 Stability assay	79

2.6.4 DLS	79
2.6.5 MALDI-TOF-MS analysis	80
2.6.6 Bradford assay	81
2.7 CONCLUSIONS.....	82
3.1 AIM	85
3.2 INTRODUCTION.....	85
3.3 METHODS AND MATERIALS.....	87
3.3.1 Cell culture	87
3.3.2 Uptake in CRL1790, CRL2159 and HCT116	87
3.3.3 Preparation of FITC labelled GNPs.....	87
3.3.4 ICP-OES	87
3.3.5 Confocal microscopy	88
3.3.6 Statistics.....	89
3.4 RESULTS	90
3.4.1 ICP-OES	90
3.4.2 Confocal microscopy	92
3.5 DISCUSSION	94
3.6 CONCLUSION	98
4.1 AIM	100
4.2 INTRODUCTION.....	100
4.3 TYPES OF 3D CULTURE MODELS	103
4.3.1 Anchorage-independent 3D cell culture	103
4.3.1a Hanging drop model and Ultra low attachment (ULA) plates	104
4.3.1b Magnetic levitation	105
4.3.2 Anchorage-dependent 3D cell cultures	106
4.3.2a Hydrogel.....	106
4.3.2b Microfluidic devices and micropatterned surfaces.....	107

4.3.2c Organotypic epithelial rafts.....	107
4.4 EXTRACELLULAR MATRIX IN CRC.....	109
4.5 CYTOKERATINS	111
4.5.1 Cytokeratins 7 and 20 in CRC.....	112
4.6 METHODS AND MATERIALS	115
4.6.1 Cell lines and cell culture.....	115
4.6.2 3D cell culture scaffold preparation	115
4.6.3 3D cell culture seeding	115
4.6.4 Histology	116
4.6.5 Hematoxylin and Eosin (H&E) staining.....	117
4.6.6 Characterisation of 3D models by Immunochemical staining	117
4.7 RESULTS	119
4.7.1 Hematoxylin and Eosin staining	119
4.7.1a Normal colon epithelium model (CRL1790)	119
4.7.1b CRC 3D model (CRL2159 AND HCT116).....	120
4.7.2 Characterisation of 3D cell models using Immunohistochemistry.....	121
4.7.2a CK7 expression in normal colon epithelium 3D model (CRL1790).....	121
4.7.2b CK7 expression in CRC 3D models (CRL2159 and HCT116).....	122
4.7.2c CK20 expression in normal colon epithelium (CRL1790).....	123
4.7.2d CK20 expression in CRC 3D models (CRL2159 and HCT116).....	123
4.8 DISCUSSION	126
4.9 CONCLUSIONS	129
5.1 AIM	131
5.2 INTRODUCTION.....	131
5.3 METHODS AND MATERIALS.....	132
5.3.1 3D cell culture	132
5.3.2 Uptake in normal vs. CRC models.....	132
5.3.3 ICP-OES	133

5.4 RESULTS	134
5.4.1 GNPs uptake in all normal vs CRC 3D models	134
5.4.2 Comparison of uptake between 2D and 3D models	135
5.5 DISCUSSION	138
5.6 CONCLUSIONS	141
6.1 DISCUSSION	143
6.2 CONCLUSIONS.....	147
6.3 FUTURE WORK.....	149
APPENDIX.....	150
BIBLIOGRAPHY	152

Abbreviations

3D and 2D	3 and 2 Dimension/Dimensional
3DCT	3-dimensional conformal radiotherapy
APC	Adenomatous Polyposis Coli
BM	Basement Membrane
CAP	Capecitabine
CIMP	CpG island methylator phenotypes
CIN	Chromosomal Instability
CK	Cytokeratin
CRC	Colorectal Cancer
CTAB	Cetyltrimethylammonium Bromide
CT-Scan	Computer Tomography Scan
DAB	3,3'-diaminobenzidine
DAPI	4', 6-diamidino-2-phenylindole
DCC	Deleted in Colorectal Cancer
DDED	Dead De-epidermalised Dermis
DHB	2, 5-Dihydroxybenzoic acid
DLS	Dynamic Light Scattering
DMEM	Dulbecco's Modified Eagle Medium
ECM	Extracellular Matrix
EDC	Carbodiimide
EGFR	Epidermal Growth Factor Receptors
ELISA	Enzyme Linked Immunosorbent Assay
EPCAM	Epithelial Cell Adhesion Molecule
EPR	Enhanced Permeability and Retention

FAP	Familial Adenomatous Polyposis
FBS	Fetal Bovine Serum
FIT	Faecal Immuno-Chemical Test
FITC	Fluorescein Isothiocyanate
FNIII	Fibronectin type III
FOBT	Faecal Occult Blood Test
FR- α	Folate Receptor – Alpha (α)
FS	Flexible Sigmoidoscopy
GNP/s	Gold Nanoparticle/s
GPI	glycosylphosphatidylinositol
GSK3	Glycogen Synthase Kinase-3
HCCA	α -Cyano-4-hydroxycinnamic acid
HLTF	Helicase – like Transcription Factor
HNPCC	Hereditary Non-Polyposis Colorectal Cancer
HPV	Human Papilloma Virus
HSV-1 / HSC-2	Herpes Simplex Virus type 1 and type 2
ICC	Immunocytochemistry
ICP-OES	Inductively Couple Plasma – Optical Emission Spectrometry
IFs	Intermediate Filaments
Ig	Immunoglobulin
IHC	Immunohistochemistry
KRAS	v-Ki-ras2 Kirsten rat sarcoma viral homolog
IRI	Irinotecan
LDH	Lactose Dehydrogenase
LOH	Loss of Heterozygosity

LS	Lynch syndrome
mAbs	Monoclonal Antibodies
MEM	Minimum Essential Medium
MINT	Methylated in Tumours
MMR	Mismatch Repair
MSI	Microsatellite Instability
MSI-L, MSI-H, MSI-S	Microsatellite Instability-Low/High/Stable
MTT	3-(4,5-dimethylthiazol-2-yl)-2,5-diphenyl-2H-tetrazolium bromide
-NH ₃	Amine group
NHS	<i>N</i> -hydroxy-succinimide
ODC	Polyamine Decarboxylase
OX	Oxaliplatin
PBS	Phosphate Buffer Saline
Pc 4	Phthalocyanine 4
PEG	Polyethylene Glycol
PFA	Paraformaldehyde
RES	Reticuloendothelial system
RME	Receptor Mediated Endocytosis
RUNX 3	Runt-related Gene 3
SA	Sinapinic acid
-SH	Thiol group
SPR	Surface Plasmon Resonance
TEM	Transmission Electron Microscopy
TIMP 3	Tissue Inhibitors of Metalloproteinase
TGF-β	Transforming Growth Factor-β

TSG	Tumour Suppressor Gene
ULA	Ultra Low Attachment
UV-Vis	Ultraviolet-Visible Spectroscopy
VEGFR	Vascular Endothelial Growth Factor Receptors
VZV	Varicella-Zoster Virus

Table of Figures

Figure 1: The figure depicts the CRC progression model in the Adenoma-Carcinoma Sequence. Molecular, genetic and epigenetic alterations drives the progression in CRC (Tariq et al., 2016).	21
Figure 2: Schematic representation of the binding of Wnt ligands leads to the transcription of the gene c-myc responsible for cell proliferation. Functional products of this gene, in turn, drives the transcription of proto-oncogene during carcinogenesis. Adapted from (Half, Bercovich and Rozen, 2009).....	23
Figure 3: Diagram shows progression of tumour through different stages of Colorectal Cancer (CRC) (Kannan, 2015).....	27
Figure 4: Figure demonstrates the Surface Plasmon Resonance of GNPs due to the oscillation of the electrons (Willets and Van Duyne, 2007).....	35
Figure 5: Figure shows biomedical applications of GNPs based on its physio-chemical, electrical and optical properties (Her, Jaffray and Allen, 2017).....	36
Figure 6: Figure describes the passive accumulation of the GNPs in to the tumour site due to enlarged gap junctions (100-600nm) between the endothelial cells of the blood vessels compared to same levels of administered drugs (Arvizo, Bhattacharya and Mukherjee, 2010).	38
Figure 7: Figure shows the EGFR antibodies bound to gold core using polyethylene glycol (PEG) as a bifunctional linker.....	39
Figure 8: GNPs internalisation via the RME pathway. Tumour specific-ligand binds to target moiety and leads to the formation of vesicles/endosomes which harbour the GNPs-drug complex. Acidic environment, along with other enzymes in the endosome denatures the bond between the drug and GNPs releasing the drug in the cell's cytoplasm (Cho et al., 2008)....	41
Figure 9: A) Structure of GPI proteins forming an anchor B) Enzymatic reaction linking FR- α to GPI-anchor via C-terminal signal peptide sequence in FR- α to ethanolamine on GPI-anchor protein. Adapted from (Sabharanjak and Mayor, 2004).	45
Figure 10: Figure shows two views of FR- α . FR- α has an overall globular structure. N and C termini are labelled (red boxes). Adapted from (Chen et al., 2013).	46
Figure 11: Structure and activation of TAM receptors. A) Shows the organisation of all the three domains; intracellular, transmembrane and extracellular. The conserved sequence is also highlighted in the kinase domain. B) All TAM receptor activation mechanisms i) ligand-independent dimerisation ii) ligand-dependent dimerisation iii) heteromeric dimerisation of two different TAM receptors iv) heterotypic dimerisation of TAM and non-TAM receptors and v) trans-cellular binding of extracellular domains. Adapted from (Linger et al., 2008)...	47
Figure 12: All three types of interaction between antibodies and Gold Nanoparticle's surface are shown in the figure. A) Hydrophobic bond B) Electrostatic or ionic bond and C) Covalent bond or dative biding (Jazayeri et al., 2016).....	54

Figure 13: Gold Nanoparticles attached with antibodies using EDC and NHS chemistry is shown in the figure above. A bifunctional linker such as Polyethylene Glycol (PEG) is used which has a –SH group on one end bound to the GNPs surface and a free –COOH group to bind antibody. EDC is reacted with –COOH group forming an O-Acylisourea intermediate. Secondly, NHS is reacted to form esters. Lastly, antibody or proteins containing amine group is added to form CONH (amide) covalent bond between antibody and GNPs (Jazayeri et al., 2016).	55
Figure 14: Schematic representation of the attachment of mAbs to GNPs is shown. GNP core is 5nm, PEG linker is ~15nm and mAbs ~7-10nm. Approximately 7 antibodies were attached per GNP after the conjugation step.	61
Figure 15: MALDI-TOF working principle is shown in the figure above. Samples are aliquoted on the allocated spaces on the target plate mixed with the matrix and allowed to dry. Laser beam is fired to create ionisation and desorption and to produce protonated ions. These ions then travels through the length of the tube and are detected via an ion detector (Patel, 2015).	64
Figure 16:- Figure shows the relative expression of FR- α in all three cell lines. DAPI stains the nucleus blue while FITC stains the FR- α membranous receptors in green. a) Colon Epithelium (CRL1790), b) Duke' B colorectal carcinoma (CRL2159) and c) Colorectal carcinoma (HCT116). Clear expression patterns can be seen of FR- α receptors being upregulated in CRL2159 and HCT116 compared to CRL1790. Scale bar = 50 μ m. Magnification 40X.	66
Figure 17:- Figure shows the relative expression of Tyro3 receptors in three types of cell lines. DAPI stains the nucleus blue while FITC stains the Tyro3 membranous receptors in green. a) Colon Epithelium (CRL1790), b) Duke' B colorectal carcinoma (CRL2159) and c) Colorectal carcinoma (HCT116). Clear expression patterns can be seen of Tyro3 receptors being upregulated in CRL2159 and HCT116 compared to CRL1790. Scale bar = 50 μ m. Magnification 40X.	67
Figure 18:- The UV-Vis (λ_{max}) peak of GNPs-PEG was at 513nm.	68
Figure 19:- The UV-Vis (λ_{max}) peak of GNPs-PEG-FR- α was at 517nm.	68
Figure 20:- The UV-Vis (λ_{max}) peak of GNPs-PEG-Tyro3 was at 517nm.	69
Figure 21: The UV-Vis (λ_{max}) peak of GNPs-PEG-(FR- α +Tyro3) was at 516nm.	69
Figure 22:- The stability of GNPs-PEG-FR- α in at different NaCl concentration solution (0.001M – 1M). No SPR red-shift observed.	70
Figure 23:- The stability of GNPs-PEG-Tyro3 at different NaCl concentration solution (0.001M – 1M).	71
Figure 24:- The stability of GNPs-PEG-(FR- α +Tyro3) at different NaCl concentration solution (0.001M – 1M). No SPR red-shift observed.	71

Figure 25: The size distribution profile of GNPs-PEG is shown. Most GNPs in this suspension are 22.97nm size (Polydispersity index (PDI) = 0.204).....	73
Figure 26:- The size distribution profile of GNPs-PEG-FR- α is shown. Most GNPs in this suspension are 30.78 nm size (Polydispersity index (PDI) = 0.231).....	73
Figure 27: The size distribution profile of GNPs-PEG-Tyro3 is shown. Most GNPs in this suspension are 31.76 nm size (Polydispersity index (PDI) = 0.225).....	74
Figure 28:- The size distribution profile of GNPs-PEG-(FR- α +Tyro3) is shown. Most GNPs in this suspension are 31.64 nm size (Polydispersity index (PDI) = 0.225).....	74
Figure 29: MALDI-TOF spectra for IgG as standard, GNPs-PEG, GNPs-PEG-FR- α and GNPs-PEG-Tyro3 is shown. High intensity peaks for IgG $[M+H]^+ = m/z$ 148,286, $[M+2H]^{2+} = 74,478$ and $[M+3H]^{3+}$ is seen. Spectra for GNPs-PEG-FR- α and GNPs-PEG-Tyro3 also shows similar peaks, however, they are absent in GNPs-PEG.....	75
Figure 30: MALDI-TOF spectrum for GNPs-PEG-(FR- α +Tyro3) also shows all three intensity peaks representative of IgG antibody.....	76
Figure 31:- The graph depicts the IgG concentration standard curve for the purpose of antibody quantification (range = 0 μ g/ml to 50 μ g/ml).....	77
Figure 32: Internalisation all 4 GNPs-constructs in CRL1790 cell lines. Internalisation is shown for each well. Experiments were done in triplicates (n=3). Error bars indicates SD. ANOVA = $p < 0.05$	91
Figure 33: Internalisation all 4 GNPs-constructs in CRL2159 cell lines Internalisation is shown from each well. Experiments were done in triplicates (n=3). Error bars indicates SD. ANOVA = $p < 0.05$	91
Figure 34: Internalisation all 4 GNPs-constructs in HCT116 cell lines Internalisation is shown from each well. Experiments were done in triplicates (n=3). Error bars indicates SD. ANOVA = $p < 0.05$	92
Figure 35: Figure shows the internalisation of GNPs-PEG-FR- α , GNPs-PEG-Tyro3 and GNPs-PEG-(FR- α +Tyro3) (red arrows) at 50ng in all three cell lines. Nuclei were stained in blue and GNPs in green. Experiments were repeated in triplicates (n=3). Scale bar = 50 μ m. Magnification 40X.....	93
Figure 36: - Schematic representation shows tumour and its interaction with surrounding microenvironment (Lovitt, Shelper and Avery, 2014).....	102
Figure 37: Figure shows the types of 3D cell cultures systems. Unlike 2D monolayer and 2.5D cell culture system, wherein cells are grown and cultured on top of thick layer of ECM, 3D models exhibits complex structures. Cells can be grown in spheroids (anchorage independent system) or seeded on the prefabricated 3D scaffolds (anchorage dependent). Moreover, spheroids in ECM scaffolds, microfluidics devices and micropatterned plates can	

together form a hybrid cell culture system that can offer advantages of both the systems to form a complex microenvironment for 3D cell culture (Langhans, 2018). 104

Figure 38: Four different techniques of developing spheroids are shown a) ultra-low adhesion (ULA) coated plates with a round bottom wells b) suspension of a droplet in a hanging drop model wherein the cells are self-aggregated and form spheroids c) Culture suspended in a bioreactor wherein the cells are self-aggregated forming spheroids and d) a random pillar in micropatterned plates where the cells are grown on the top of the pillar to form spheroids (Fang and Eglén, 2017). 105

Figure 39: Schematic representation of 3D models developed. DDED of the skin is used as a scaffold to grow and culture multiple layers of cells on top. 109

Figure 40: Schematic representation of the normal colon and CRC tissue. Top panels: Masson’s trichrome staining showing the connective tissue (blue), nuclei (red/purple), and cytoplasm (red/pink). Lower panel: Graphical scheme showing the transition of the normal colon (isotropic) mucosa to cancer (anisotropic) microenvironment (Crotti et al., 2017). ... 110

Figure 41: Figure shows an example of the 3D cell culture of the normal (CRL1790) and CRC (CRL2159 and HCT116) colon epithelium. Metal rings were placed on the top of the scaffold to affix the DDED in the well. 1×10^6 in $100\mu\text{l}$ were then seeded inside the ring and left in the incubator for optimum cell attachment to the dermis. 116

Figure 42:- Figure shows H&E staining of CRL1790 normal 3D model at 20X magnification. Cells have formed multilayers upon the scaffold as seen *in vivo* environment. Scale bar = $250\mu\text{m}$ 120

Figure 43: Figure shows H&E staining of CRL2159 (left) and HCT116 (right) 3D models at 20X magnification. Cells have formed multilayers upon the scaffold as seen *in vivo* environment. Scale bar = $250\mu\text{m}$ 120

Figure 44:- Focal expression of CK7 is shown in the normal 3D model. CK7 is expressed in the normal colon epithelium cells at 20X Magnification. Scale bar = $250\mu\text{m}$ 121

Figure 45: CK7 expression pattern was absent in CRL2159 Duke’s B 3D model. No DAB staining in the regions has been found. The image is shown at 20X magnification. Scale bar = $250\mu\text{m}$ 122

Figure 46: CK7 expression pattern was absent in the HCT116 Colorectal Carcinoma 3D model. No DAB staining in the regions has been found. The image is shown at 20X magnification. Scale bar = $250\mu\text{m}$ 122

Figure 47:- CK20 expression is positive and at higher level in the normal 3D model compared to CK7. Image is shown at 20X magnification. Scale bar = $250\mu\text{m}$ 123

Figure 48: Images shows the expression of CK20 in CRL2159 3D model at 20X magnification. A high level of DAB staining for CK20 is revealed in this model making it a potential 3D model for Colorectal Cancer. Scale bar = $250\mu\text{m}$ 123

Figure 49: Images shows the expression of CK20 in HCT116 3D models at 20X magnification. High levels of DAB staining for CK20 is revealed in this model making it a potential 3D model for Colorectal Cancer. Scale bar = 250µm.....	124
Figure 50: An example of GNPs aliquoting inside the O-ring placed on a CRC 3D model.	132
Figure 51: Internalisation efficiency of all GNPs constructs in normal and CRC 3D models (n=3). Name of the cell lines are mentioned that is representative of model developed using it. Error bars represents SD.....	134
Figure 52: Internalisation of all 4 GNPs constructs in normal 3D model vs CRL1790 2D monolayer of cells at 50ng. Error bars represents SD (n=3).....	136
Figure 53: Internalisation of all 4 GNPs constructs in CRC 3D model vs CRL2159 2D monolayer of cells at 50ng. Error bars represents SD (n=3).....	136
Figure 54: Internalisation of all 4 GNPs constructs in CRC 3D model vs HCT116 2D monolayer of cells at 50ng. Error bars represents SD (n=3).....	137
Figure 55: GNPs attachment study to plastic surface of 6-well plate. All GNPs were incubated for 4 h at 37 °C and in 5% CO ₂ in the absence of cells (p<0.05). Each sample in the well was processed through in a similar manner as with the cell sample. Error bars indicate SD. n=3	150
Figure 56: Aqua regia matrix effect study. ICP-OES detection of 50ng GNPs with and without aqua regia for all GNPs constructs. All GNPs were incubated for 4 h at 37 °C and in 5% CO ₂ in the absence of cells (p>0.05). Error bars indicate SD. n=3	150
Figure 57: All three cell lines A) CRL1790, B) CRL2159 and C) HCT116 from confocal microscopy is shown. The images represented as control for each cell line without any antibody-coated GNPs. The nuclei of the cell is represented in blue. Scale bar = 50µm. Magnification 40X.....	151

CHAPTER 1

Introduction

1. Introduction

Colorectal cancer (CRC) is the fourth most commonly diagnosed cancer around the globe and is characterised by the formation of malignant neoplasm in the mucosa of the colon and rectum (Cisterna *et al.*, 2016). CRC is one of the leading cause of morbidity and mortality worldwide. The average 5-year survival rate of a person diagnosed with colon and rectum cancer is 57% and 56%, respectively (Holleczek *et al.*, 2015). CRC does not correspond to a single pathological disorder but rather is a cumulative effect of heterogeneous malfunctions arising through mutations, epigenetic alterations, risk factors and inflammatory diseases (Yamauchi *et al.*, 2012). Moreover, the incidence of CRC rises rapidly with increase in age and, in particular, the incidence of the colon cancer is higher than the rectum in CRC (Young, Hobbs and Kerr, 2011). Nearly all CRCs arises from pre-existing benign polyps which can be surgically removed via endoscopic polypectomy preventing its further transformation into a malignant tumour. However, due to its asymptomatic nature, CRC is not diagnosed until very late (Gonzalez-Pons and Cruz-Correa, 2015). Adenoma polyps are the precursor lesions of advanced carcinoma in CRC and, thus, are a putative target for early treatment in CRC, if detected early. Also, development of CRC is manifested over the span of more than ten years; therefore such a period would provide ample amount of opportunities for early intervention making 5-year survival rate >90% (Bosch *et al.*, 2011).

1.1 Carcinogenesis of CRC

Carcinogenesis is a progressive multistep transformation of the benign dysplasia or adenoma into a malignant tumour or carcinoma in a process known as adenoma-carcinoma sequence (Young, Hobbs and Kerr, 2011). Carcinogenesis in CRC is driven by mainly three mechanisms, namely 1) Chromosomal instability (CIN) 2) Microsatellite instability (MSI) and 3) CpG island methylator phenotypes (Tariq *et al.*, 2016) (CIMP) (Figure 1).

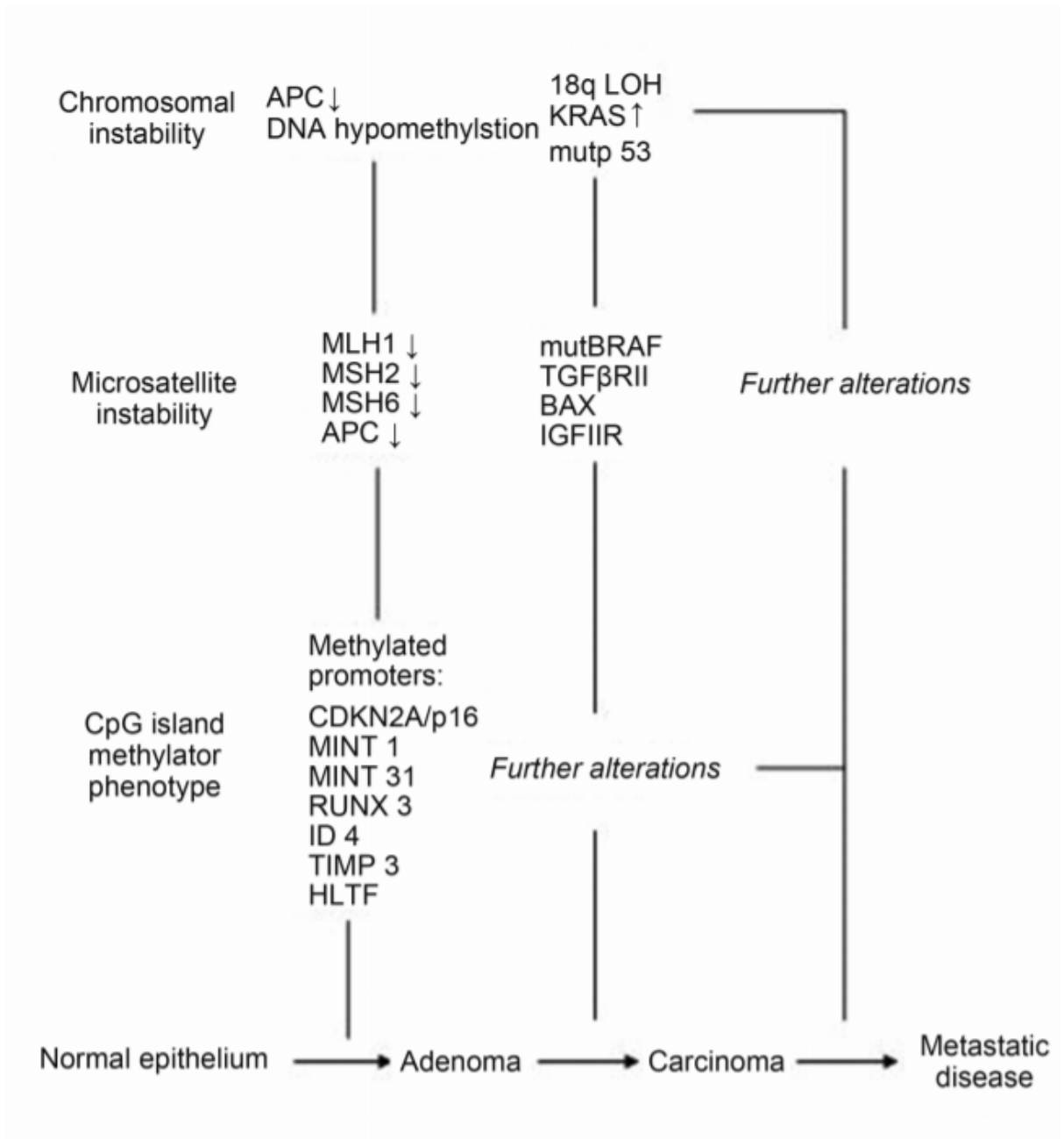


Figure 1: The figure depicts the CRC progression model in the Adenoma-Carcinoma Sequence. Molecular, genetic and epigenetic alterations drives the progression in CRC (Tariq et al., 2016).

1.1.1 Chromosomal instability

Chromosomal instability (CIN) refers to instability in genes or chromosomal arrangements; CIN accounts for 80%-85% of sporadic CRC. On the contrary, CIN involved in inherited Familial Adenomatous Polyposis (FAP), an inherited form of CRC, accounts only for 1% of all CRC. In either case, Adenomatous Polyposis Coli (*APC*) gene, a Tumour Suppressor Gene (TSG), located on the long arm of chromosome 5q2, is mutated/inactivated. FAP is an autosomal dominant disorder characterised by the formation of thousands of polyps or adenomas in rectum and colon during the second decade of life (Nugent and Phillips, 1992). CIN pathway, both in sporadic and inherited, follows the adenoma-carcinoma sequence beginning with a biallelic mutation in the *APC* gene leading to the development of benign polyps in the colon (Young, Hobbs and Kerr, 2011). *APC* help control cell proliferation and differentiation and plays a vital role in the Wnt-signalling pathway. *APC* regulates the expression of transcription factor β -catenin by its proteolytic degradation. In the presence of the Wnt ligand, expression of the β -catenin is mediated via glycogen synthase kinase-3 (GSK3)- conductin and β -catenin complex. This GSK-3-conductin- β -catenin complex targets the expression of *c-myc* in the nucleus which, in turn, activates the expression of polyamine decarboxylase (ODC), a proto-oncogene (Figure 2). However, in the absence of the Wnt ligand, *APC* binds to β -catenin for ubiquitin-mediated proteolytic destruction. Therefore, *APC* suppresses the activation of the downstream components preventing the transcription of the genes responsible for cell proliferation and differentiation in CRC (Half, Bercovich and Rozen, 2009).

Following *APC* mutation, activation mutation of proto-oncogene v-Ki-ras2 Kirsten rat sarcoma viral homolog (*KRAS*) and Deleted in Colorectal Cancer (*DCC*) further transforms benign neoplasm into the intermediary stage. *KRAS*, a member of mitogenic activated protein kinase (MAPK) pathway, is found mutated in 35% lesions of adenoma. Subsequently, progression from intermediate-stage to late-stage is driven by the loss of chromosome 18 (18q)

in the process called Loss of Heterozygosity (LOH). LOH of chromosome 18 is found in 60% of large adenomas and harbours two potential TSGs, SMAD family member 2 and 4 (*SMAD 2* and 4). Both TSGs are an innate part of Transforming Growth Factor- β (TGF- β) signalling pathway. Fully blown carcinoma transition from late-stage is committed by the loss of chromosome 17 (17q) harbouring tumour protein p53 (*TP53*). *TP53* is an important regulator in cellular stress and DNA damaging response and is found mutated in 50% of the cases (Young, Hobbs and Kerr, 2011).

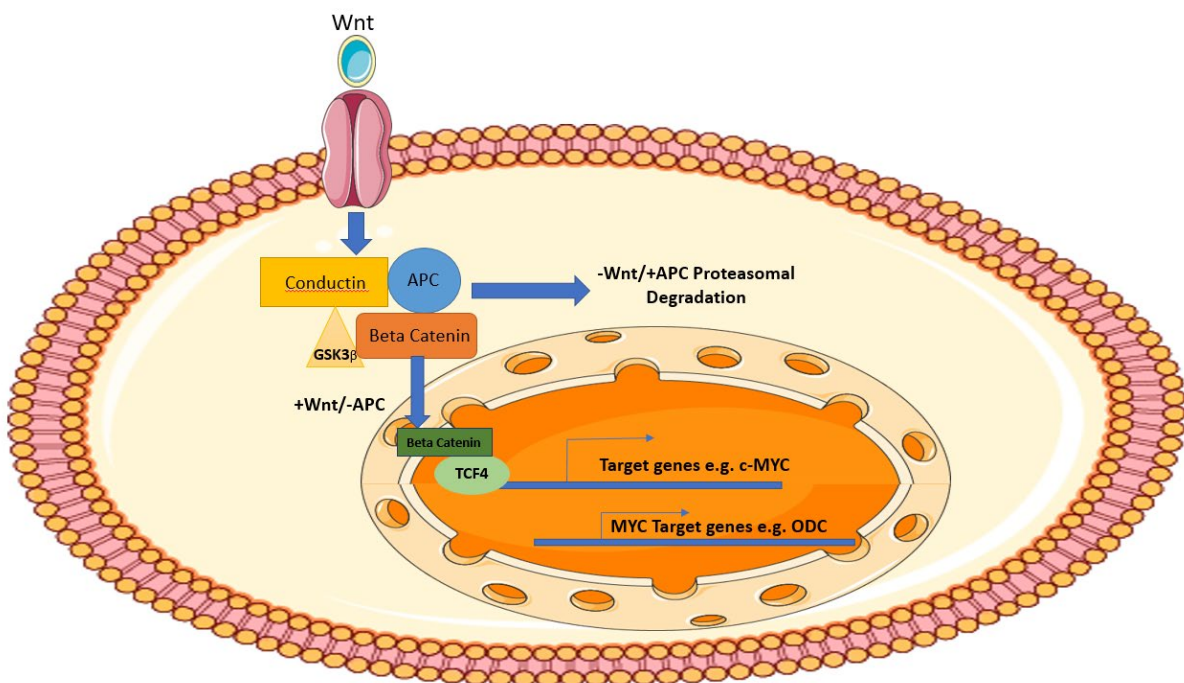


Figure 2: Schematic representation of the binding of Wnt ligands leads to the transcription of the gene *c-myc* responsible for cell proliferation. Functional products of this gene, in turn, drives the transcription of proto-oncogene during carcinogenesis. Adapted from (Half, Bercovich and Rozen, 2009).

1.1.2 Microsatellite instability

Microsatellite is the region in the chromosome with mono- and dinucleotide repeats. Microsatellite instability (MSI) is attributed to the inactivation mutation in DNA Mismatch Repair (MMR) genes. MMR proteins are involved in preserving the DNA fidelity by correcting

the mismatch/misincorporated nucleotides or base during DNA replication (Thomas, Umar and Kunkel, 1996). Inactivation of MMR genes increases the mutation rate in CRC mucosal cells by 100-fold (Thomas, Umar and Kunkel, 1996). The backbone of this mismatch repair system are the proteins hMSH2, hMSH6, hMSH3, hMLH1, hPMS2, hPMS1, and hMLH3 (Tariq *et al.*, 2016). Lynch syndrome (LS) or Hereditary Non-Polyposis Colorectal Cancer (HNPCC) have germline mutations in these proteins that makes a person predisposed to CRC. However, sporadic CRC with MSI arises due to hypermethylation in *MLH1* (Gonzalez-Pons and Cruz-Correa, 2015). MSI constitutes 10%-15% of sporadic CRC whereas hereditary Lynch syndrome accounts for only 3% of all CRC. Thus, most CRC with MSI are sporadic (de la Chapelle and Hampel, 2010). In 1997, National Institute of Cancer authorised BAT25, BAT26, D5S346, D2S123, and D17S250 as markers that would confirm the presence and extent of MSI in CRC. If it is $\geq 30\%$ then it is characterised as MSI-high (MSI-H), if $\leq 30\%$ then MSI-low (MSI-L) and if MSI is not present at all then the condition is MSI-stable (MSI-S) (Boland *et al.*, 1998).

There are more than 1500 germline variation found in MMR genes in addition to promoter hypermethylation, somatic deletions and point mutation (Tariq *et al.*, 2016). Additionally, EPCAM (Epithelial Cell Adhesion Molecule), located upstream of MSH2, have also been found commonly mutated in HNPCC. The mutation is at the 3' end of the *EPCAM*. The mutation silences the 3' end which harbours the stop signal for the gene. As a result, *MSH2* is also transcribed along with the transcription of *EPCAM* producing a long strand of mRNA. (Niessen *et al.*, 2009). *BRAF* mutations were also shown in 40%-50% MSI-H sporadic CRC which are not present in MSI arising in inherited LS. Thus, *BRAF* mutation can be used to differentiate between sporadic and hereditary CRC (Gonzalez-Pons and Cruz-Correa, 2015). Table 1 shows genetic alterations of the oncogenes and TSGs in sporadic CRC.

Table 1: Table shows the oncogenes and TSGs involved in sporadic CRC (Young, Hobbs and Kerr, 2011)

GENE NAME	TYPE OF GENE	FREQUENCY OF MUTATION OR EPIGENETIC SILENCING	RESULTS
<i>APC</i>	TSG	~70%	Activation of Wnt signalling pathway
<i>BRAF, KRAS</i>	Oncogene	~10%, ~35%	Activation of MAPK pathway
<i>SMAD2 & 4, TGFBR2</i>	TSGs	~5%, ~10%, ~15%	Decreased TGF- β signalling
<i>TP53</i>	TSG	~50%	Impaired cellular stress and DNA damage response
<i>MLH1, MSH2, MSH6, PMS2</i>	Mutator Gene	~10%	Defective in mismatch repair pathway

1.1.3 CpG island methylator phenotype (CIMP)

CRC tumours also shows the tendency of promoter hypermethylation of the CpG islands thereby silencing the gene in an epigenetic event. CpG are short tandem dinucleotide repeats constituting of cytosine and guanine bases and are found in 5' region of approximately 50% of the human gene-pool (Bird, 1986). Hypermethylation of CpG islands leads to transcription inactivation of the gene as seen for *MLH1* promoter and is correlated with *BRAF* V600E mutation (Tariq *et al.*, 2016). In this type of pathogenesis, the chromosomal karyotype is normal (Young, Hobbs and Kerr, 2011). According to the varying degree of hypermethylation, the subgroup of people diagnosed with CIMP are represented differently in clinical perspective and are attributed to 'epigenetic instability'. Unlike MSI markers, however, markers of hypermethylation or CIMP are still not unanimous amongst the pioneers in the field and are also categorised differently (Tariq *et al.*, 2016).

1.2 Diagnosis and screening

Survival of the patients depends upon the grade and staging of the CRC upon diagnosis. According to the Duke's classification, if a patient is diagnosed with CRC in Duke's A stage, then the probable survival rate of the patient for 5 year or more is >90%. On the other hand, if during the diagnosis CRC was found to be in the last stage, Duke's D Colorectal Cancer, the probability for 5 year survival is reduced to <5% (Figure 3) and (Table 2) (Young, Hobbs and Kerr, 2011). One such test is the faecal occult blood test (FOBT) that detects subtle levels of pseudoperoxidase activity in haem of the faeces/stool from adenomatous lesions. Thus, the presence of occult blood from neoplasm (Osborn and Ahlquist, 2005). FOBT is non-invasive and inexpensive and thus can be used during screening. However, sensitivity (50%-60%) and specificity of FOBT is low and does not include lymph node and distant metastasis making it unreliable for the detection of CRC (Osborn and Ahlquist, 2005). Additionally, a false positive result can also be seen, as FOBT result can be affected by the food intake for e.g. beet root, meat and other substances that contain haem (Mandel *et al.*, 1993).

Table 2: Duke's Classification of CRC based upon tumour, lymph nodes involvement and distant spread of tumour or metastasis using Tumour, Nodes and Metastasis (TNM) system (Young, Hobbs and Kerr, 2011).

TNM Stage	Duke's Stage	Prognosis
T1N0M0	Duke's A	5 year survival >90%
T2N0M0		
T3N0M0	Duke's B	5 year survival 70%-85%
T4N0M0		5 year survival 55%-65%
Any T, N1M0	Duke's C (C1 if apical node negative)	5 year survival 45%-55%
Any T, N2M0	(C2 if apical node positive)	5 year survival 20%-30%
Any T, any N, M1	Duke's D	5 year survival <5%

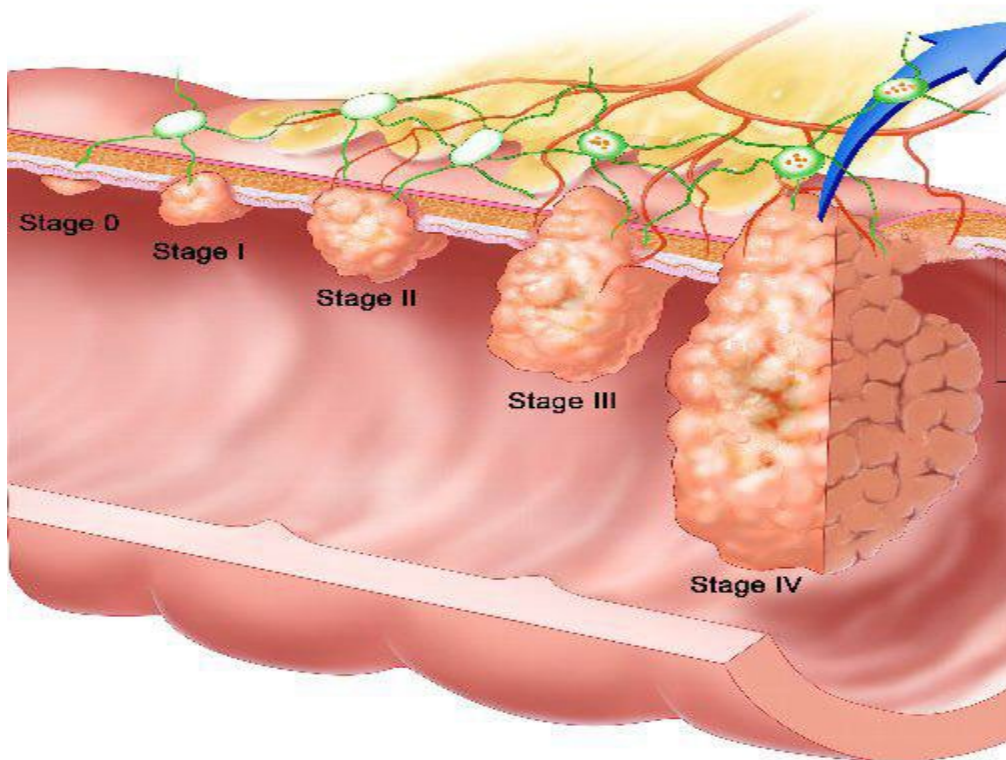


Figure 3: Diagram shows progression of tumour through different stages of Colorectal Cancer (CRC) (Kannan, 2015).

Likewise, the Faecal Immuno-Chemical (FIT) test detects blood in the faeces to detect CRC but using Enzyme Linked Immunosorbent Assay (ELISA) (Chan *et al.*, 2017). Its use, however, cannot detect CRC in its early stages (De Maio *et al.*, 2014). Regardless, if the test comes positive, for FOBT or FIT, further invasive or semi-invasive procedures such as Flexible Sigmoidoscopy (FS) and Colonoscopy are recommended to precisely locate the lesions in the colon. Direct visualisation of the distal colon (sigmoid colon and rectum) is done via FS. However, the drawback of the FS is that it is limited to the left region of the colon, and, therefore, the polyps in the transverse colon and above are not detected (Young, Hobbs and Kerr, 2011). Similarly, colonoscopy allows full optical endoscopy of the colon and is regarded as the ‘gold standard’ approach in detecting early cancer. Nevertheless, it has numerous drawbacks. First, optimum operational capability of colonoscopy is limited to the competency

of its user. It is also expensive and invasive in nature requiring bowel treatment prior to colonoscopy. Bowel laxative preparation occasionally induces perforation on the walls of the colon. Therefore, due to the asymptomatic nature of the colon, by the time CRC is detected, it will have grown into stage Duke's C or Duke's D where the mortality rate is above 95% (Chan *et al.*, 2017). Hence, it is imperative to investigate an alternative method for the purpose of CRC treatment.

Table 3: Limitations of procedures used for diagnosing and screening for CRC (Wolf *et al.*, 2018).

TESTS	ADVANTAGES	LIMITATIONS
Faecal Occult Blood Test (FOBT)	<ol style="list-style-type: none"> 1) Non-invasive 2) No bowel preparations 3) Low cost 	<ol style="list-style-type: none"> 1) Low sensitivity (50%-60%) 2) Needs to be performed multiple times 3) Requires confirmation via colonoscopy if found positive 4) Can produce false-positive results 5) A strict diet plan needs to be followed
Faecal Immunochemical Test (FIT)	<ol style="list-style-type: none"> 1) Low cost 2) No bowel preparations required and Non-invasive 3) Better sensitivity than FOBT (73%-88%) 	<ol style="list-style-type: none"> 1) Fails to detect early adenomatous lesions 2) Requires confirmation via colonoscopy if found positive
Flexible Sigmoidoscopy	<ol style="list-style-type: none"> 1) High performance of CRC detection in lower 1/3 of the colon and rectum 2) Minimal bowel preparations 3) Biopsies and polyps can be removed 	<ol style="list-style-type: none"> 1) Unable to detect any early lesions of CRC in the upper part of the colon. 2) Less harmful than colonoscopy in bowel preparation
Colonoscopy	<ol style="list-style-type: none"> 1) Gold standard approach with >90% sensitivity and specificity 2) Allows the visualisation of entire colon 3) Biopsies and polyps can be removed 	<ol style="list-style-type: none"> 1) Requires sedation and extreme bowel preparations 2) Can cause perforation in the wall of the bowel
Computer Tomography (CT) Colonoscopy	<ol style="list-style-type: none"> 1) Minimally invasive 2) Good sensitivity (75%-93%) 3) Oral contrast agents needs to be consumed 	<ol style="list-style-type: none"> 1) Dietary restriction needs to be followed 2) Biopsies or polyps cannot be removed

1.3 Treatment and Limitations in CRC

Treatment of CRC, in most cases, is ineffective using single modality of treatment. Upon detection of CRC, the conventional way of treating it is a neo-adjuvant chemoradiotherapy followed by surgery and adjuvant chemotherapy depending on the stage/grade of the tumour. Chemotherapy, however, has considerable side-effects due to improper pharmacokinetics, failure of drug retention by the tumour and unwanted toxicity (Akhter *et al.*, 2011). Radiation, on the other hand, is unable to prevent loco-regional recurrences and some cancers develop innate resistance towards it. Neither of the strategies has shown a positive outcome without manifesting systematic cytotoxicity or survival benefit (Ku and Ilson, 2009). Additionally, the results of the surgery too are not noteworthy as it relies on radiotherapy and/or chemotherapy for its success. Hence, the need to develop a personalised tailor-made therapy specific for CRC remains indispensable (Singh *et al.*, 2015).

1.3.1 Chemotherapy in CRC

Considerable progress has been made in the last two decades in the treatment of malignant CRCs. As a result, the average progression-free survival (PFS) has increased from 9 months to 24 months (Wolpin and Mayer, 2008). Currently, chemotherapy involves the use of single drug, mainly fluoropyrimidine (5-FU), as well as it is used in combination with multiple regimens such as oxaliplatin (OX), irinotecan (IRI), and capecitabine (CAP or XELODA or XEL) to treat CRC (Seymour *et al.*, 2007). Amongst the combined regimens used for CRC treatment, FOLFOX (5-FU+OX), FOXFIRI (5-FU+IRI), XELOX OR CAPOX (CAP+OX) and CAPIRI (CAP+OX) are currently being used as first line of treatment (Xie, Chen and Fang, 2020). Nonetheless, chemotherapy is limited by poor specificity, improper biodistribution, drug resistance and dose-limiting cytotoxicity (Gu *et al.*, 2007; Hong and Rao, 2019). Additionally, treatment for liver metastases in CRC is also not curable (Hong and Rao, 2019). Despite this, chemotherapy still remains the cornerstone in the treatment of CRC (Cassidy *et al.*, 2004). Furthermore, conventional chemotherapeutic drugs, like paclitaxel,

target solely proliferating cells and cannot distinguish between normal and cancer cells (Volk-Draper *et al.*, 2014). Also, it is unable to target quiescent cancer stem cells from which a new cancer cell re-generates. On the contrary, cyclophosphamide accomplishes both aims but multidrug resistance develops due to impaired biological pathways and mutations in the genes (Chen *et al.*, 2012; Tazawa *et al.*, 2014). Moreover, 5-FU can exhibit fewer side-effect at lower dose but for 5-FU to be effective, high dose needs to be applied. However, at high dosage 5-FU shows systematic toxicity and chemotherapy resistance (Debucquoy *et al.*, 2009).

These multidrug resistant and latent cancer stem cells will subsequently cause relapse. Such erratic nature of the drugs not only generates cytotoxic effect in the body for e.g. bone marrow suppression, nausea, vomiting and neurotoxicity but also renders remission or overall survival short-lived due to drug resistance in the tumour (Liu, Lv and Yang, 2015). Therefore, to effectively curb the tumour, CRC is treated with a plethora of chemotherapeutic drugs such as capecitabine, irinotecan, oxaliplatin, fluorouracil, leucovorin as well as targeting drugs such as bevacizumab as first line of defence (Geißler *et al.*, 2017). Nevertheless, most CRCs are diagnosed at TNM stage IV or Duke's D stage where chemotherapy cannot offer much assistance. Hence, together with toxicity, non-specificity and advanced tumour stage chemotherapy is limited in CRC. Table 4 shows chemotherapeutic drug's functions and limitations in CRC. To circumvent this problem, GNPs can be used as an alternate strategy since it offer considerable advantages over chemotherapy and can evade all the aforementioned drawbacks (Barui *et al.*, 2014).

Table 4: Functions and limitations of the chemotherapeutic drugs used in CRC treatment.

DRUGS	FUNCTIONS	LIMITATIONS/SIDE EFFECTS	REFERENCES
5-Fluorouracil with Leucovorin	To inhibit the function of thymidylate synthase and DNA metabolite incorporation	Neutropenia, stomatitis, diarrhoea, drug resistance due to enhanced thymidylate synthase activity	(Geißler <i>et al.</i> , 2017)
Oxaliplatin, Carboplatin, Cisplatin	Incorporation of DNA platinum adducts	Hypertension, paresthesias of hand & feet	(Wolpin and Mayer, 2008) and (Stojanovska, Sakkal and Nurgali, 2015)
Irinotecan	To inhibit Topoisomerase-I activity	Diarrhoea, myelosuppression and alopecia (Hair-loss)	(Rougier <i>et al.</i> , 1998)
Bevacizumab (Avastin®)	To inhibit angiogenesis via VEGF	Hypertension and proteinuria and drug resistance due to mutations in <i>BRAF</i>	(Wolpin and Mayer, 2008)
Cetuximab (Erbix®) and panitumumab (Vecitibix®)	To inhibit proliferation and differentiation via EGFR	Skin rash or redness or blistered skin, diarrhoea, pulmonary toxicities etc, and drug resistance due to mutations in <i>KRAS</i> & <i>NRAS</i>	(Bardelli and Siena, 2010)

1.3.2 Radiotherapy in CRC

The use of radiotherapy, with/without chemotherapy, is being used to treat more than 50% of the patients suffering from cancer or as a palliative treatment (Delaney *et al.*, 2005). Radiotherapy can be delivered via two methods 1) short-course preoperative radiotherapy and 2) chemoradiation. The former delivers 25Gy of radiation intermittently in 5 fractions over 1 week period whereas latter gives 45Gy in 25 fractions over 5 weeks with chemotherapy (Hatcher and Kumar, 2014). Radiotherapy employs the use of ionising radiation in the form of X-rays or γ -rays; externally or internally. External radiation can be delivered by linear

accelerators such as external beam for e.g. 3-dimensional conformal radiotherapy (3DCT) that implements left, right and posterior field. Such radiation therapy conforms to the shape and volume of the tumour allowing maximum radiation dosage to the tumour whilst keeping it minimum to the normal cells. It is used mainly on medium risk, locally advanced and inoperable rectal cancers (Tam and Wu, 2019). Another example of external radiation is intensity modulated radiotherapy which help monitors the dosage of radiation applied to a specific area (Kaufman *et al.*, 1989; Hatcher and Aswin A Kumar, 2014). On the contrary, in an internal radiation therapy, a radioisotope or a rectal implant is inserted and placed near the tumour e.g. brachytherapy (also known as endorectal brachytherapy), which constantly emits radiation to eliminate the cancer cells (Kaufman *et al.*, 1989; Her, Jaffray and Allen, 2017). Continuous exposure to ionising radiation induces cellular damage, especially in the DNA, via the generation of free radicals. Radiotherapy although effective in controlling the tumour growth also affects normal tissue surroundings. As a consequence, the radiation dosage needs to be kept to a level where it does not induce toxicity to the normal cellular environment (Her, Jaffray and Allen, 2017).

Extensive progress has been made in targeting cancer cells using radiation modality (Kaliberov and Buchsbaum, 2012). However, due to radiation-resistance of the tumour cells and radiation-induced toxicity on normal cells, it remains an obstruction in treating the cancer. Development of resistance to therapeutic doses can be of two types; 1) innate resistance and 2) acquired resistance. Innate resistance is the in-built resistance of the tumour to therapeutic doses of radiation whilst acquired resistance is procured secondary to the radiation treatment (Shimura, 2011). Therefore, combination therapy of drugs and radiation are given which offers the best treatment by far by exploiting all the biological pathways in destroying the cancer cells. Toxicity to normal tissue surrounding the tumour has also limited the doses of radiation being delivered to the tumour. An example is the use of radiotherapy in treating cancer in

abdominal cavity and pelvis; colon and small bowel or rectum have also been subjected to normal tissue toxicity solely due to the location (Goitein, 2009). Additionally, radiotherapy-associated acute and chronic toxicities are also imposed on the normal tissue surroundings. Such toxicities include chronic bowel perforation, obstruction, strictures, malabsorption, increased bowel frequency and incontinence (Hatcher and Kumar, 2014). Other than these, infertility, erectile dysfunction, and delayed wound healing are some of the side effects also associated with radiotherapy (Marijnen *et al.*, 2002). Another limitation 3DCT is organ motion, volume invariability and dose invariability giving potentially suboptimal dosage to the tumour. More trials are currently underway to circumvent this problem and to determine its clinical benefits that outweighs its side effects (Arbea *et al.*, 2010). Therefore, a greater need of novel treatment arises that specifically targets the cancer cells whilst keeping the toxicity to minimum in normal cells or tissue.

1.4 Gold nanoparticles

Nanotechnology was first defined by the Nobel prize winner Richard Feynman in 1959 (Feynman, 1959). In Greek, 'nano' means 'dwarf' and refers to the particle size equivalent to 10^{-9} m. Therefore, the term Gold Nanoparticles (GNPs) refers to as particles of gold (Au) atoms in the range of 10^{-9} meters (Grobmyer, Iwakuma *et al.* 2010). GNPs are non-toxic to the cells as the core of the GNP is inert (Lévy *et al.*, 2010) and are also biocompatible with cells and tissues (Mukherjee, Bhattacharya and Mukhopadhyay, 2006). GNPs have a unique physicochemical feature of making thiol and amine bonds and, therefore, can interact and modified with wide arrays of organic materials, enzymes and proteins (Bhattacharya *et al.*, 2007). GNPs can be characterised easily via intrinsic surface plasmon resonance (SPR) property which refers to the collective oscillation of the electrons by absorbing photons from the visible spectrum at a specific wavelength and emitting the energy in relation to the size and shape of GNPs (Figure 4) (Daniel and Astruc, 2004). Hence, monitoring the therapy, imaging,

drug delivery, biomedical imaging, as a contrast agent, diagnosing and excessive heat therapy in cancer can be possible (Figure 5) (Singh *et al.*, 2015). Additionally, gold-based compounds possess anti-inflammatory properties and, hence, have since been in use to treat rheumatoid arthritis (e.g. Auranofin[®] and Tauredon[®]) (Finkelstein *et al.*, 1976; Berners-Price and Filipovska, 2011). GNPs also come in different shapes and sizes such as spheres, nanorods, star-shapes, nano-urchins, nano-belts, nano-cages, nano-prisms, nano-stars, hexagonal etc (Cai *et al.*, 2008).

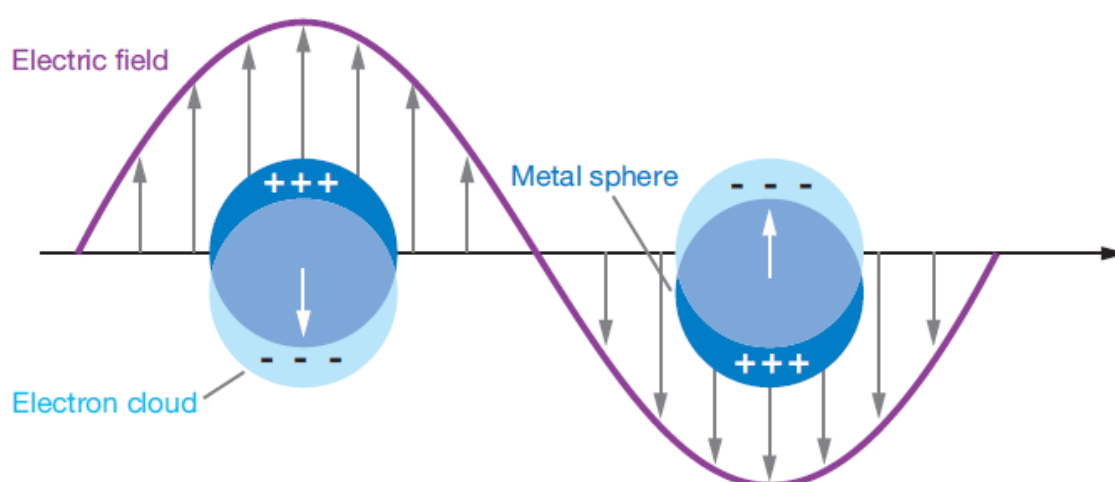


Figure 4: Figure demonstrates the Surface Plasmon Resonance of GNPs due to the oscillation of the electrons (Willels and Van Duyne, 2007).

Synthesis of GNPs was first shown by Michael Faraday in the scientific paper, where it was demonstrated that the artificial production of colloidal gold could be achieved by reduction of aurochloric acid (HAuCl_4) by phosphorous. GNPs so synthesised are highly stable since they still present in the solution proving their high stability. This was further supplemented by new advents of the 20th century, wherein the technologies such as Transmission Electron Microscopy (TEM) and Atomic Force Microscopy enabled direct visualisation of GNPs (Turkevich, Stevenson and Hillier, 1951). Due to its application as nanomedicine in cancer, GNP's current research is focused on GNP uptake/internalisation,

subcellular localisation, excretion from the cell and, subsequently, excretion from the whole organism (Dykman and Khlebtsov, 2014).

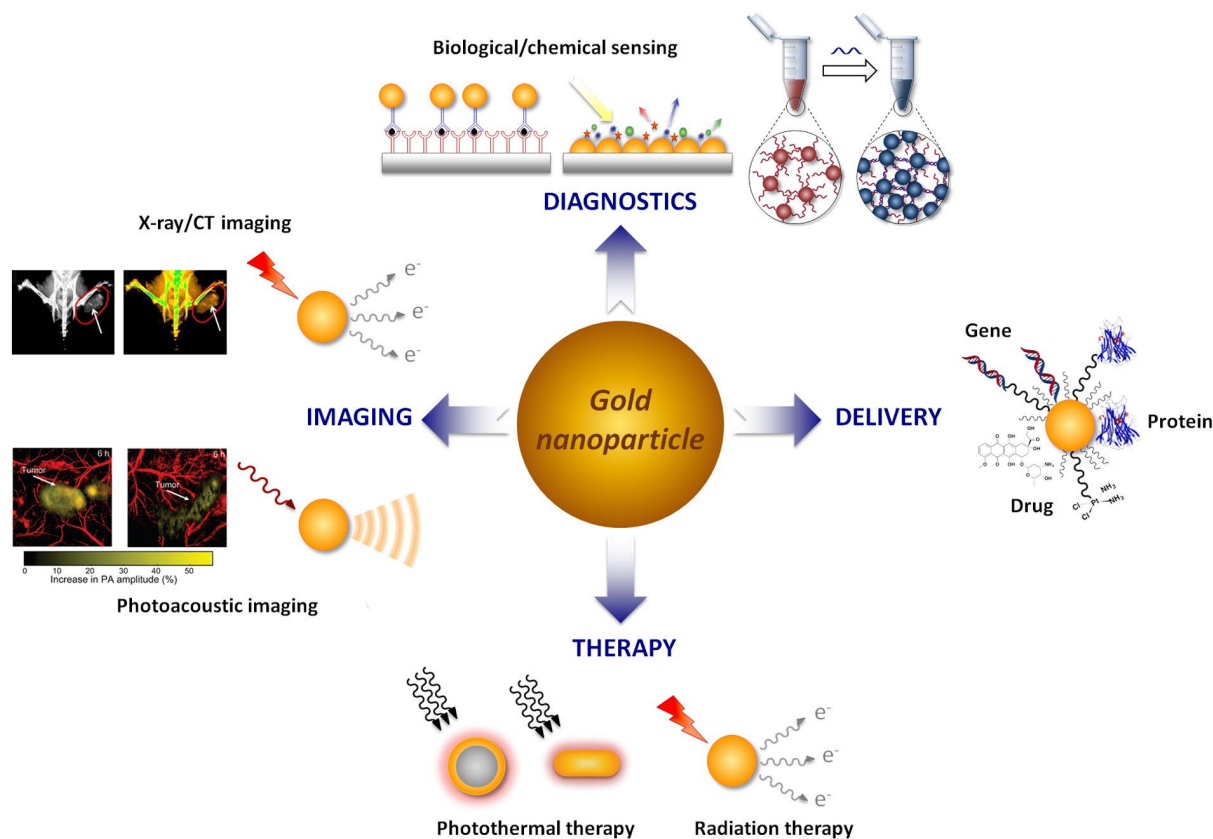


Figure 5: Figure shows biomedical applications of GNPs based on its physio-chemical, electrical and optical properties (Her, Jaffray and Allen, 2017).

1.4.1 Size

As mentioned before, the inorganic core of the GNPs possesses a crucial role in the biomedical application such as sensing, imaging, and drug delivery. Their success is dependent on its target specificity and followed by successful internalisation in the cell. On this basis, it was demonstrated that the size and shape of GNPs play a vital role in cellular uptake *in vitro*. Spherical gold nanoparticles have been shown to have more uptake efficiency compared to gold nanorods. In a study to investigate GNPs internalisation in HeLa cell line, it was demonstrated that the uptake of gold nanospheres were 3 to 6 times higher than that of gold nanorods (Chithrani, Ghazani and Chan, 2006). In the same study, it was shown that 50nm GNPs have the highest internalisation efficiency compared to 14nm, 30nm, 74nm and 100nm

GNPs nanospheres and 40 x 14 nm and 74 x 14 nm gold nanorods (Chithrani, Ghazani and Chan, 2006). However, the GNPs so used in the study were capped with citrate and cetyltrimethylammonium bromide (CTAB) surfactants and were not targeted using a specific antibody. Moreover, the plasma membrane is a semi-permeable membrane and allows only diffusion of small and non-polar molecules. As such, bigger molecules like GNPs cannot traverse unless specific ligand is used against a receptor in a process called endocytosis (Doherty and McMahon, 2009). Hence, it was concluded that due to the adsorption of the proteins in the culture media onto GNP's surface, GNPs were internalised in the cell via endocytosis (Dykman and Khlebtsov, 2014).

1.4.2 Delivery

For GNPs to be successful in cancer clinical trials, it needs to reach the tumour's primary, and if possible, its secondary metastatic site after systemic administration. This delivery of the GNPs to tumours is a multistep process (Lund *et al.*, 2011). GNPs can reach a tumour via two different ways; active and/or passive targeting. These can be modified to improve the GNPs delivery to a tumour. Due to its nanometre size, GNPs can exploit certain features of the tumour. As such, due to improper angiogenesis, poor alignment of the endothelial cells and leaky blood vessels in the tumours, GNPs can sequester and tend to accumulate in tumours through wide fenestrations (100-600nm). These pores are usually 5nm-10nm in normal vasculature (Wang, Langer and Farokhzad, 2012). This is called the enhanced permeability and retention (EPR) effect (Maeda, 2001). Simultaneously, lymphatic vessels are also poorly developed and, thus, are not able to draw the waste away from a growing tumour. Hence, GNPs preferentially accumulate in a tumour due to enlarged gap junction between endothelial cells via extravasation 10 times more than levels of same administered dosage of free drug (Figure 6) (Arvizo, Bhattacharya and Mukherjee, 2010). Together with the EPR effect, this feature constitutes passive targeting in cancer (Choi *et al.*, 2010).

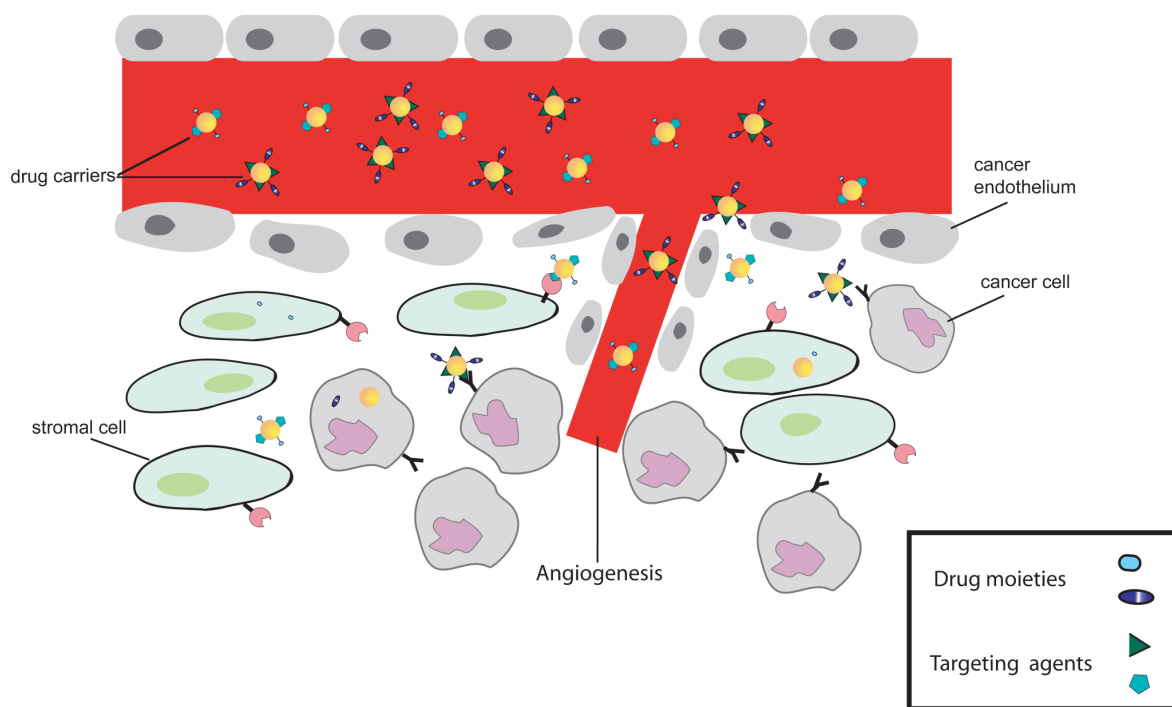


Figure 6: Figure describes the passive accumulation of the GNPs in to the tumour site due to enlarged gap junctions (100-600nm) between the endothelial cells of the blood vessels compared to same levels of administered drugs (Arvizo, Bhattacharya and Mukherjee, 2010).

After GNP's diffusion from the blood vessel, GNPs needs to reach to the tumours core/lumen and has to bypass the interstitial network of collagen and adhesion molecules. Lastly, it will have to get internalised by the cancer cells and deliver the diagnostic or therapeutic payload according to the GNP's modification. Data in recent years implicates that GNPs with a hydrodynamic diameter less than 10nm can penetrate intestinal barriers that are between the tumour core and blood vessels (Baish *et al.*, 2011; Wong *et al.*, 2011). GNPs with 10nm or less hydrodynamic diameter have entirely different physicochemical/thermodynamic properties compared to GNPs larger than 10nm due to their larger surface area-to-volume ratio (Baish *et al.*, 2011). Once inside the body, GNPs also need to be excreted like any other metabolites. It has been known that GNPs with less than 6nm (including gold core and attached ligands) can be excreted via glomerular capillary walls in the kidney (Bayford *et al.*, 2017).

Active targeting, on the other hand, allows direct targeting of the cancer cells. Non-specific drug interaction is primarily responsible for limiting its efficacy. This sub-optimal efficiency can be circumvented by attaching antibodies or ligands to the GNPs that can be directed towards neoplastic cells and prevent its uptake in normal cells (Allen, 2002) (Figure 7). For e.g., GNPs internalisation efficiency was tested using epidermal growth factor receptor (EGFR) antibody in HaCaT (normal human keratinocytes) and HOC 313 clone 8 and HSC 3 (human oral squamous cell carcinoma). It was demonstrated that anti-EGFR antibody bound GNPs had been internalised 600% and 700% more in HOC and HSC cancerous cell lines compared to HaCaT (El-Sayed, Huang and El-Sayed, 2005). Thus, it is possible to target the cancerous cells while keeping the uptake to normal cells to a minimum. Over and above, due to GNPs physicochemical properties, pharmacokinetics and biocompatibility, it is an emerging tool in targeting cancer. These characteristics can be attributed to its easy manipulation of shape and size, colloidal stability, larger surface-to-volume ratio, conjugation to different ligands, peptides, antibodies, proteins, drugs, DNA etc (Cabral, Baptista 2014).

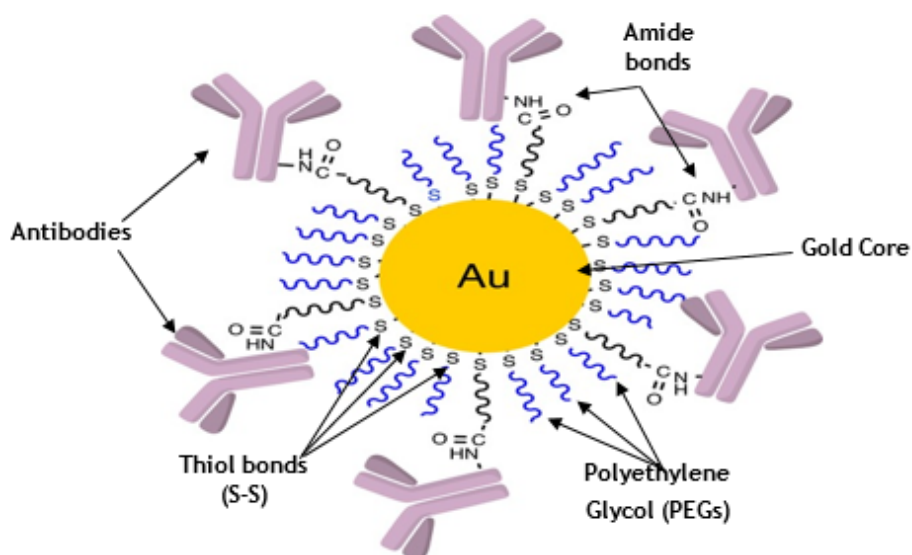


Figure 7: Figure shows the EGFR antibodies bound to gold core using polyethylene glycol (PEG) as a bifunctional linker.

1.4.3 Internalisation

Normally, nanoparticles are internalised by the cells via three main pathways: fluid-phase endocytosis, phagocytosis and receptor-mediated endocytosis (RME) (Yang *et al.*, 2005). RME is further divided into clathrin-, caveolin and raft-dependent endocytosis. Whereas clathrin- and caveolin proteins induce the invagination of the plasma membrane, raft is a specialised lipid molecule on the plasma membrane, and together with clathrin and caveolin mediates internalisation of the molecule. Endocytosis includes engulfing the GNPs via invagination of the plasma membrane forming a vesicle harbouring GNPs in the cytosol known as ‘endosomes’ which later fuses with ‘lysosomes’ to form ‘secondary lysosomes’ (Figure 8) (Dykman and Khlebtsov, 2014). Also, *in vitro*, tumour cells have been demonstrated to take up more GNPs than normal cells (Kodiha *et al.*, 2015). However, this varies from cell line to cell line e.g. hepatocellular carcinoma (HepG2) and cervix carcinoma cells (HeLa) have different rates of uptake of GNPs (Tkachenko *et al.*, 2004). Such difference of GNPs uptake by two different cell lines can be compensated by exploiting tumour-specific markers present in various cancer-types to increase specificity towards a different types of cancers (Kodiha *et al.*, 2015).

Moreover, in a size-dependent internalisation study, transferrin-coated 50nm GNPs were internalised by the mammalian cells at significantly higher rates than any other GNPs between 10nm – 100nm. This was explained by a process known as ‘wrapping-effect’ whereby the plasma membrane of the cell encloses the GNPs (Chithrani, Ghazani and Chan, 2006). The ‘wrapping-effect’ is dominated by two factors; 1) free energy released by ligand-receptor interaction and 2) receptor diffusion kinetics at the wrapping sites. According to the study conducted by (Gao, Shi and Freund, 2005), GNPs ranging between 27nm - 30nm has the best potential in internalisation by the cells.

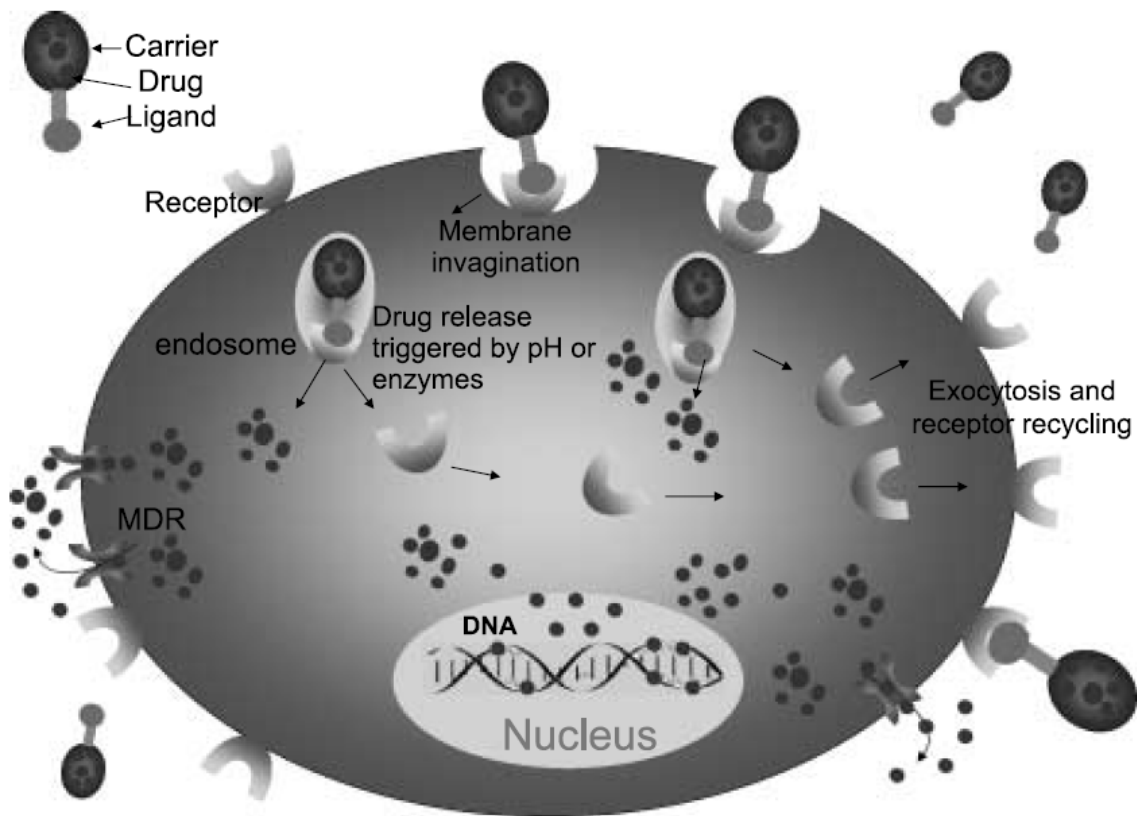


Figure 8: GNPs internalisation via the RME pathway. Tumour specific-ligand binds to target moiety and leads to the formation of vesicles/endosomes which harbour the GNPs-drug complex. Acidic environment, along with other enzymes in the endosome denatures the bond between the drug and GNPs releasing the drug in the cell's cytoplasm (Cho *et al.*, 2008).

1.4.4 Toxicity

It is vital to consider the inherent toxicity of GNPs due to its size, shape and ability to interact with surrounding tissue. Also, due to increasing usage of GNPs as contrast agents, therapeutic tool, imaging etc, it has become imperative to investigate its toxicological effects in the body (Trickler, Lantz et al. 2011). Most studies have described GNPs as non-toxic or less toxic since gold is an inert element (Goodman, McCusker et al. 2004). However, there is no conclusive evident that GNPs exert toxicity in the cells since there is not one standard method with which to measure its toxicity (Alkilany and Murphy, 2010). Most common methods that are employed to study toxicity relies upon proliferation and survival of the cells incubated with GNPs. For e.g., lactose dehydrogenase (LDH) colorimetric assay measures the

release of lactase in the media; MTT colorimetric assay measures the activity of mitochondria. Although these colorimetric assays detect plausible cell death directly by reduced cell proliferation and survival, these might not be a standard approach since GNPs absorb light in the visible spectrum which can underestimate the results (AshaRani *et al.*, 2009).

There has been size-dependent cytotoxicity observed for GNPs on neuronal differentiation, synapse formation and functional plasticity of neurons (Senut, Zhang *et al.* 2016). In another study, it was shown that 1.4nm GNPs were more toxic compared to other sizes when taken up by HeLa, L929, J774A1 and SK-Mel-28 cell lines. On the contrary, 15nm GNPs did not show any toxicity even at 60-fold higher concentration in the same cell lines (Pan *et al.*, 2007). Furthermore, bulk gold is chemically inert and, as such, non-toxic but the attached ligands to GNPs could infer unwanted toxicity (Hornos Carneiro, Barbosa 2016). For e.g. CTAB is used to give GNP a rod-like shape and, as a result, are bound onto the surface of GNPs conferring a positive charge. This GNP bound surfactant (CTAB) alone is toxic in sub-micromolar dose and, thus, it can be easily mistaken that the toxicity is due to the GNP (Alkilany, Murphy 2010). Furthermore, conflicting results could also arise from different parameters considered during experiments such as toxicity assays, cell lines used for assays, exposure of nanoparticles to cells and physicochemical properties of the nanoparticles. For e.g., citrate-capped 13 nm GNPs were non-toxic to human liver carcinoma cell lines but found toxic to human carcinoma lung cells (Goodman, McCusker *et al.* 2004).

Furthermore, GNPs have been found to increase endothelial paracellular permeability *in vitro* and elevate blood brain barrier permeability *in vivo* (Li *et al.*, 2015) and (Gromnicova *et al.*, 2013). To this course, Naz *et al.*, 2016 carried out the investigation of pharmacokinetics, distribution and urinary excretion of three different sized GNPs – 2nm, 5nm and 10nm in mice. It was found that no mortality or changes in behaviour, hair colour, weight and food intake was affected for the 2 nm GNPs. Additionally, there was no evidence produced for haematocrit,

serum biochemistry and tissue histology making GNPs non-toxic. On the contrary, mostly all GNPs was excreted through urine (Naz *et al.*, 2016). Thus, GNPs are non-toxic, and toxicity depends on ligands conjugated onto the GNPs and its size. At last, due to different parameters used to define the toxicity, one cannot be certain that *in vitro* toxicity is solely attributed to one single factor and, therefore, more thorough investigation is warranted.

1.5 GNPs and Cancer

Cancer therapy using GNPs can be executed in several ways. GNPs can be laden with specific drugs that selectively target cancer cells. Mainly, the drug is limited due to dose-limiting cytotoxicity effect, non-specific interaction, inability to target non-proliferative stem cells and low water solubility and biodistribution and using nanoparticles these inefficiencies can be circumvented (Bartos *et al.*, 2016). There has been increasing research to improve the drug pharmacokinetics resulting in reduction of the side effects and reaching for high-dose drug delivery. An example for GNPs usage in such a way is the loading of anti-EGFR cetuximab (C225) onto 5nm GNPs as a targeting agent and gemcitabine as a therapeutic payload in pancreatic cancer (Patra, Bhattacharya *et al.* 2010). Pancreatic cancer cells have also been shown to have 60% increase in expression of EGFR. As a result, GNPs carrying anti-cancer drug targeting EGFR in pancreatic cells have demonstrated reduced proliferation *in vitro* pancreatic cancer cells and *in vivo* orthotopic models (Patra, Bhattacharya *et al.* 2008). GNPs related cancer therapy has less cytotoxic effect on the normal tissue surrounding than using chemotherapeutic drugs alone. Hence, GNP is increasingly being used as a therapeutic approach in active targeting in cancer. However, to successfully implement these therapeutic effects, GNPs are required to reach a certain threshold within the cells efficiently (Alivisatos, 2004; Giljohann and Mirkin, 2009). In this work, to achieve the desired concentration of GNPs inside the cells, two receptors are selected to target simultaneously on CRC for its efficient internalisation: 1) Folate receptors and 2) Tyro3 receptors.

1.5.1 Folate receptors

Due to the drawback underpinning the usage of chemotherapy and radiotherapy, novel treatments are envisaged that make use of receptors that are upregulated in cancer. Folate receptors (FR) are such receptors that are overexpressed in various malignancies such as breast, colon, ovaries, endometrium, kidneys, brain and myeloid cells (Sega and Low, 2008). Normally, folate receptors are required to transport folic acid inside the cells where it is used for synthesis of amino acids as well as purines and thymidine (essential DNA components) (Massaro and Rogers, 2002; Antony, 1996). Folate is transported via FR that is anchored to the plasma membrane via a special class of proteins called glycosylphosphatidylinositol (GPI) proteins. Therefore, these combined structure of folate receptors and GPI proteins are also known as GPI-anchored membranous receptors (Wibowo *et al.*, 2013). FR- α and FR- β belongs to GPI-anchored family of receptors (Shen *et al.*, 1994; Wibowo *et al.*, 2013). On the other hand, FR- γ is a secreted receptor and is harboured in low concentration in the blood whilst FR- δ is only expressed on the surface of ovary and T-cells (Shen *et al.*, 2017).

Out of all the four FR isoforms, FR- α are expressed throughout the body but at a low level in normal tissues. However, FR- α are upregulated in various malignancies including CRC. Therefore, FR- α is chosen for targeting over other FR (Elnakat and Ratnam, 2004). Hence, for the purpose of showing the structure, FR- α is chosen. FR- α are synthesised with C-terminal peptide sequence that specifies GPI-anchoring site (Figure 10). These FR- α is then linked to a GPI-anchor attached to the plasma membrane by transamidase enzyme (Figure 9) (Sabharanjak and Mayor, 2004). FR- α itself has a globular structure, consisting of 4 long α -helices (α_1 , α_2 , α_3 , α_6), 2 short α -helices (α_4 , α_5), 4 short β -strands (β_1 – β_4) and many loop regions. Furthermore, this secondary protein structure is then transformed into tertiary structure via 8 disulphide bonds between 16 conserved cysteine residues (Figure 10) (Chen *et al.*, 2013).

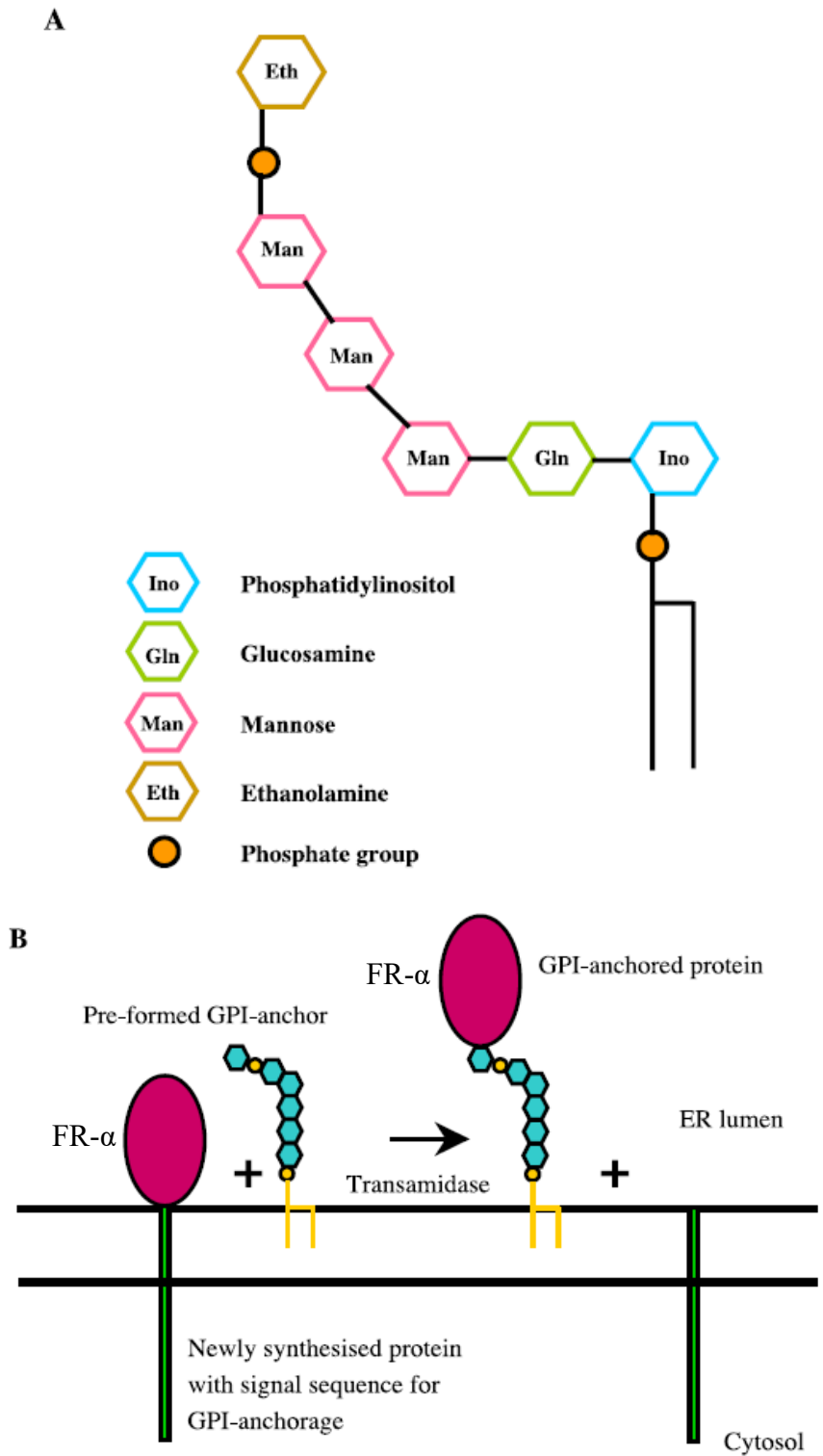


Figure 9: A) Structure of GPI proteins forming an anchor B) Enzymatic reaction linking FR- α to GPI-anchor via C-terminal signal peptide sequence in FR- α to ethanolamine on GPI-anchor protein. Adapted from (Sabharanjak and Mayor, 2004).

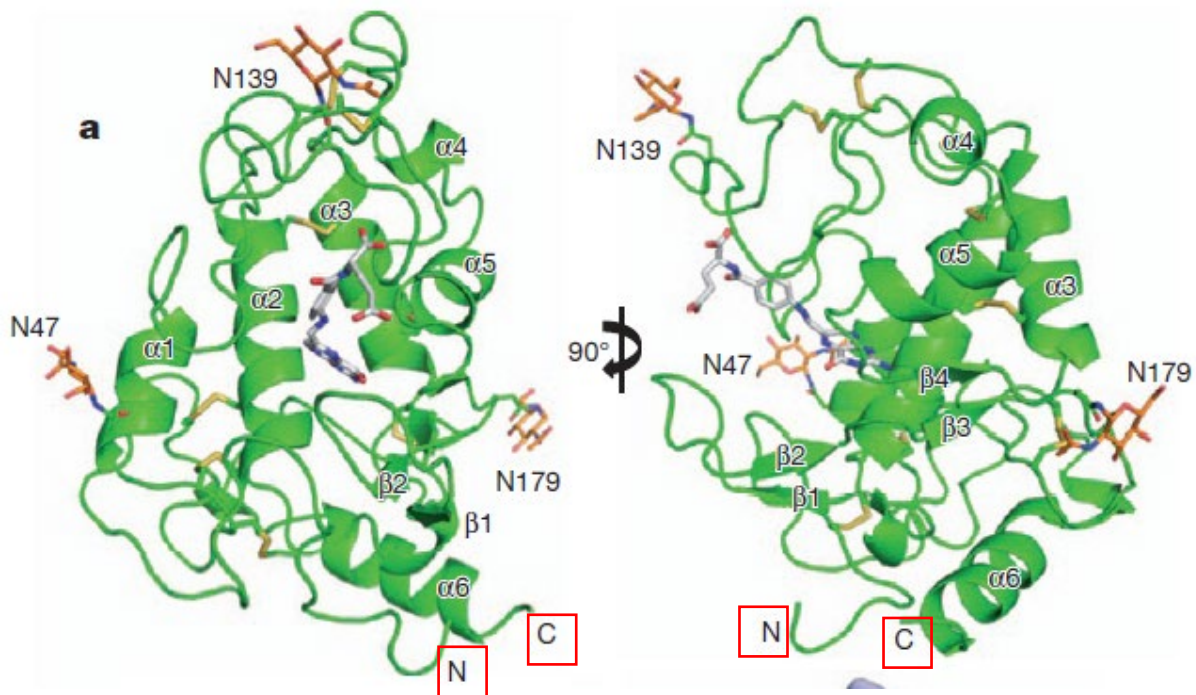


Figure 10: Figure shows two views of FR- α . FR- α has an overall globular structure. N and C termini are labelled (red boxes). Adapted from (Chen *et al.*, 2013).

These folate receptors are limited or absent in non-proliferating normal cells which help to distinguish tumour cells from normal healthy cells (Sega and Low, 2008). With regards to their location, FR- α is primarily found on apical surfaces such as kidney, lungs and mammary ducts whereas FR- β is found predominantly on activated myeloid cells. In cancer, FR- α is overexpressed in colon, ovary, breast and head and neck cancers constituting up to 40% in human cancers (Shen *et al.*, 2015). FR- β is upregulated in brain, liver, thyroid, uterus, stomach, prostate, testis and colon (Shen *et al.*, 2015). Therefore, due to its overexpression in different cancers, GNPs can be delivered using FR- α as a targeting moiety (Bhattacharya *et al.*, 2007).

1.5.2 Tyro3 receptors

Tyro3, together with Axl and Mer, constitutes the TAM receptor family and is a subfamily receptor tyrosine kinase. TAM receptors were discovered in 1991 and considered to be orphan receptors at the time (Schmidt *et al.*, 2012). Later, in 1995, Gas6/protein S (Pros1) were identified as ligands for TAM receptors (Stitt *et al.*, 1995). TAM mediates signal transduction through the binding of Gas6/Protein S followed by homodimerisation or

heterodimerisation of its receptors and autophosphorylation of the tyrosine residue in the kinase domain. Tyro3 can also be activated in ligand-independent activation when expressed in high numbers (Figure 11) (Taylor, Roy and Varmus, 1995). Tyro3, Axl and Mer, like all other tyrosine kinase receptors, has three domains; an extracellular, a transmembrane and an intracellular kinase domain. However, the key difference between TAM receptors from all other tyrosine kinase family of receptors is highly conserved motifs consisting of KW(I/L)A(I/L)ES sequence within its kinase domain (Figure 11) (Linger *et al.*, 2008). The two immunoglobulin-like domain (Ig) and two fibronectin type III (FNIII) constitutes the entire extracellular domain. Ig and FNIII are thought to be vital in cell-cell contact and closely mimic the structure of neural cell adhesion molecule (Yamagata, Sanes and Weiner, 2003).

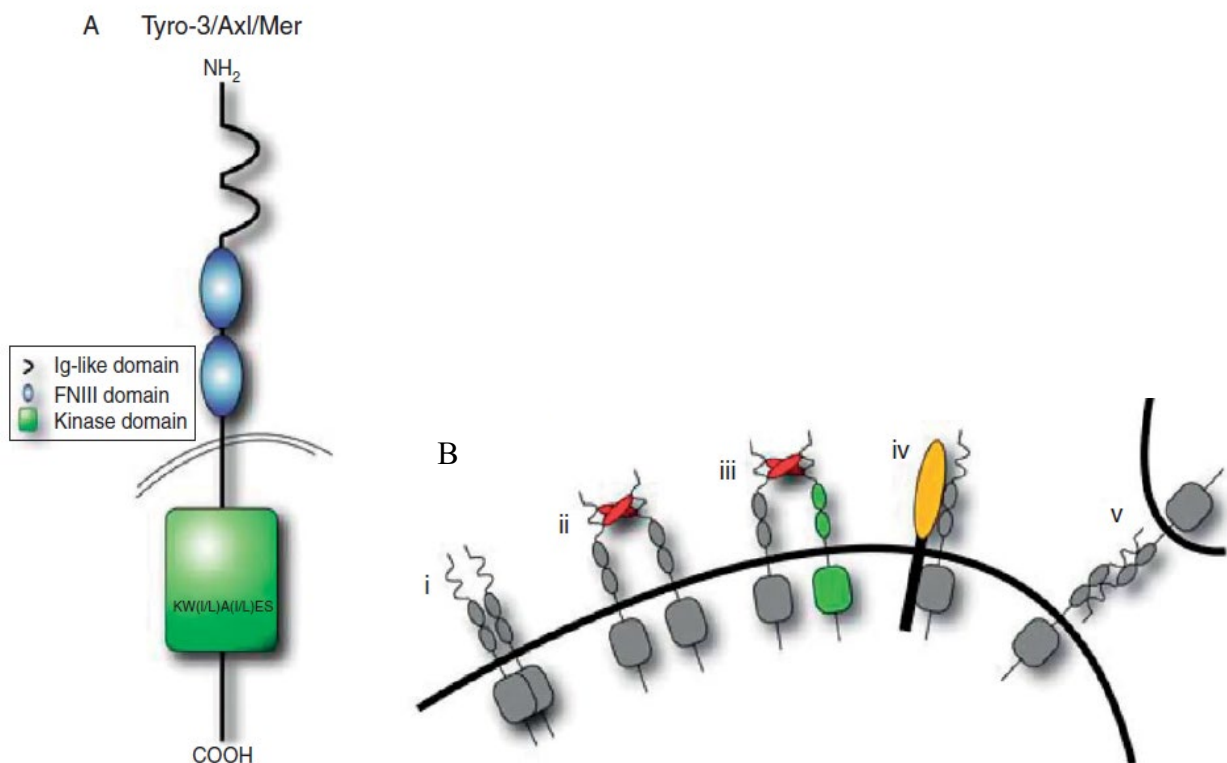


Figure 11: Structure and activation of TAM receptors. A) Shows the organisation of all the three domains; intracellular, transmembrane and extracellular. The conserved sequence is also highlighted in the kinase domain. B) All TAM receptor activation mechanisms i) ligand-independent dimerisation ii) ligand-dependent dimerisation iii) heteromeric dimerisation of two different TAM receptors iv) heterotypic dimerisation of TAM and non-TAM receptors and v) trans-cellular binding of extracellular domains. Adapted from (Linger *et al.*, 2008).

Tyro3, discovered in 1993, also known as Tif, Sky, BYK and Dtk (Chien *et al.*, 2016), was initially found to control embryonic differentiation (Biesecker, Gottschalk and Emerson, 1993). Tyro3's oncogenic potential first emerged when murine models were shown to have mammary tumours due to the upregulation of TAM receptors (Taylor *et al.*, 1995). Like FR, Tyro3 receptors are also upregulated in various human cancers including CRC and especially in haematological tumours. Tyro3 overexpression is correlated with poor prognosis and advanced tumour stage (Graham *et al.*, 2014).

In a study conducted in CRC patients, it was found that Tyro3 was overexpressed in CRC tumour patients compared with healthy colon mucosa ($p < 0.0001$). It was also shown that overexpression of Tyro3 led to CRC and metastasis in liver making Tyro3 a potential target in CRC (Schmitz *et al.*, 2016). In another study, comparing 76 polyps and 265 pairs of normal and cancer samples, overexpression of Tyro3 greatly enhances cell motility, invasion, anchorage-independent growth and metastatic ability in CRC. In the same study, meta-analysis showed Tyro3 induces endothelial to mesenchymal transition (EMT) (Chien *et al.*, 2016). Moreover, no clinical trials so far have been shown to have targeted Tyro3 receptors, making Tyro3 a novel target in CRC (Hojjat-Farsangi, 2014; Schmitz *et al.*, 2016). Besides CRC, Tyro3 as a novel target is also implicated in Hepatocellular Carcinoma (HCC) (Duan *et al.*, 2016).

1.6 Gap in the literature

Chemotherapy and radiotherapy have not increased overall survival of CRC and due to CRC's asymptomatic nature, it remains elusive until it has reached Duke' C or Duke's D stage where the 5-year survival rate is <5%. As a result, nanotechnology is exploited as a novel mechanism to target CRC tumour cells. GNPs between 1nm – 100nm can help target cancer cells *in vitro* and *in vivo* to circumvent the problem. Due to its physicochemical and optoelectronic properties, GNPs is applied in biomedical applications for targeting different cancers (Davis, Chen and Shin, 2008). One of the distinguishing features of the GNPs is the delivery of drug targeted towards the tumour sites because of its unique properties as mentioned above (Wang, Langer and Farokhzad, 2012). Since GNPs are continually used in therapy, drug delivery and imaging, its efficiency of delivery and internalisation is key for its successful application in biomedicine (Patra *et al.*, 2008; Sperling *et al.*, 2008; Wang, Langer and Farokhzad, 2012). Therefore, there is a need to achieve a higher threshold of GNPs in the tumour cells (El-Sayed, Huang and El-Sayed, 2006).

Normally, GNPs used in cancer using only a single type of antibody or a peptide which is overexpressed in cancers. Moreover, efficient delivery of the threshold amount of GNPs in cancer cells is required for its success in imaging, diagnosis and therapy (Alivisatos, 2004; Giljohann and Mirkin, 2009). In order to increase the efficiency of gold nanoparticles, another alternative strategy is to target different moieties on the cancer cells simultaneously (Arvizo, Bhattacharya and Mukherjee, 2010). Therefore, by targeting two different receptors (FR- α and Tyro3) simultaneously may increase the efficiency, delivery and internalisation of GNPs.

1.7 Research aims and objectives

The main aim of this work is to increase the delivery and internalisation of GNPs by targeting two different receptors in CRC cells simultaneously to increase their internalisation or uptake efficiency. Further aim is to develop 3D cancer models *in vitro* to experience more *in vivo*-like cell arrangements and to test GNP's efficacy in targeting CRC using these models. Thus, the objectives are:

- 1) To develop the GNPs constructs with Folate receptor- α antibody.
- 2) To develop the GNPs construct with Tyro3 antibody.
- 3) To develop a GNPs construct with Folate receptor- α and Tyro3 antibody for simultaneous targeting.
- 4) To characterise the conjugation of antibodies to GNPs using various analytical tools.
- 5) To develop a 3D Normal Colon and Colorectal Cancer *in vitro* model to assess the delivery and internalisation efficacy of GNPs constructs.
- 6) To determine the difference in delivery internalisation in 2D vs 3D CRC models.

CHAPTER 2

Synthesis and characterisation of Gold nanoparticles

2.1 Aim

The aim of this chapter is to construct anti-FR- α bound GNPs (GNPs-PEG-FR- α), anti-Tyro3 bound GNPs (GNPs-PEG-Tyro3) and anti-FR- α and anti-Tyro3 bound GNPs (GNPs-PEG-(FR- α +Tyro3)). Chapter also explores to validate the expression levels of FR- α and Tyro3 in normal and CRC cells.

Chapter also uses analytical techniques to characterise the conjugation of all the GNPs as below.

- 1) Immunocytochemistry was used to study the expression levels of FR- α and Tyro3 in normal vs CRC cells.
- 2) UV-visible spectroscopy (UV-Vis) was utilised to study the SPR peak of individual GNPs. A stability assay was also used to determine the stability at various ionic concentrations.
- 3) Dynamic Light Scattering (DLS) was used to estimate the size of each GNPs construct as well as the conjugation with mAbs.
- 4) Matrix-Assisted Laser Desorption/Ionisation – Time-of-Flight (MALDI-TOF) mass spectrometry (MS) was used to qualitatively assess the conjugation of FR- α and Tyro3 antibodies to each types of GNPs.
- 5) Bradford assay was used to quantify the amount of antibodies conjugated to each type of GNPs.

2.2 Introduction

GNPs can be used in various biomedical applications including diagnosis, therapy and delivering cytotoxic drugs. Due to its SPR property, GNPs can be characterised more readily than other imaging and contrast agents (Hainfeld *et al.*, 2006). GNPs are also biocompatible to human cells and can be readily conjugated with vast arrays of proteins in facile bio-conjugation (Connor *et al.*, 2005). Moreover, GNP has a strong binding affinity towards antibodies and other proteins that have naturally occurring thiols (e.g. glutathione and cysteine), disulphides and primary amine functional groups (Lee *et al.*, 2008). Therefore, in this chapter, GNP's conjugation to FR- α and Tyro3 is described along with its characterisation. Furthermore, the chapter also investigates the upregulation of FR- α and Tyro3 receptors in three cell lines 1) Normal Human Colon Epithelium (CRL1790) 2) Duke's B colorectal carcinoma (CRL2159) and 3) Colorectal carcinoma (HCT116). It is imperative that proteins, peptides, monoclonal antibodies (mAbs) etc to be used in biomedicine, for diagnostic and therapeutic purposes, needs to be chosen and assessed carefully so that they target the correct moiety on the cell's plasma membrane to target cancer. Also, GNPs attachment to mAbs and proteins needs to be analysed so it may remain stable for *in vitro* or *in vivo* application (Cao-Milán and Liz-Marzán, 2014).

There are different physical and chemical interactions with which mAbs, peptides etc can be attached to GNPs. Proteins can be attached via two possible mechanisms; 1) Non-covalent conjugation and 2) Covalent conjugation (Table 5) (Jazayeri *et al.*, 2016). The non-covalent method is spontaneous adsorption of the proteins, antibodies etc on the GNP's surface via hydrophobic and ionic interactions (Figure 12) (Rayavarapu *et al.*, 2007). Hydrophobic interactions with mAbs can be mediated via interaction between hydrophobic parts of the antibody and metal surface of the GNPs constituting a non-covalent bond. On the other hand, ionic or electrostatic non-covalent conjugation occurs via positively charged antibodies and negatively charged GNPs surface (e.g. citrate-capped GNPs) (Ljungblad, 2009). Bonds formed in such a manner, however, are weak and fragile and can be displaced easily by another strong

molecule with higher affinity towards GNPs in solution (S Kumar, Aaron and Sokolov, 2008). Therefore, due to weak interactions, bonding and easy displacement, neither hydrophobic nor electrostatic bonding was applied whilst preparing mAbs conjugated GNPs in this project.

Table 5: Non-covalent and Covalent modes of attachment between antibodies and Gold Nanoparticles surface is shown in the table (Jazayeri *et al.*, 2016).

Non-Covalent modes	Covalent modes
<ul style="list-style-type: none"> Hydrophobic interactions Ionic interactions 	<ul style="list-style-type: none"> Forming covalent bond via –SH (thiol) group Via EDC-NHS carbodiimide chemistry to form –CONH (amide) bond Via Streptavidin and biotin linkage

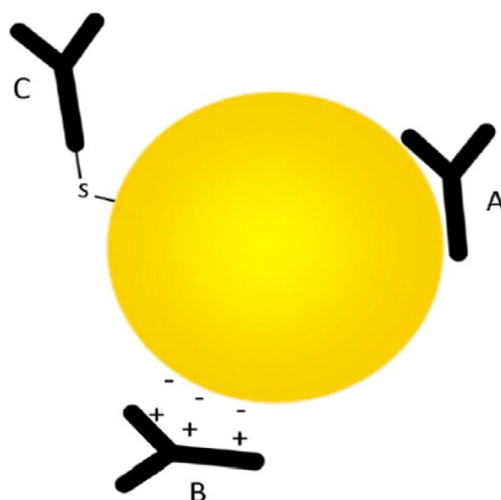


Figure 12: All three types of interaction between antibodies and Gold Nanoparticle's surface are shown in the figure. A) Hydrophobic bond B) Electrostatic or ionic bond and C) Covalent bond or dative binding (Jazayeri *et al.*, 2016).

Covalent conjugation attaches a protein via a functionalised group on GNPs surface. Compounds and antibodies can be attached using the innate thiol (-SH) group on the biomolecules (Figure 12) (Yu, Park and Jon, 2012). Covalent conjugation can also be mediated via reacting carboxylic (-COOH) group and amine (-NH₂) group between the two molecules. This involves by exploitation of water-soluble carbodiimide (EDC) and *N*-hydroxy-

succinimide (NHS) chemistry (Figure 13). First, $-\text{COOH}$ group is activated to form an intermediate compound O-Acylisourea; to which NHS is added forming another amine-reactive ester intermediate. After that, antibodies or proteins containing primary amine ($-\text{NH}_2$) group is mixed to the activated $-\text{COOH}$ complex forming an amide or peptide ($-\text{CONH}$) bond. Therefore, a strong and stable covalent bond is formed which cannot be easily displaced in high pH environment or ionic strength (Sperling and Parak, 2010).

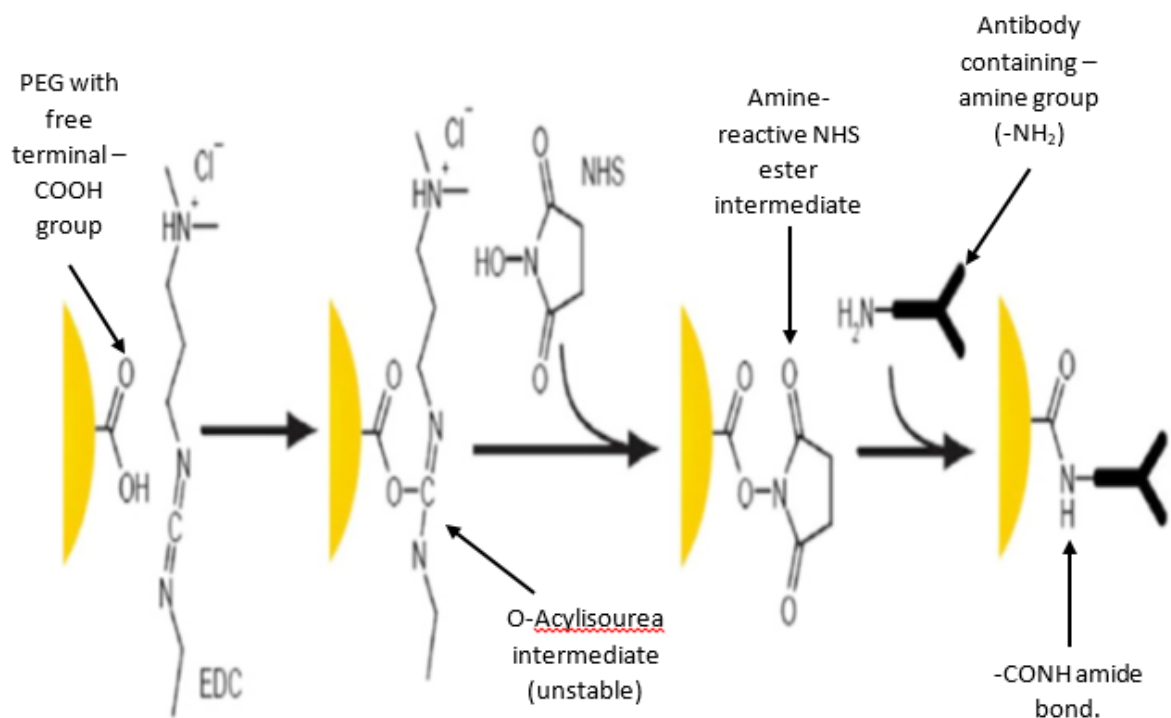


Figure 13: Gold Nanoparticles attached with antibodies using EDC and NHS chemistry is shown in the figure above. A bifunctional linker such as Polyethylene Glycol (PEG) is used which has a $-\text{SH}$ group on one end bound to the GNPs surface and a free $-\text{COOH}$ group to bind antibody. EDC is reacted with $-\text{COOH}$ group forming an O-Acylisourea intermediate. Secondly, NHS is reacted to form esters. Lastly, antibody or proteins containing amine group is added to form CONH (amide) covalent bond between antibody and GNPs (Jazayeri *et al.*, 2016).

2.3 Tyro3 and folate receptor- α mAbs conjugation to GNPs

Folate receptors (FR) are overexpressed in many cancers including CRC. On the contrary, these receptors are rarely present in non-proliferating normal cells and, thus, can be exploited to enhance the selective efficacy of GNPs in CRC. As such, folate receptor targeted

GNPs hold great promise in targeting various cancer (Samadian *et al.*, 2016). For enhancing efficiency of GNPs in CRC, FR- α was chosen as one of the receptors since they are specifically upregulated in CRC (Shia *et al.*, 2008) including ovarian, breast and head & neck cancer (Shen *et al.*, 2017). Moreover, FR- α specific mAbs (Farletuzumab) were also approved in clinical trials in ovarian cancer that exerted no toxicity (Ledermann, Canevari and Thigpen, 2015). Several FR targeted GNPs were also used against various cancers. For e.g., folate receptor targeted gold nanorods were internalised efficiently and selectively by KB cell lines (Huff *et al.*, 2007). Another study demonstrated the folate receptor-targeted GNPs in various ovarian cancer cell lines wherein GNPs were specifically internalised in the cancer cells (Bhattacharya *et al.*, 2007). In a yet another study to investigate internalisation in GNPs, folic acid conjugated GNPs were used against folate receptors. As a result, HeLa cells had specifically taken up FR targeted GNPs compared to normal A549 fibroblasts cell line that did not have folate receptors (Zhang *et al.*, 2010).

Another advantage of combining receptor FR- α with Tyro3 is its biological localisation. In normal condition, FR- α are expressed on the apical/luminal surface of the organs such as intestine, lung, retina, placenta and choroid plexus (Cheung *et al.*, 2016). However, due to its localisation it does not come into direct contact with the circulation and, hence, cannot be affected by circulating FR- α based targeting agents in the bloodstream such as GNPs (Elnakat and Ratnam, 2004). In the kidney, FR- α has a function to retrieve folate from the urine. However, in the study conducted by two independent groups to verify the uptake of FR- α based targeting agents in humans and rodents, respectively, observed no toxicity making FR- α good candidate for targeting. (Sega and Low, 2008; Low and Kularatne, 2009). Therefore, FA- α is conjugated to GNPs to enhance the efficacy and delivery of the GNPs. Similarly, Tyro3 is selectively upregulated in many malignancies including CRC (Hojjat-Farsangi, 2014). As such, it has shown a potential for targeting but, thus far has not been demonstrated in CRC (R. *et al.*,

2016). This project has shown and compared its efficiency for the first time in an effort to increase the internalisation efficiency of the GNPs by simultaneous targeting of FR- α and Tyro3 receptors. Furthermore, delivery of Tyro3 and FR- α mAbs conjugated GNPs is greatly enhanced by exploiting the EPR effect of the tumour as mentioned in chapter 1. Due to leaky vasculature of several hundred nanometres (100nm – 600nm) between the endothelial cells, GNPs <100nm will predominantly accumulate at the tumour site. At the same time, since normal vasculature has only few nanometres (5nm – 10nm) gap junctions, GNPs larger than 10nm would not leak out of the circulation and does not get deposited in the normal tissue. The EPR effect gives an upper hand in reducing any unwanted and non-specific GNPs interaction with normal tissue (Ali Mansoori, Brandenburg and Shakeri-Zadeh, 2010).

In order to attach FR- α and Tyro3 antibodies to GNPs, an intermediate heterobifunctional molecule/linker polyethylene glycol (PEG) ($M_w = 5000kDa$) was chosen that had an -SH group at one end and an -NHS reactive ester group at the other. The linker affords covalent conjugation of FR- α and Tyro3 mAbs to GNPs as mentioned above (Figure 13). The reason for choosing PEG as linker between GNPs and antibodies is multifactorial. PEG is biocompatible (Bhatia *et al.*, 2009) and allows easy covalent conjugation of FR- α and Tyro3 antibodies to GNPs (Seung *et al.*, 2005). It reduces non-specific interaction and, therefore, reduces unwanted protein adsorption and non-specific internalisation (Nativo, Prior and Brust, 2008). PEG also infers stability in a monodisperse GNPs suspension over a wide range of temperature, ionic strength and pH (Zhang *et al.*, 2007). Additionally, it prevents opsonin-binding and subsequent uptake by the reticuloendothelial system (RES) of the body (Dreaden *et al.*, 2009).

2.4 Methods and materials

2.4.1 Cell lines

The Human Colon Epithelium cell line (CRL1790), Human Duke's B Colorectal Carcinoma (CRL2159) and Colorectal Carcinoma (HCT116) were used to characterise overexpression of FR- α and Tyro3 in order to test the internalisation efficiency of GNPs against these receptors. CRL1790 (ATCC no. CCD841) a human colon epithelium cell line was used as a control between the passage 2 and 5. CRL2159 (ATCC no. LS411N) Duke's B stage human colorectal carcinoma cell line between the passage 2 and 5. HCT116 (ATCC no. CCL-247) human colorectal carcinoma cell line between the passage 2 and 6.

2.4.2 Culture media

CRL1790 was cultured using Sigma's Minimum Essential Medium (MEM) Eagle (product no. M4655) supplemented with 10% Fetal Bovine Serum (FBS) and 1% Penicillin/Streptomycin antibiotic solution. CRL2159 was cultured using Sigma's RPMI1640 (product no. R8758) supplemented with 10% FBS and 1% antibiotic solution. HCT116 was cultured using Gibco's Dulbecco's Modified Eagle Medium (DMEM) solution (product no. 61965-026) and supplemented with 10% FBS and 1% antibiotic solution. When cells are cultured for 3D culture, the antibiotic solution was replaced with an antifungal solution (Antibiotic and Antimycotic) (Gibco® 15240-062) to prevent any fungal growth on the skin and in the suspension (Chapter 4). The anti-fungal solution also has antibiotic properties to prevent any bacterial growth in the culture. Cells were grown in a humidified atmosphere in an incubator at 37°C and at 5% CO₂.

2.4.3 Cell passage

Cells were passaged upon reaching 80%-90% confluence, once or twice a week, depending upon the proliferation rate of the cells. Briefly, 2-3ml of trypsin was added after washing the flasks with 5ml of serum free media (without 10% FBS) and kept in the incubator for 2-3 minutes. 4-5ml of complete media with 10% FBS was then added to stop the action of the enzyme trypsin in the solution. The cells were then collected in a 10ml centrifuge tube and

centrifuged at 1500 RPM for 5 minutes. The supernatant was later removed, and fresh complete media was added and homogeneously mixed with the cell pellet followed by transference of the cells into a new flask.

2.4.4 Cell counting

A haemocytometer was used to count the cells to investigate the upregulation of FR- α and Tyro3 expression in all three cell lines. To count the cells, first, cells are collected in a 10ml centrifugal tube after trypsin digestion as before and centrifuged at 1500 RPM for 5 minutes. The supernatant was discarded. Then, 10ml of the complete medium, with 10% FBS and 1% pencillin/streptomycin solution, was added to the cell pellet and homogeneously mixed with the medium. Later, 20 μ l of the cell suspension was aliquoted in a haemocytometer to count the cells.

2.4.5 Fixation

All three cell lines CRL1790, CRL2159 and HCT116 were grown and cultured as described above using appropriate culture media. Later, 10,000 cells were aliquoted on a sterilised cover-slips in 6-well plates until they were 80%-90% confluent. For detecting differential levels of FR- α and Tyro3 receptors in normal vs. CRC cell lines, cells were washed 3 times with 1X PBS and fixed using 4% paraformaldehyde (PFA) for 30 minutes. After fixation, residual PFA was washed away by washing twice with 1X PBS after which all three cell lines were subjected to immunocytochemistry (ICC) experiments to visualise FR- α and Tyro3 receptor expression.

2.4.6 Immunocytochemistry

Fixed cells, after being washed 3 times with 1X PBS, were treated with citrate buffer at pH 6 for FR- α antigen retrieval for 10 minutes whereas it remained untreated for Tyro3 receptors. The citrate treated cells were washed thoroughly with 1X PBS. Subsequently, 50% horse serum in 1X PBS (1:1) was aliquoted to inhibit any unwanted signals and non-specific binding of primary antibodies to the antigen receptors. Thereafter, FR- α rabbit polyclonal

antibody (no. PA5-42004) at a concentration of 1:100 and Tyro3 mouse monoclonal antibody (no. MA5-11171) at a concentration of 1:50 were incubated with all three types of cell lines for 90 minutes followed by washing with 1X PBS. Next, using VECTASTAIN ABC kit (catalog no. AK-6100), a biotinylated-secondary antibody was incubated with the cells to facilitate binding with the primary antibodies for 30 minutes. Again, the residual unbound secondary antibody was washed away using 1X PBS. A tertiary peroxidase-labelled avidin was applied at room temperature for 20 min before developing with a tyramide signal amplification (TSA) fluorescein system (NEN Life Science Products, Boston, MA, USA) to enable the visualisation of the receptors. Excess FITC was washed away using 1X PBS, and the cover-slips were counter-stained using DAPI (4',6-diamidino-2-phenylindole) (product no. H-1200) based mounting media. Confocal microscopy was used for obtaining pictures of FR- α and Tyro3 expression.

2.4.7 Synthesis of Folate Receptor- α and Tyro3 conjugated Gold Nanoparticles

Lyophilised gold nanoparticles with PEG (5kDa) linker, NHS ester-activated kit were purchased from Cytodiagnostics (product no. CGN5K-5-2) and followed the protocol provided (Figure 14). The kit was used instead of conventional synthesis due to less time consumption, high reproducibility and faster and efficient covalent antibody conjugation with GNPs. Briefly, FR- α (catalogue no.- MA5-23917) (mouse monoclonal antibody) or Tyro3 (catalogue no.- ab235078) (rabbit monoclonal antibody) were suspended in the protein dilution buffer provided in the kit to a final concentration of 5mg/ml. Subsequently, 40 μ l (5mg/ml) FR- α or Tyro3 mAbs was mixed with 60 μ l reaction buffer, also provided in the kit, and mixed gently. Finally, the protein mix was reacted with NHS-activated GNPs-PEG for 2-3 hours to yield GNPs-PEG-FR- α and GNPs-PEG-Tyro3 conjugates. For GNPs-PEG-(FR- α +Tyro3), a 1:1 ratio of FR- α and Tyro3 mAbs were used with NHS-activated GNPs. The reaction was quenched using 10 μ l quencher provided. The solution was then centrifuged at 15,000g for 1 hour using 100kDa membrane filters (product no. VS0152) to remove any unbound antibodies

from all antibody-conjugated GNPs constructs. Later, the GNPs conjugates were re-suspended in deionised water. GNPs-PEG were synthesised by adding deionised water and activating the GNPs without any antibodies resulting into pegylated GNPs (GNPs-PEG). Synthesised conjugates were then stored at 4°C where it was stable for up to 3 months.

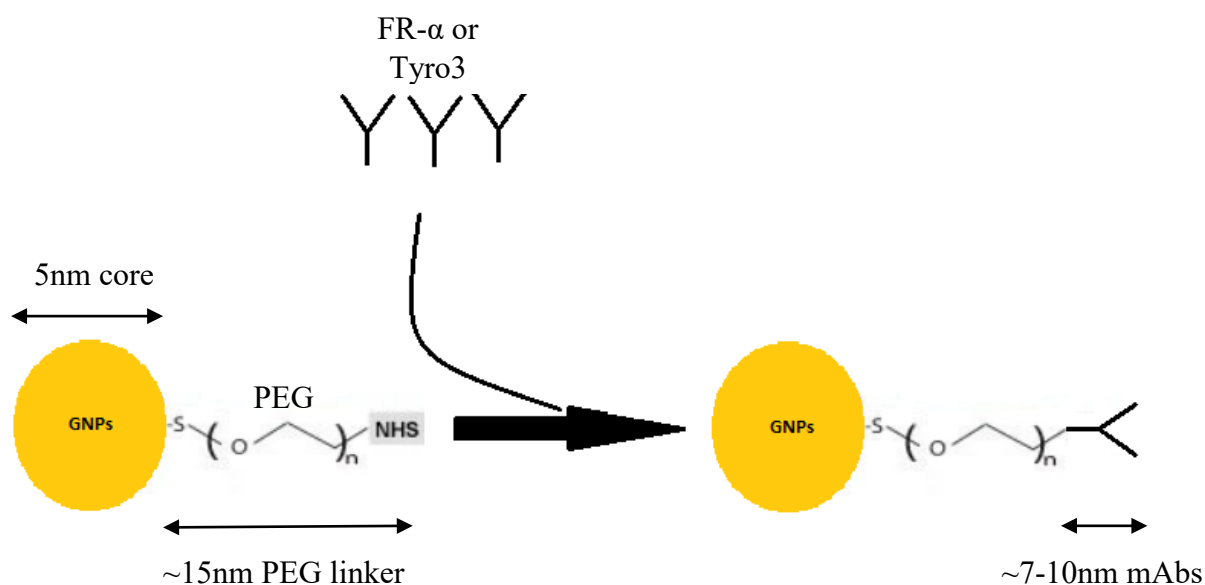


Figure 14: Schematic representation of the attachment of mAbs to GNPs is shown. GNP core is 5nm, PEG linker is ~15nm and mAbs ~7-10nm. Approximately 7 antibodies were attached per GNP after the conjugation step.

2.4.8 Ultraviolet visible (UV-Vis) spectroscopy

Ultraviolet Visible (UV-Vis) spectroscopy is a vital technique in determining GNPs size distribution, concentration and aggregation levels (Amendola and Meneghetti, 2009). This is the most common technique used in the analysis of gold nanoparticles, where the absorbance and scattering of GNPs in suspension are dominated by its SPR. GNP's SPR (λ_{max}) peak in the visible spectrum (400nm-800nm) is unique and reflective of its size distribution. For e.g., the wavelength of maximum extinction changes with nanoparticle size (Pal, Tak and Song, 2015). As such all GNPs conjugates were subjected to UV-Vis spectroscopy. Briefly, 300 μ L of each of the 4 GNPs samples were aliquoted into a 96-well plate (96 NUN) which was placed into a 96-well plate reader device. The BMG FLUstar Omega software was used to read the

absorbance at room temperature. Wavelength was set between 400-800nm. The reading took approximately 7 seconds.

2.4.9 Stability assay

GNPs to be used *in vitro* or *in vivo* need to be stable across a wide range of ionic strengths. Noble metallic nanoparticles such as GNPs strongly absorb the light that is highly associated with the physical properties of the nanoparticles (Raouf *et al.*, 2012). Thus, the UV-Vis peaks were used not only to determine the attachment but also for aggregation via broadening of the peak and spectral red-shifts (Ray *et al.*, 2015). Different analytes and chemicals can induce aggregation, disaggregation or change of the local refractive index resulting in a shifting of the SPR band accordingly (Fang *et al.*, 2009) and (Murphy *et al.*, 2008). Therefore, it is crucial to qualitatively measure GNPs aggregation in the solution that would provide a valuable assessment of colloidal stability of bio-nano interfaces after surface functionalization. To this end, a flocculation assay was conducted to study the aggregation caused by the introduction of different concentration of NaCl (0.001M – 1M). As such, 1ml of each antibodies coated GNPs construct were mixed with 100 μ l of different NaCl concentrations (0.001M, 0.05M, 0.1M and 1M) for 1 hour to check for the aggregation via a red-spectral shift in SPR peak using the UV-Vis spectrophotometer as above. Stability test was also carried out after storing the GNPs constructs at 4°C for 3 months and conducting DLS test. In that regards, no aggregation was observed and all the GNPs constructs were highly monodispersed.

2.4.10 Dynamic light Scattering (DLS)

The Dynamic light scattering (DLS) (Malvern Nano-ZS) device was used to find the distribution of the size of the nanoparticles in the suspension. DLS is popular in order to determine the hydrodynamic size of the GNPs in suspension, up to sub-nanometers. It exploits the feature of capturing the scattered light intensity produced when nanomaterials undergo 'Brownian motion' by illuminating it via a laser beam (Kaszuba *et al.*, 2008). Particle-size distribution plays a fundamental role in determining the properties of the nanomaterials. For

e.g., property of bulk gold is different from that of GNPs at nanometres scale (Jazayeri *et al.*, 2016). Size monitoring not only allows one to determine the attachment of proteins but also a quality control measure to determine aggregation. Therefore, to assess the quality, size characterisation is a vital step in GNPs application (Brar and Verma, 2011). Disposable cuvettes were used to determine the size of all 4 GNPs constructs. 1.5ml of all GNPs solutions were loaded into the DLS and measurements were taken. Readings were taken in the multiple of 3 for every GNPs solution.

2.4.11 Matrix Associated Laser Desorption/Ionisation – Time of flight (MALDI-TOF) Mass spectrometry (MS)

The analytical technique, mass spectroscopy, is based on measuring the chemicals through its mass-to-charge (m/z) ratio. Analysis of the sample via MALDI-TOF-MS is done by preparing and mixing a matrix with the samples. Some examples of the matrixes are α -Cyano-4-hydroxycinnamic acid (HCCA), 2, 5-Dihydroxybenzoic acid (DHB) and Sinapinic acid (SA). Upon crystallisation of the matrix, samples are also crystallised and dried trapping the sample within the matrix. When the laser beam is fired upon the matrix associated sample, it becomes ionised. Due to the ionisation and desorption, it produces single protonated ions from the analytes of the sample. The ionic charge of these particles travels through the length of the tube in relationship to mass-to-charge (m/z) ratio. These charged particles are then detected using a mass analyser such as Time-of-Flight (TOF) analyser (Singhal *et. al*, 2015) (Figure 15).

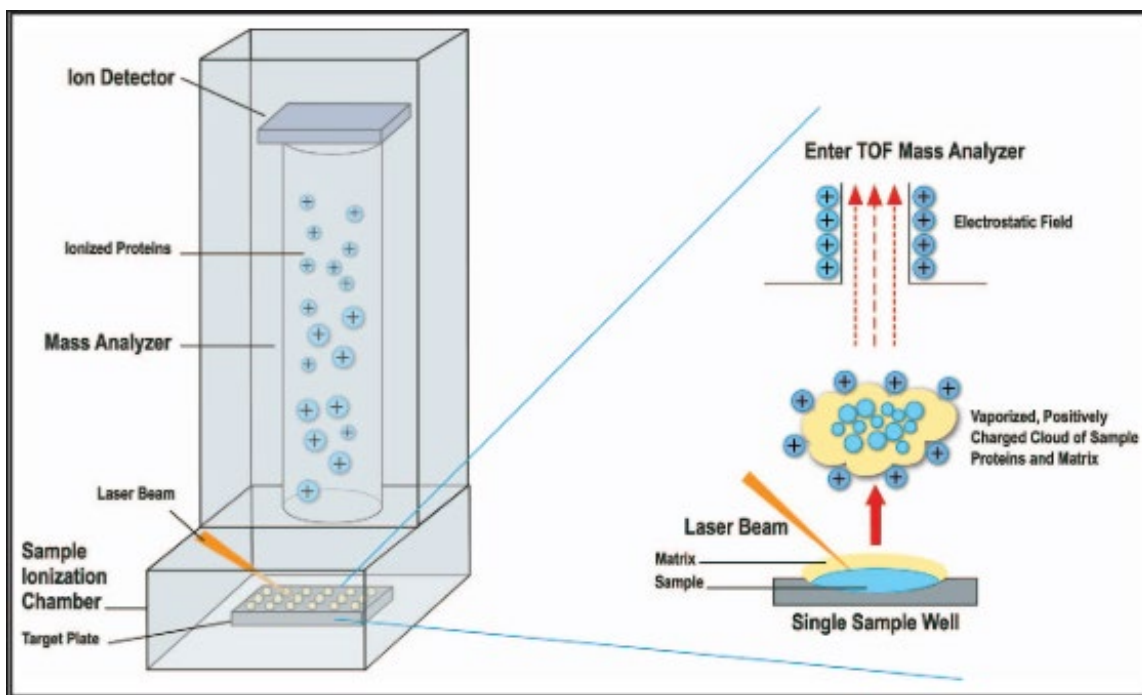


Figure 15: MALDI-TOF working principle is shown in the figure above. Samples are aliquoted on the allocated spaces on the target plate mixed with the matrix and allowed to dry. Laser beam is fired to create ionisation and desorption and to produce protonated ions. These ions then travels through the length of the tube and are detected via an ion detector (Patel, 2015).

The MALDI-TOF instrument (Bruker) was calibrated using an IgG mAbs as standard (product no. 56834-25MG). Thereafter, 1 μ l GNPs-PEG, GNPs-PEG-FR- α , GNPs-PEG-Tyro3 and GNPs-PEG-(FR- α +Tyro3) conjugates were deposited on the target plate to detect the presence of antibody attached. The samples were left to air-dry at room temperature and then 1 μ l of SA in acetonitrile and water (1:1) with 0.1% trifluoroacetate (TFA) (70:30 v/v) was pipetted onto the dried sample and left to form a thin layer over the sample at room temperature. The mass spectra were acquired in a positive linear mode with the laser beam at 60% intensity and 5000 shots on an average were fired upon the sample to generate protonated ions within the 20,000-200,000 m/z range. Spectra were reviewed in FlexAnalysis Software (Bruker) and visually inspected for the presence of monoclonal peaks.

2.4.12 Bradford assay

Bradford assay was used to quantify the FR- α and Tyro3 mAbs conjugation to GNPs. The Bradford assay involves the use of the dye Coomassie Brilliant Blue G-250 for quantification of proteins. The dye goes into ionic interaction by first donating its free proton

to the ionisable amino acids on the protein (arginine, histidine, phenylalanine, tryptophan and tyrosine) causing conformational changes that, consequently, exposes the protein's hydrophobic core. This interaction brings about stabilization of the blue form (the anionic form) of coomassie dye, subsequently shifting the absorption peak of the dye at 595 nm (Bradford, 1976). Concentrations were calculated from a standard IgG (product no. 56834-25MG) curve (0 $\mu\text{g/ml}$ to 50 $\mu\text{g/ml}$) (Figure 31) prepared in deionised water. Following the centrifugation of each type of GNPs construct approximately 100 μl of supernatant and each IgG concentration was aliquoted in each well of 96-well plate, followed by addition of 150 μl Bradford reagent. The mixture was gently pipetted up and down and allowed to react for 10 minutes in the dark before being subjected to absorbance reading at 595nm. The obtained absorbance reading measurement was converted into concentration from the IgG standard curve. Later, concentration of the supernatant was subtracted from the initial concentration of the mAbs used to determine the concentration of the mAbs attached to each GNPs construct. Moreover, concentration was then used further to estimate the number of antibodies attached to each GNPs using the method mentioned elsewhere (Tripathi and Driskell, 2018) and followed here.

2.5 Results

Expression of FR- α and Tyro3 in CRL1790, CRL2159 and HCT116 was determined for its feasibility in gold nanoparticles targeting. FR- α were overexpressed in CRC and absent or present in low numbers in normal colon epithelium (Figure 16). Moreover, the expression of Tyro3 was also obtained and a similar finding has been observed, in that Tyro3 receptors were overexpressed in CRC cell lines (CRL2159 and HCT116) compared to normal colon epithelium (CRL1790) (Figure 17).

2.5.1 FR- α expression in CRL1790, CRL2159 and HCT116 cell lines

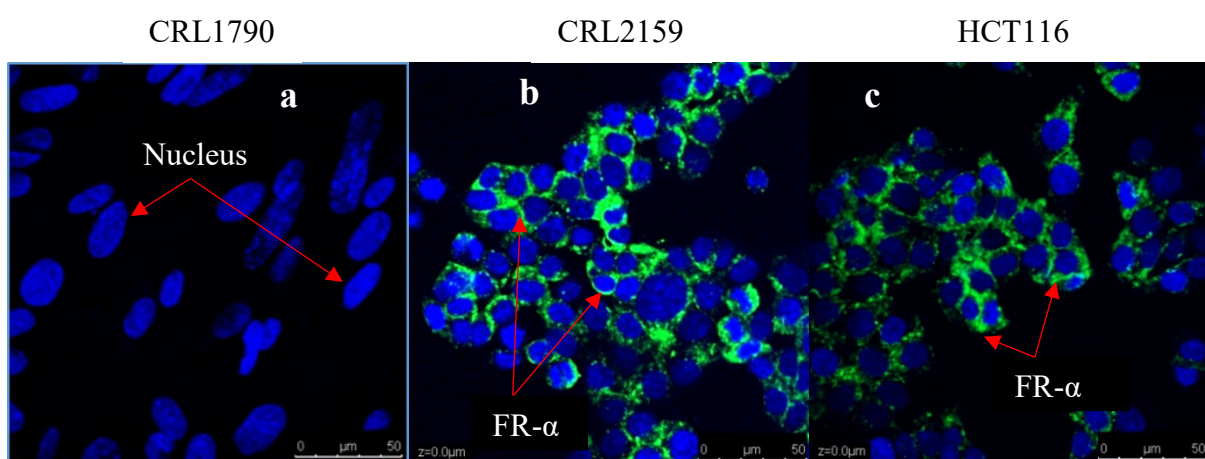


Figure 16:- Figure shows the relative expression of FR- α in all three cell lines. DAPI stains the nucleus blue while FITC stains the FR- α membranous receptors in green. a) Colon Epithelium (CRL1790), b) Duke' B colorectal carcinoma (CRL2159) and c) Colorectal carcinoma (HCT116). Clear expression patterns can be seen of FR- α receptors being upregulated in CRL2159 and HCT116 compared to CRL1790. Scale bar = 50 μm . Magnification 40X.

2.5.2 Tyro3 expression in CRL1790, CRL2159 and HCT116 cell lines

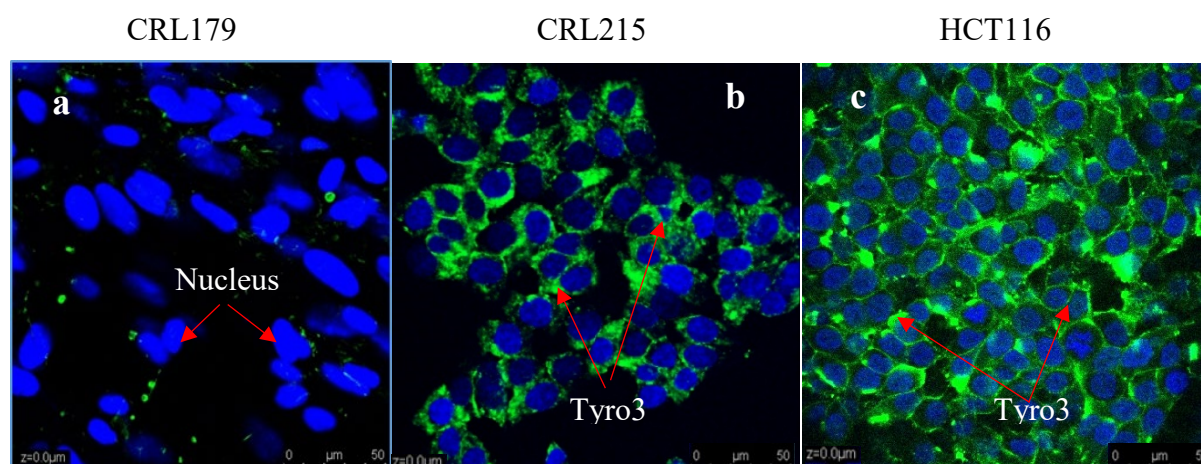


Figure 17:- Figure shows the relative expression of Tyro3 receptors in three types of cell lines. DAPI stains the nucleus blue while FITC stains the Tyro3 membranous receptors in green. a) Colon Epithelium (CRL1790), b) Duke' B colorectal carcinoma (CRL2159) and c) Colorectal carcinoma (HCT116). Clear expression patterns can be seen of Tyro3 receptors being upregulated in CRL2159 and HCT116 compared to CRL1790. Scale bar = 50 μ m. Magnification 40X.

2.5.3 UV-Vis spectroscopy

UV-Vis spectroscopy exploits the SPR feature to determine the size and synthesis of GNPs. The SPR band characteristic of the gold nanoparticles lies in the visible region of the electromagnetic spectrum and any alterations to the surroundings of these particles, such as surface modification and aggregation, leads to a colorimetric alteration of the dispersion. This is due to the oscillation of the electrons in the visible spectrum at a specific wavelength of light (Martínez *et al.*, 2012). When the overall size of the GNP increases, the peak shifts towards the red region of the visible spectrum (Haiss *et al.*, 2007). Hence, UV-Vis spectra is used to determine the characteristics and attachment of the FR- α and Tyro3 mAbs to GNPs. All four GNPs 1) GNPs-PEG 2) GNPs-PEG-FR- α 3) GNPs-PEG-Tyro3 and 4) GNPs-PEG-(FR- α +Tyro3) constructs were analysed for their respective SPR (λ_{\max}) peaks.

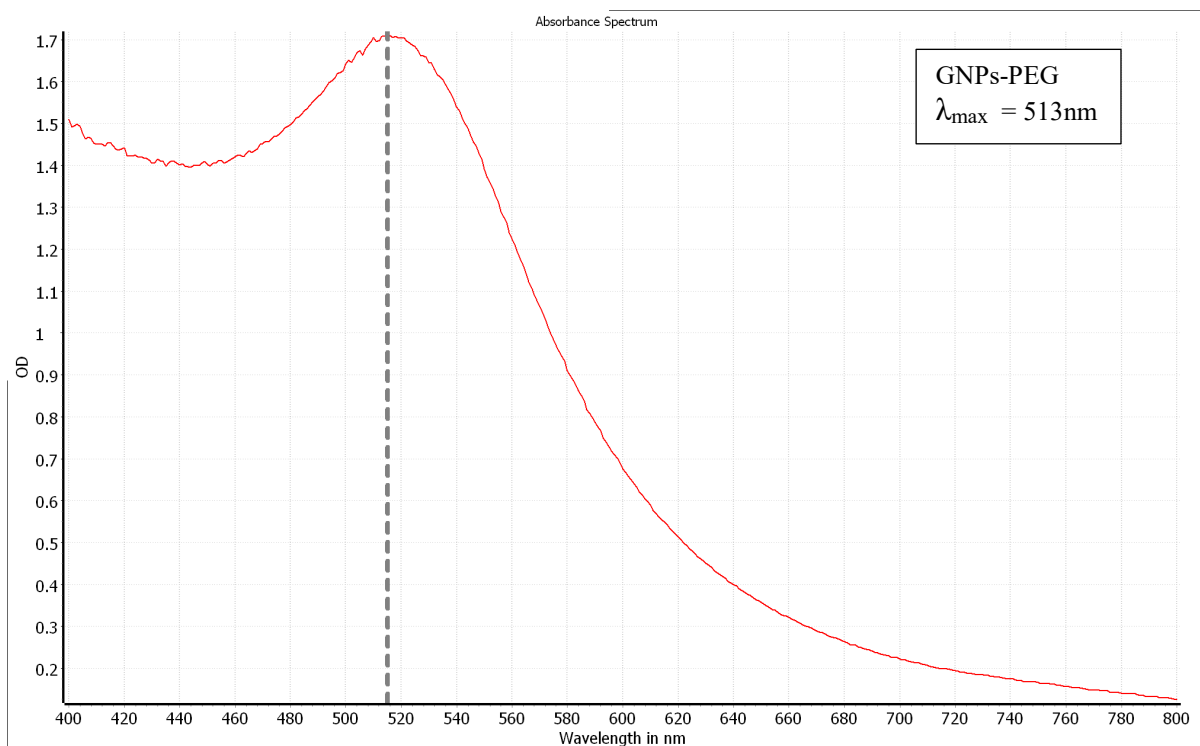


Figure 18:- The UV-Vis (λ_{\max}) peak of GNPs-PEG was at 513nm.

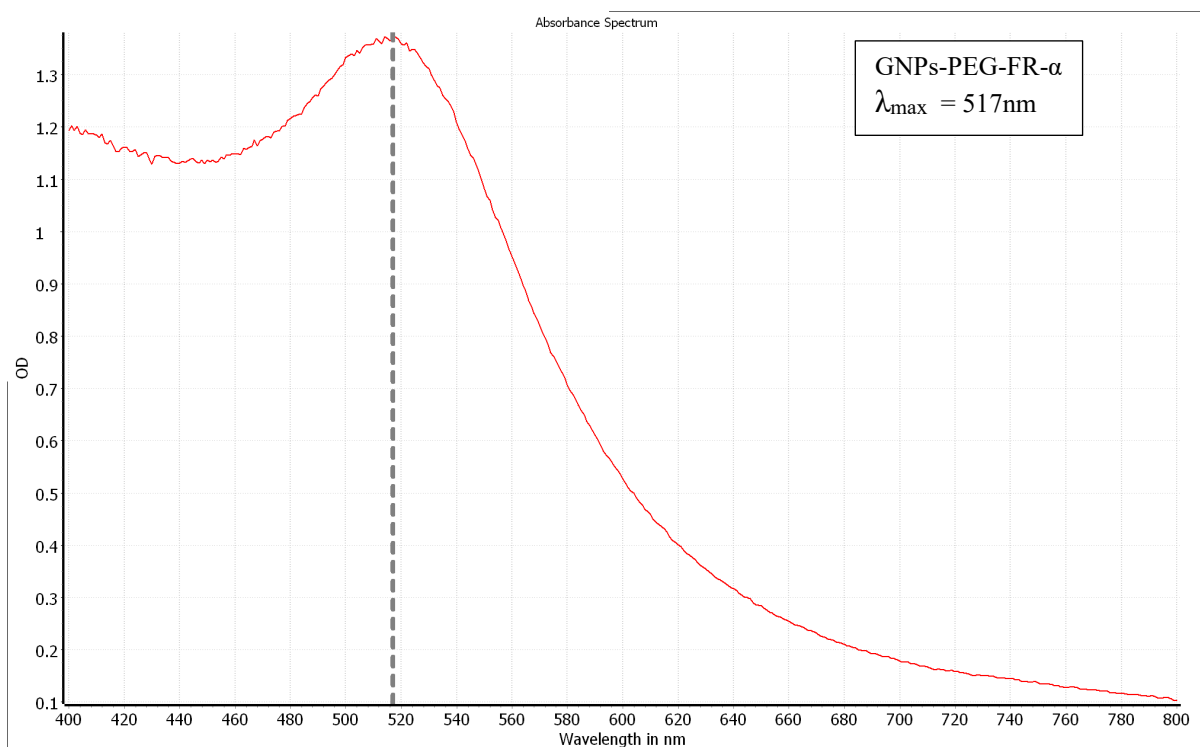


Figure 19:- The UV-Vis (λ_{\max}) peak of GNPs-PEG-FR- α was at 517nm.

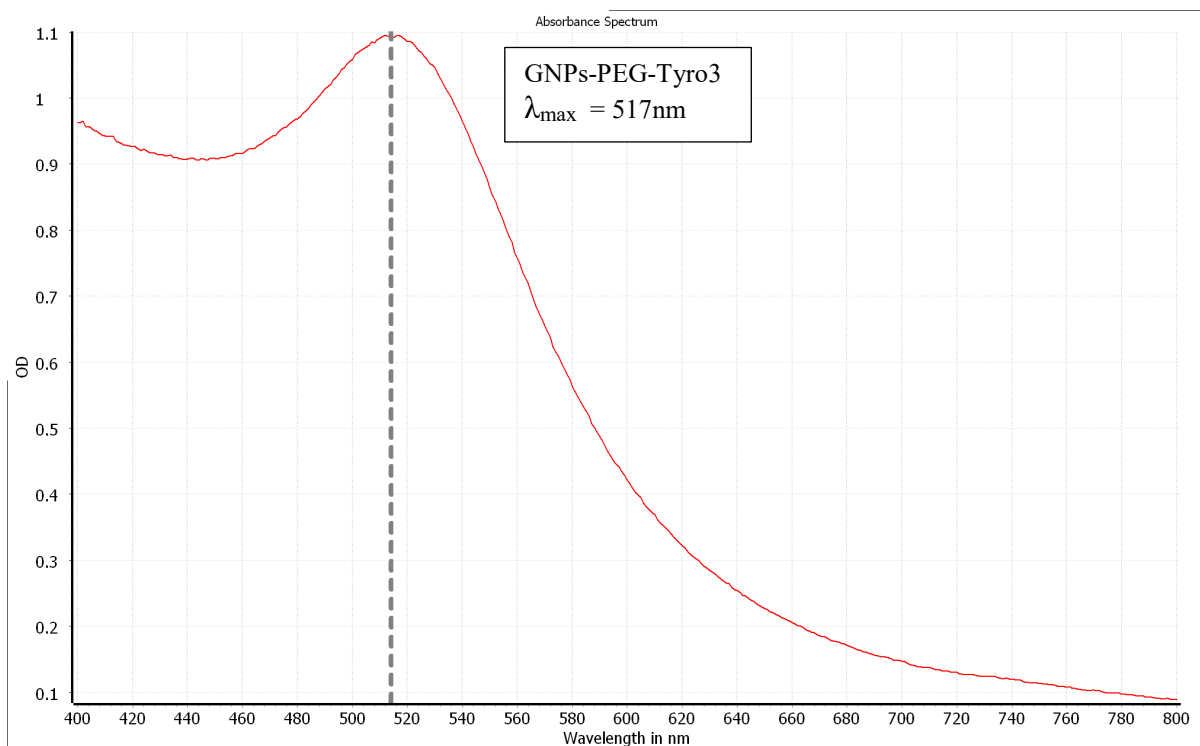


Figure 20:- The UV-Vis (λ_{\max}) peak of GNPs-PEG-Tyro3 was at 517nm.

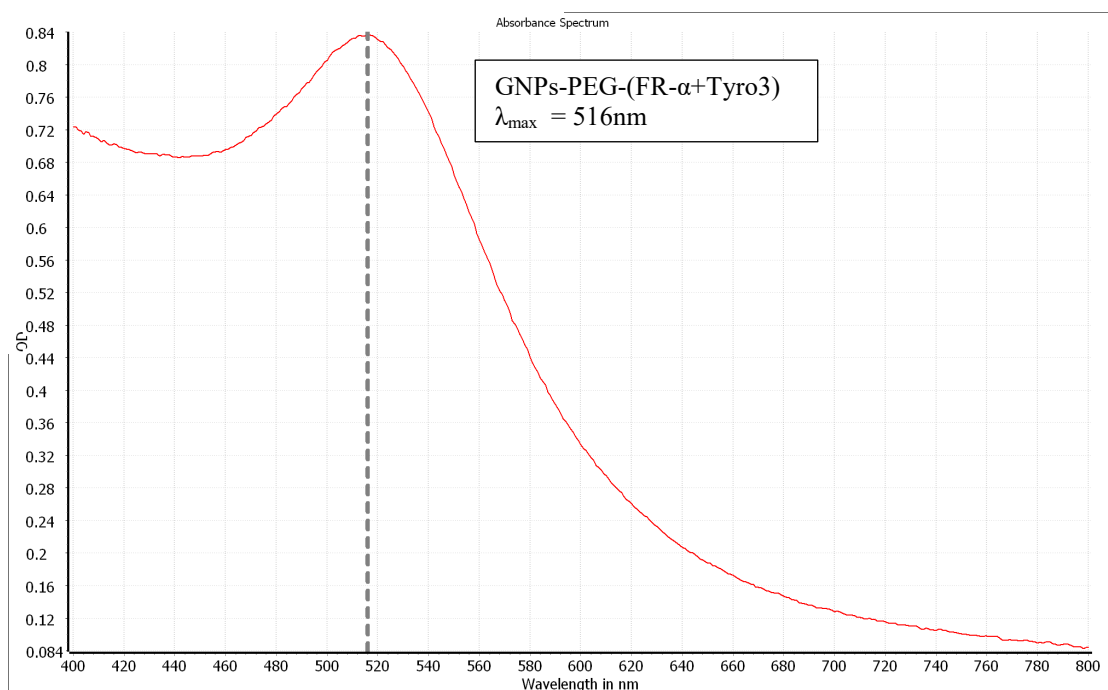


Figure 21: The UV-Vis (λ_{\max}) peak of GNPs-PEG-(FR- α +Tyro3) was at 516nm.

2.5.4 Stability assay

GNPs to be used *in vitro* or *in vivo* needs to be stable across a wide range of ionic strengths. To prove all antibody-coated GNPs were stable after the FR- α and Tyro3 attachment, different concentration of NaCl (0.001M – 1M) were added to the mixture and UV-Vis reading were taken for the presence of the SPR peak. No stability test for GNPs-PEG was done since antibody was not conjugated to this sample. Therefore, only GNPs attached with FR- α and Tyro3 mAbs were tested to assess the stability of the covalent bonds (Figure 22), (Figure 23) and (Figure 24).

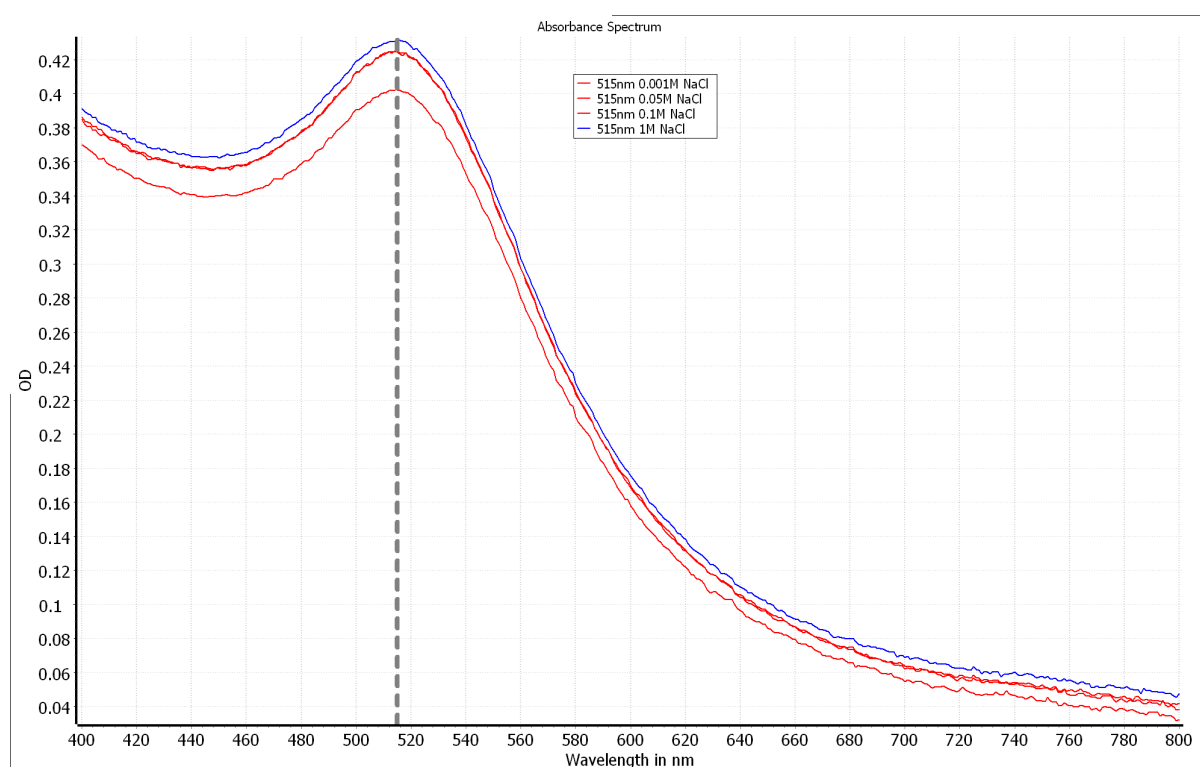


Figure 22:- The stability of GNPs-PEG-FR- α in at different NaCl concentration solution (0.001M – 1M). No SPR red-shift observed.

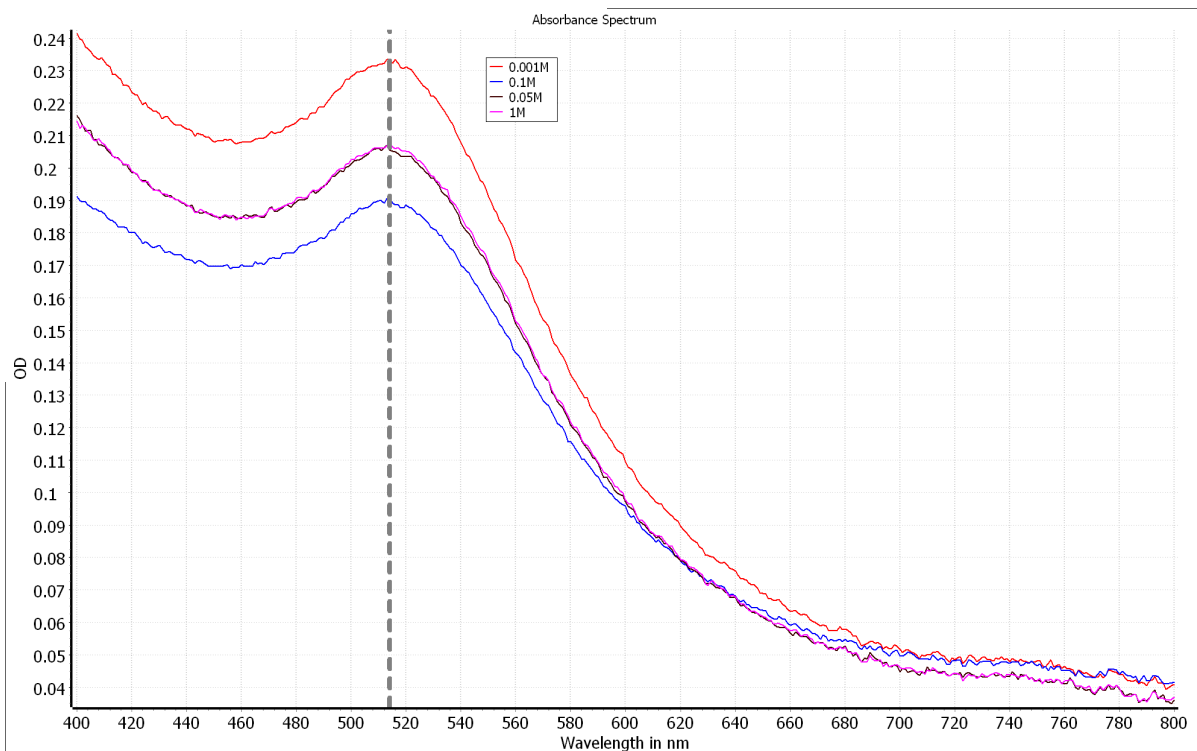


Figure 23:- The stability of GNPs-PEG-Tyro3 at different NaCl concentration solution (0.001M – 1M).

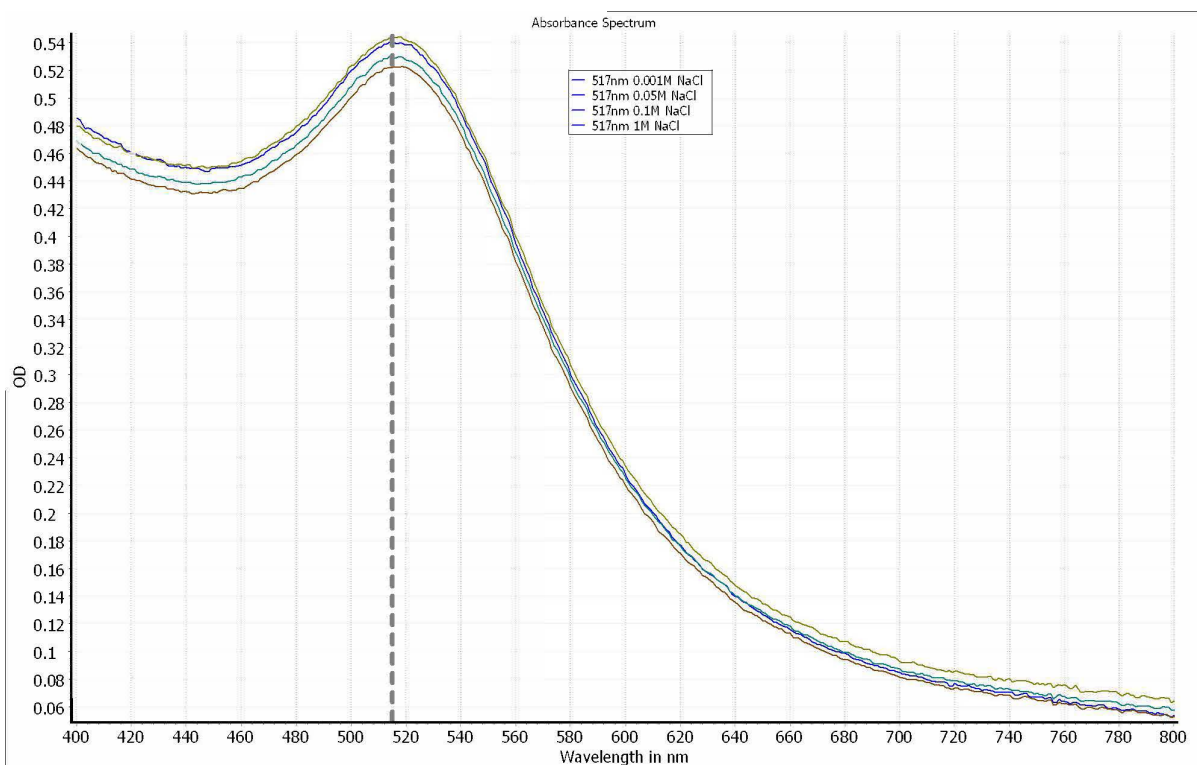


Figure 24:- The stability of GNPs-PEG-(FR- α +Tyro3) at different NaCl concentration solution (0.001M – 1M). No SPR red-shift observed.

2.5.5 DLS

DLS was used to measure the size of the GNPs attached to PEG and, in turn, with FR- α and Tyro3. DLS measures the hydrodynamic diameter of the molecules in the suspension. After the attachment of FR- α and Tyro3 mAbs to GNPs-PEG the overall size of the newly formed single- and double-antibody coated GNPs increases confirming the attachment with FR- α and Tyro3. TEM can also be used to study size distribution profile of GNPs (Murray, Kagan and Bawendi, 2000) . However, it has its own disadvantages. To begin with, GNPs requires to be studied robustly in real time for e.g. soon after the stability test is conducted as mentioned above to assess the level of aggregation. This cannot be done via TEM since tedious sample preparations is required before the samples are subjected to the microscopy. Additionally, concentration of the GNPs also cannot be ascertained using only TEM (Amendola and Meneghetti, 2009). Besides, TEM can modify morphology and size distribution of the GNPs (Gonzalez *et al.*, 2005) for e.g. when GNPs are involved in solid matrixes and reactive environments (Corbierre *et al.*, 2001). Nonetheless, TEM can prove as useful tool when used together with UV-vis and DLS since combined use of all three techniques can give conclusive results on GNPs size. TEM in this project was not utilised due to the lack of access to the technique and instead size determination of all GNPs constructs was done using UV-vis and DLS.

Table 6: Summary of UV (λ_{max}) SPR peak and DLS size measurement of all 4 types of GNPs.

Types of GNPs constructs	UV-Vis Spectrophotometry	DLS (nm)	PDI
GNPs-PEG	513nm	22.97nm \pm 2.1	0.204
GNPs-PEG- FR- α	517nm	30.78nm \pm 1.8	0.231
GNPs-PEG-Tyro3	517nm	31.76nm \pm 2.9	0.225
GNPs-PEG-(FR- α +Tyro3)	516nm	31.64nm \pm 2.3	0.252

Results

	Size (d.nm):	% Volume:	St Dev (d.nm):
Z-Average (d.nm): 157.2	Peak 1: 22.97	99.9	5.773
Pdi: 0.204	Peak 2: 231.2	0.1	43.06
Intercept: 0.793	Peak 3: 0.000	0.0	0.000

Result quality : Refer to quality report

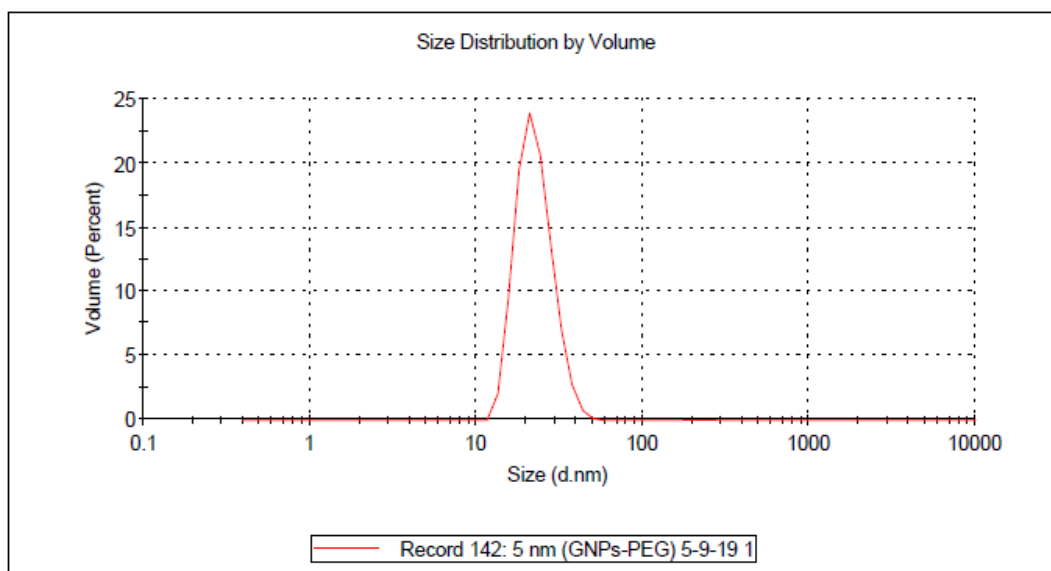


Figure 25: The size distribution profile of GNPs-PEG is shown. Most GNPs in this suspension are 22.97nm size (Polydispersity index (PDI) = 0.204).

Results

	Size (d.nm):	% Volume:	St Dev (d.nm):
Z-Average (d.nm): 43.77	Peak 1: 30.78	100.0	9.093
Pdi: 0.231	Peak 2: 0.000	0.0	0.000
Intercept: 0.882	Peak 3: 0.000	0.0	0.000

Result quality : Refer to quality report

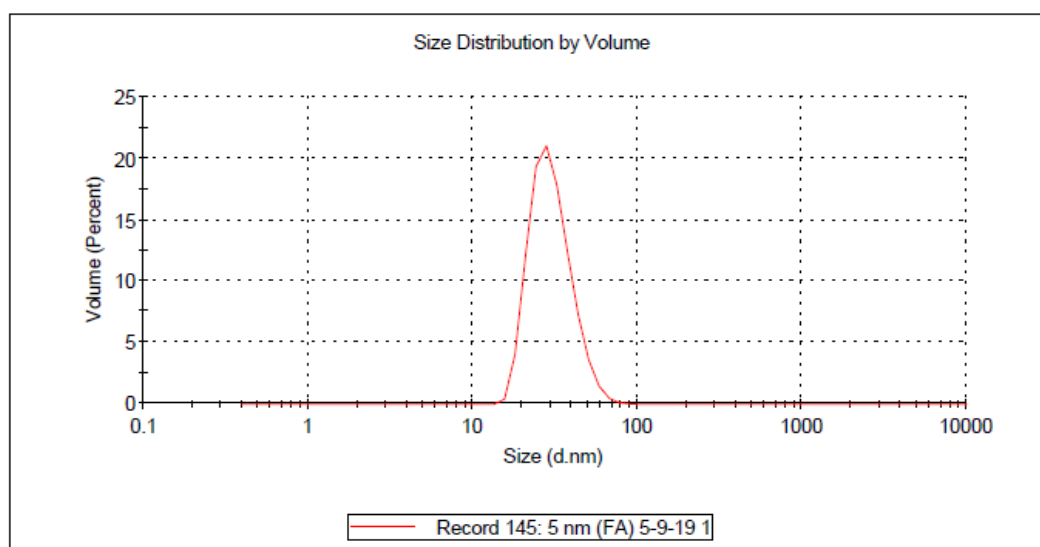


Figure 26:- The size distribution profile of GNPs-PEG-FR- α is shown. Most GNPs in this suspension are 30.78 nm size (Polydispersity index (PDI) = 0.231).

Results

	Size (d.nm):	% Volume:	St Dev (d.nm):
Z-Average (d.nm): 46.64	Peak 1: 31.76	89.5	12.06
Pdi: 0.225	Peak 2: 5202	10.5	754.1
Intercept: 0.926	Peak 3: 0.000	0.0	0.000
Result quality : Good			

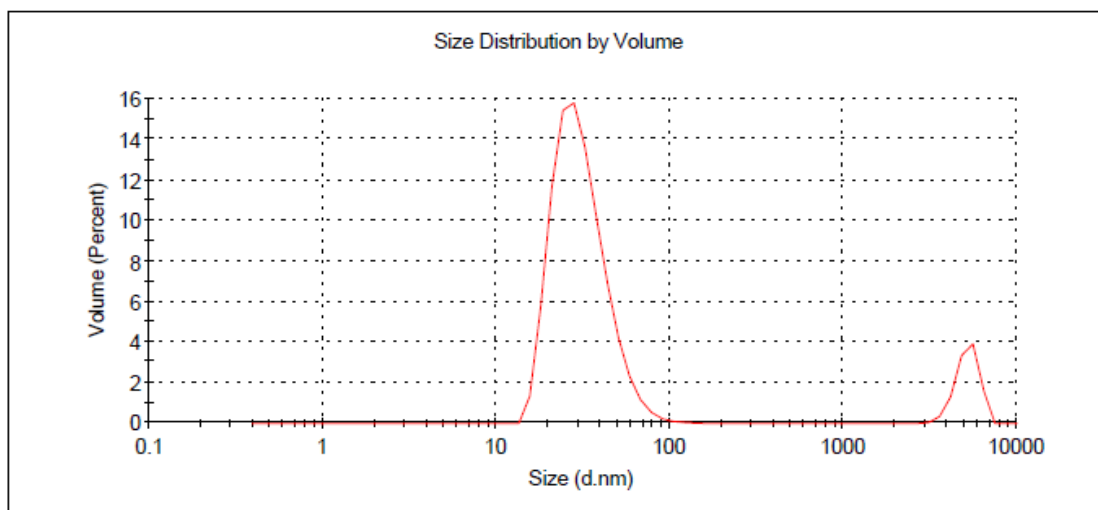


Figure 27: The size distribution profile of GNP-PEG-Tyro3 is shown. Most GNPs in this suspension are 31.76 nm size (Polydispersity index (PDI) = 0.225).

Results

	Size (d.nm):	% Volume:	St Dev (d.nm):
Z-Average (d.nm): 49.66	Peak 1: 31.64	83.2	13.09
Pdi: 0.252	Peak 2: 4853	16.8	923.9
Intercept: 0.903	Peak 3: 0.000	0.0	0.000
Result quality : Good			

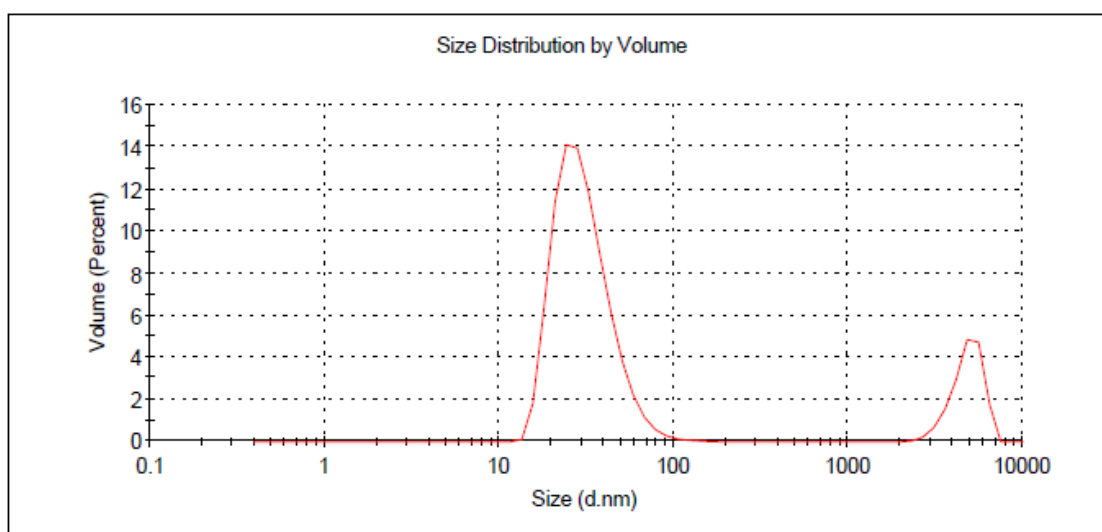


Figure 28:- The size distribution profile of GNP-PEG-(FR- α +Tyro3) is shown. Most GNPs in this suspension are 31.64 nm size (Polydispersity index (PDI) = 0.225).

2.5.6 MALDI-TOF

MALDI-TOF measures the mass-to-charge (m/z) ratio of the molecules. As the laser beam fires upon the sample, the ions so generated travel depending upon their m/z ratio and is detected by the ion detector at the end. This results into vivid spectrum being generated pertaining to that of the molecule of interest. The spectra of 4 GNPs constructs are shown in addition to the IgG standard to compare and measure m/z peaks emanating from each sample (Figure 29) and (Figure 30). Due to the ionisation and desorption, IgG emanates three different m/z peaks $[M+H]^+$, $[M+2H]^{2+}$ and $[M+3H]^{3+}$ (Bian and Olesik, 2017) and (Signor and Erba, 2013). These three were expected to be seen in the single- and double-antibody coated GNPs and absent in GNPs-PEG.

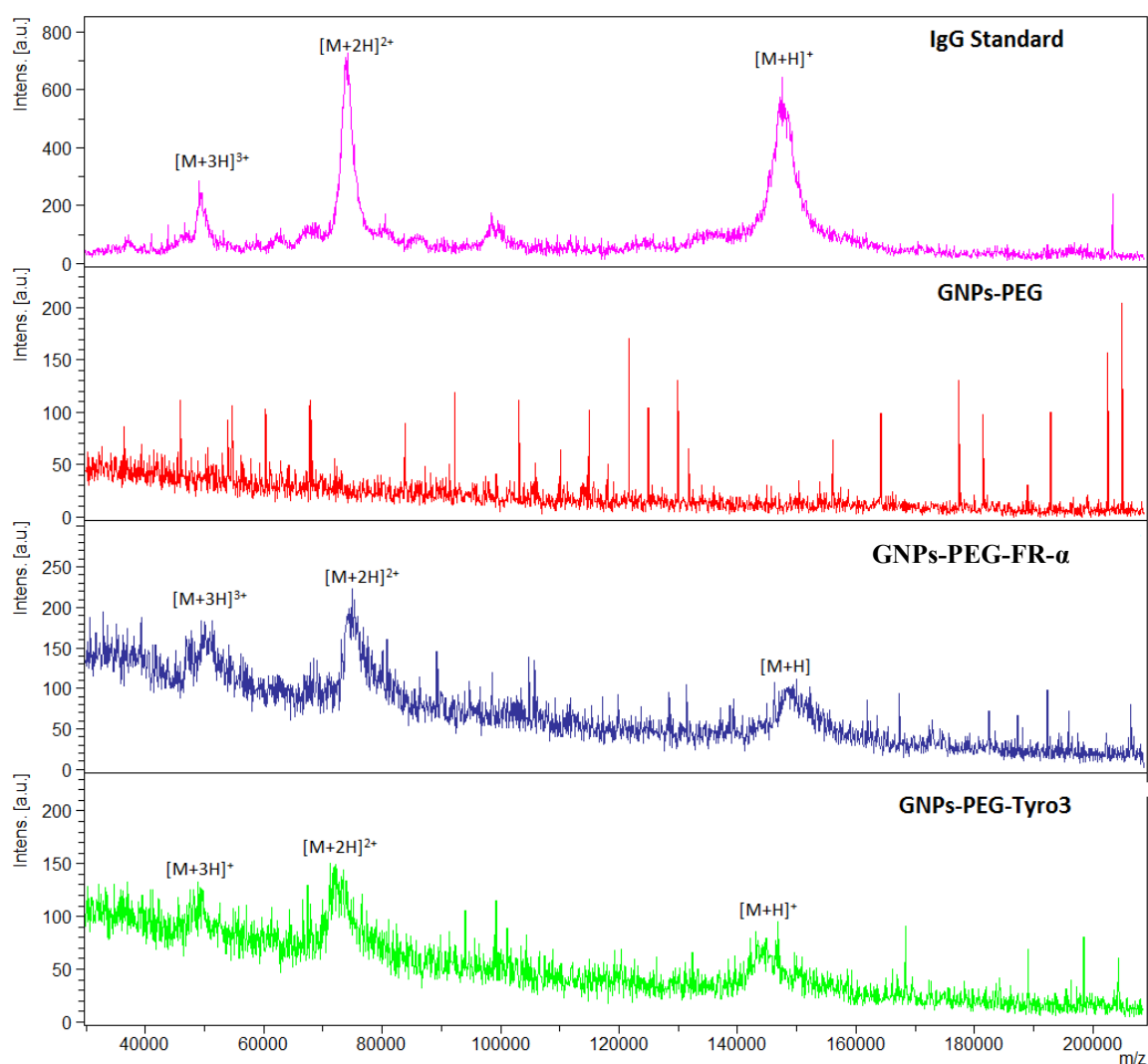


Figure 29: MALDI-TOF spectra for IgG as standard, GNPs-PEG, GNPs-PEG-FR- α and GNPs-PEG-Tyro3 is shown. High intensity peaks for IgG $[M+H]^+ = m/z$ 148,286, $[M+2H]^{2+} = m/z$ 74,478 and $[M+3H]^{3+}$

is seen. Spectra for GNPs-PEG-FR- α and GNPs-PEG-Tyro3 also shows similar peaks, however, they are absent in GNPs-PEG.

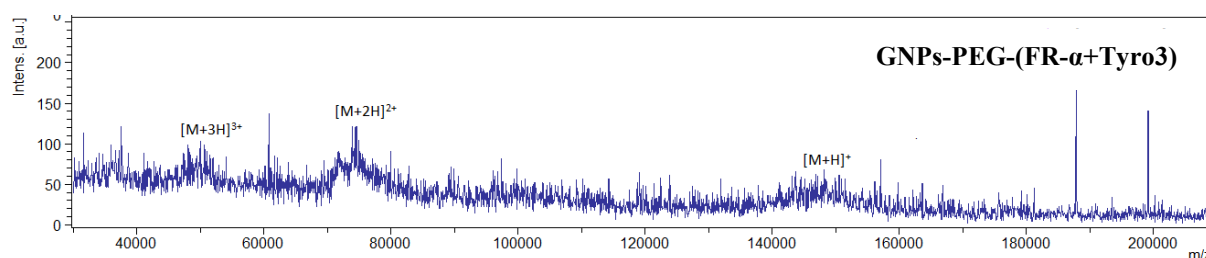


Figure 30: MALDI-TOF spectrum for GNPs-PEG-(FR- α +Tyro3) also shows all three intensity peaks representative of IgG antibody.

2.5.7 Bradford assay

The Bradford assay was used to determine the concentration or amount of the mAbs attached to each of the 3 GNPs constructs indirectly from the plotted IgG standard curve (Figure 31). The concentration in the supernatant was determined. Later, the concentration found in the supernatant was subtracted from the initial concentration (5mg/ml) used to conjugate mAbs to the GNPs-PEG. Table 7 summarises the concentration of mAbs conjugated to each type of GNPs construct. Also, the calculation in determining the amount of antibodies conjugated is also illustrated as below. GNPs-PEG was an exception where no mAbs (IgG) were detected and was also assessed to see if GNPs-PEG let alone give false positive result.

For GNPs-PEG-FR- α , convert the mass into the number of moles using molecular weight of IgG (150,000 g/mol),

$$198.3\mu\text{g} * \frac{1\text{mg}}{1000\mu\text{g}} * \frac{1\text{g}}{1000\text{mg}} * \frac{1}{150,000 \frac{\text{g}}{\text{mol}}} = 1.322e * 10^{-9} \text{ moles IgG}$$

Next, number of moles was converted into number of IgG antibodies,

$$1.322 * 10^{-9} \text{ moles IgG} * \frac{6.023 * 10^{23}}{1} = 7.96 * 10^{14} \text{ IgG particles}$$

Average number of IgG per GNP,

$$\frac{7.96 * 10^{14} \text{ IgG particles}}{1.1 * 10^{14} \text{ GNPs}} = 7.23 \text{ IgG per GNPs}$$

Equation 1: Equation shows the calculation based determination of number of IgG bound to a single GNPs-PEG-FR- α .

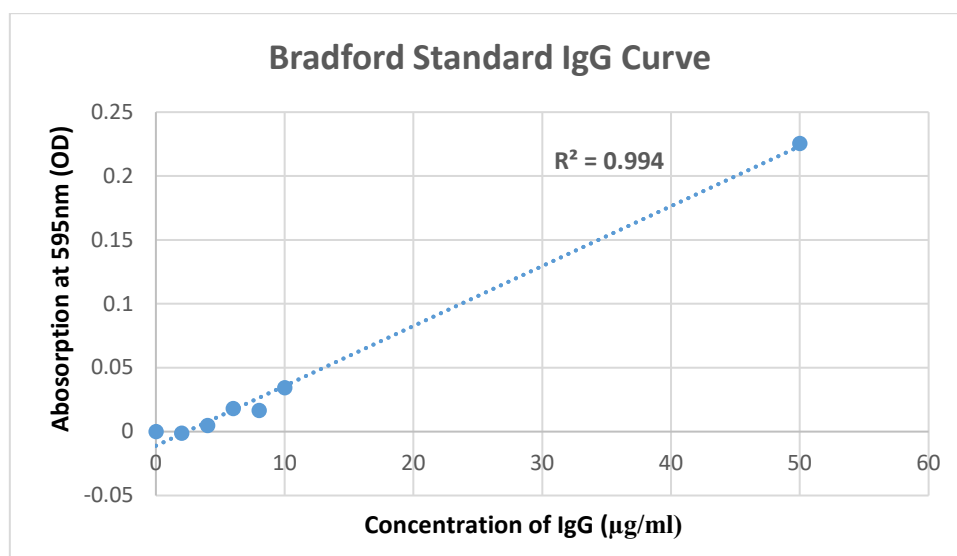


Figure 31:- The graph depicts the IgG concentration standard curve for the purpose of antibody quantification (range = 0 µg/ml to 50 µg/ml).

Table 7: Table illustrates amount of IgG (FR- α and Tyro3) bound to different types of GNPs constructs.

Type pf Gold Nanoparticles	Initial Concentration 5mg/ml or 200µg	Supernatant using Bradford assay	Antibody attached	Antibodies coated to one Gold Nanoparticle
GNPs-PEG	0 µg	0 µg	0 µg	0
GNPs-PEG-FR- α	200 µg	1.7 µg	198.3 µg	7.23
GNPs-PEG-Tyro3	200 µg	2.1 µg	197.9 µg	7.22
GNPs-PEG-(FR- α +Tyro3)	200 µg	0.4 µg	199.6 µg	7.26

2.6 Discussion

2.6.1 Immunocytochemistry (ICC)

For targeting and testing of FR- α and Tyro3 bound GNPs, FR- α and Tyro3 were demonstrated for their expression levels in normal (CRL1790) vs. CRC cell lines (CRL2159 and HCT116). FR- α are membrane bound receptors and were found to be overexpressed in CRL2159 and HCT116 CRC cell lines whereas they were absent in CRL1790 in ICC experiments (Figure 16). FR- α are upregulated in many cancers such as brain, kidney, breast, ovaries including colon (Sega and Low, 2008). Due to the fact that FR- α are absent or minimally expressed in normal colonic tissue, it makes them a potential target for GNPs application in biomedicine (Samadian *et al.*, 2016). Tyro3 is another subtype of tyrosine kinase and a membrane bound receptor along with others such as EGFR, VEGFR, PDGFR, IFF1R and MET (Duan *et al.*, 2016). Tyro3 had been found to be overexpressed in various cancers including CRC (Graham *et al.*, 2014). In ICC experiments, their expression patterns too were concomitant with the literature and were not expressed in CRL1790 compared to CRL2159 and HCT116 (R. *et al.*, 2016) and (Chien *et al.*, 2016) (Figure 17). Therefore, Tyro3 is also a potential candidate for targeting CRC using GNPs. Thus, FR- α and Tyro3 receptors are overexpressed in CRC compared to normal colon cells making them a feasible target for GNPs. The main aim is to simultaneously target the cells exploiting FR- α and Tyro3 upregulation in CRC cells in order to increase the efficiency of GNPs.

2.6.2 UV-Vis spectroscopy

UV-spectroscopy is widely used for determination of nanomaterials diagnostically between 400nm and 800nm (Pal, Tak and Song, 2015). As such, UV-Vis spectrum analysis was carried out to measure the SPR peak or λ_{\max} of all four GNPs constructs: GNPs-PEG, GNPs-PEG-FR- α , GNPs-PEG-Tyro3 and GNPs-PEG-(FR- α +Tyro3). The λ_{\max} of GNPs-PEG was at 513nm (Figure 18), after the attachment with FR- α and Tyro3 mAbs the λ_{\max} of newly synthesised GNPs-PEG-FR- α and GNPs-PEG-Tyro3 were 517nm, respectively. Also, for

GNPs-PEG-(FR- α +Tyro3) the λ_{\max} was at 516nm. These newly formed SPR peaks were associated with spectral red-shifts (4nm and 3nm) due to the change in local refractive index and addition of a protein corona around the GNPs (Kumar, Aaron and Sokolov, 2008). These new SPR peaks in the visible spectrum indicate the interaction and attachment of FR- α and Tyro3 mAbs antibodies to GNPs. Table 6 provides an overview of all the 4 GNPs and their respective UV-Vis spectra. A similar red-shift (<10nm) was also reported wherein EGFR antibody (C225) was conjugated to GNPs with an alkane-thiol linker (Raouf et al., 2012). Furthermore, all GNPs in the suspension were spherical as indicated by a single SPR peak as opposed to two SPR peaks for gold-nanorods (Jazayeri *et al.*, 2016).

2.6.3 Stability assay

UV-Vis does not only characterise GNPs solely but also give detail onto GNPs state of aggregation. Hence, UV-Vis was used to investigate the stability of FR- α and Tyro3 conjugated GNPs by inducing aggregation at various concentrations of NaCl (0.001M - 1M). With different size, shape and surrounding medium of the GNPs, different peaks are observed that characterises the GNPs (Kelly *et al.*, 2003). Different analytes and chemicals can induce aggregation, disaggregation or change of local refractive index resulting a shifting of the SPR band accordingly (Murphy *et al.*, 2008). Aggregation of the GNPs will induce a red shift towards the infrared region of the spectrum and broadening of the SPR peak (Fang *et al.*, 2009). For GNPs-PEG-FR- α (Figure 22), GNPs-PEG-Tyro3 (Figure 23) and GNPs-PEG-(FR- α +Tyro3) (Figure 24) were tested with different concentrations of NaCl for 1 hours to determine the stability in the solution. For all three types of GNPs constructs, no observable red shift or broadening of the peaks was seen indicating all three constructs were highly stable.

2.6.4 DLS

The 4 GNPs samples were further analysed using dynamic light scattering. The size of GNPs-PEG was measured to be 22.97nm (Figure 25). However, after the addition of the FR- α and Tyro3 mAbs, the overall size of the GNPs-PEG-FR- α and GNPs-PEG-Tyro3 increases to

30.78nm (Figure 19) and 31.76nm (Figure 27), respectively. The molecular mass of the antibodies used is ~150kDa and the corresponding size is around 7-10 nm (Jans et al., 2009). This overall increase in the GNPs hydrodynamic diameter of approximately 8nm – 10nm is thus attributed to the attachment of FR- α and Tyro3 antibodies to GNPs. Similarly, hydrodynamic diameter of GNPs-PEG-(FR- α +Tyro3) (Figure 28) was 31.64nm confirming the attachment of FR- α and Tyro3 mAbs to GNPs. Additionally, Polydispersity Index (PDI) for all types of GNPs is <0.3 indicating a narrow monodispersed GNPs suspension. Table 6 summarises the hydrodynamic size of all 4 GNPs along with respective λ_{\max} values.

2.6.5 MALDI-TOF-MS analysis

Conjugation of FR- α and Tyro3 mAbs to GNPs was qualitatively assessed via MALDI-TOF mass spectrometry. MALDI-TOF-MS is a soft ionisation technique which has garnered much attention in recent years for its analytical approach. It is used widely due to its accuracy, reproducibility as well as sensitivity and high throughput (Resemann *et al.*, 2010). Intensity peaks were confirmed using IgG as standard. Three intensity peaks were generated $[M+H]^+$, $[M+2H]^{2+}$ and $[M+3H]^{3+}$ (Figure 29) from the IgG as shown previously (Bian and Olesik, 2017) and (Signor and Erba, 2013). Out of three, IgG is mainly denoted by two main peaks $[M+H]^+$ and $[M+2H]^{2+}$ corresponding to single protonated ($m/z = 148,286$) and double protonated ($m/z = 74,478$) IgG molecules (Lapolla *et al.*, 2000) and (Lapolla *et al.*, 1997). For all the antibody-coated GNPs (Figure 29) and (Figure 30), similar peaks were also shown which confirmed the attachment of the antibodies to GNPs-PEG. As a proof of principle, GNPs-PEG (Figure 29) was also analysed using MALDI-TOF and showed no similar IgG peaks in the sample due to the absence of the antibodies. This further confirmed those peaks were emanating solely from IgG and not generated from either the GNPs, polyethyleneglycol chain or the matrix used to analyse the GNPs.

2.6.6 Bradford assay

Bradford assay was conducted to estimate the number of antibodies (IgG) bound to each of the antibody conjugated to GNPs. Due to the ability of Bradford reagent to turn the protein suspended in the solution by interacting its arginine, histidine, phenylalanine, tryptophan and tyrosine amino acids, the concentration of FR- α and Tyro3 mAbs (IgG) in the sample was determined. The covalently conjugated GNPs were separated from the supernatant by centrifugation and subsequently analysed by Bradford assay. The obtained concentration was subtracted from the initial concentration to estimate the concentration bound to GNPs and, consequently, the number of IgG per GNP. Using the method illustrated in (Tripathi and Driskell, 2018), Table 7 summarises the number of FR- α and Tyro3 IgG bound to single GNP in all GNPs constructs. Approximately, 199 μ g of IgG (mAbs) were bound to each of the single- and double-antibody conjugated GNPs which corresponds to ~ 7 antibodies per GNPs (Equation 1). A similar approach and results were obtained (Filbrun and Driskell, 2016) wherein number of mouse IgG to GNPs were detected using the Bradford assay. The number of antibody attached to single GNPs is consistent as quantified in two separate studies (S. Kumar, Aaron and Sokolov, 2008) and (Eck *et al.*, 2008). For Bradford analysis, synthesised GNPs-PEG was also centrifuged, and supernatant analysed via the assay to see if GNPs-PEG alone can give a false-positive result. The supernatant showed no visible colour change nor absorbance change deducting that no IgG were present. Also, analysis suggested that PEG does not react with the dye to yield false-positive result.

2.7 Conclusions

Overexpression of receptor Tyro3 and FR- α was demonstrated in human colon epithelium (CRL1790) and CRC cell lines (CRL2159 and HCT116). Tyro3 belongs to the TAM receptor family which also includes Axl and Mer receptors. TAM family of receptors are tyrosine kinase, which mediates cell growth, proliferation, migration and invasion. Tyro3, especially, has shown its EMT transforming capability in CRC and as a potential target to increase drug sensitivity in the CRC (Chien *et al.*, 2016). Tyro3 have been observed to have upregulated in CRC cells compared to colon epithelium cell line. Similarly, expression of FR- α among CRL1790, CRL2159 and HCT116 cell lines was also determined. FR- α overexpression was restricted to only CRC cell lines and was hardly expressed in colon epithelium cell line. Like Tyro3, FR- α is also overexpressed in many cancer including colon and its selective expression on CRC makes it a viable target for GNPs. Therefore, Tyro3 and FR- α were chosen to target simultaneously for increasing the efficacy of GNPs.

Moreover, synthesis of all 4 GNPs constructs was shown and characterised using UV-vis spectroscopy where red-shift in the visible spectrum (400nm-800) and increase in size have confirmed the attachment of FR- α and Tyro3 mAbs to respective GNPs constructs. All four GNPs constructs were also qualitatively analysed by using MADLI-TOF via analysing the protonated ions formed. Three distinguished m/z IgG peaks were seen $[M+H]^+$, $[M+2H]^{2+}$ and $[M+3H]^3$ that verified the conjugation of FR- α and Tyro3 to single- and double-antibody coated GNPs. To complement it, the Bradford assay was also carried out that quantified the number of FR- α and Tyro3 (IgG) bound to each of the antibody conjugated GNPs. As per the calculations, approximately 7 antibodies were found to have attached to GNPs. GNPs-PEG did not show any attachment as denoted by no visible colour or absorbance change. The absorbance was close to deionised water used as a blank in the Bradford assay. These GNPs constructs will be analysed for their internalisation efficacy in chapter 3 to test if the GNPs-PEG-(FR- α +Tyro3) has greater internalisation potential compared to GNPs-PEG-FR- α and GNPs-PEG-

Tyro3. Chapter 4 will demonstrate the development of 3D *in vitro* normal and CRC models. Chapter 5 will be focused on testing the efficacy of GNPs in the 3D cultured normal and CRC models and chapter 6 will discuss the results gathered from all the experiments.

CHAPTER 3

Internalisation of GNPs in 2D Normal and CRC cells

3.1 Aim

The aim of this chapter is to investigate the internalisation efficiency of all 4 GNPs constructs: GNPs-PEG, GNPs-PEG-FR- α , GNPs-PEG-Tyro3 and GNPs-PEG-(FR- α +Tyro3). To achieve this, an analytical technique Inductively Coupled Plasma-Optical Emission Spectrometry (ICP-OES) was utilised to quantify the GNPs internalised in all three cell lines: one normal and two CRC cell lines. Moreover, GNP localisation in the cells was visualised via the use of confocal microscopy by fluorescently labelling GNPs.

3.2 Introduction

To determine the efficiency of GNPs internalised by the cells or tissue for biomedical application, it must be quantified as well as it is imperative to understand its localisation within the cells. Furthermore, it is also indispensable to gather the evidence that GNPs does not interact with other cells or tissue non-specifically (Drasler *et al.*, 2017). To overcome this, researchers have utilised a wide array of analytical techniques to quantify internalised GNPs and imaging techniques to understand spatial distribution of GNPs within the cells (Marquis *et al.*, 2009). Therefore, to begin with, this chapter discusses the uptake of fluorescently labelled GNPs in normal vs CRC cell lines to visualise GNPs *in vitro*. This is normally done via fluorescently labelling GNPs using fluorescein isothiocyanate (FITC) or Texas red to visualise cellular internalisation of GNPs in the cells *in vitro* (Chnari *et al.*, 2006). Imaging the GNPs in the cells will help us evaluate the localisation of the GNPs qualitatively. Confocal microscopy was employed in order to image fluorescently labelled GNPs in the cells. However, using imaging technique, single GNPs cannot be differentiated and rather one signal could easily be several GNPs clustered together (Drasler *et al.*, 2017). Additionally, imaging only focuses on the spatial distribution of the GNPs within the cells and does not retrieve the information on the amount that had been internalised. Therefore, to supplement imaging, inductively coupled plasma – optical emission spectroscopy (ICP-OES) was also used in conjunction with confocal microscopy.

To study localisation via confocal microscopy, all antibody-coated GNPs constructs were conjugated with FITC. Also, all 4 GNPS constructs was quantified in all three cell lines and their uptake efficiency was compared with each other within the same cell line. For GNPs-PEG, GNPs-PEG-FR- α , GNPs-PEG-Tyro3 and GNPs-PEG-(FR- α +Tyro3) uptake, their concentrations were predetermined using ICP-OES and all 4 GNPs constructs ranging 0ng – 50ng were allowed to incubate with all three cell lines up to 4 hours. Conditions were kept similar for both the confocal imaging and ICP-OES experiments in order to investigate internalisation efficiency of all 4 GNPs constructs.

3.3 Methods and materials

3.3.1 Cell culture

All three cell lines CRL1790, CRL2159 and HCT116 were cultured using appropriate culture media as mentioned in chapter 2 until flasks were 80% - 90% confluent.

3.3.2 Uptake in CRL1790, CRL2159 and HCT116

All 4 GNPs constructs were utilised to investigate the uptake efficiency by all three cell lines via confocal imaging as well as ICP-OES. 0ng – 50ng of each type of GNPs was incubated with all three cell lines for 4 hours. For confocal imaging, a fluorescent labelling method was introduced to enable visualisation in the cell cytosol whereas trace level of gold concentration was determined using ICP-OES elemental analysis.

3.3.3 Preparation of FITC labelled GNPs

Due to the fact that FITC recognises and binds to primary amine residues found on mAbs, all antibody-coated GNPs were reacted with FITC for 24 hours in the dark on an orbital shaker to enable visualisation using confocal microscopy (Zhang *et al.*, 2010). FITC labelled GNPs conjugates were then centrifuged using 10,000 MW Amicon® centrifugal filter tubes for 30 minutes to remove excess FITC from the suspension. GNPs-PEG was the only exception since it does not provide a supporting amino group to bind FITC and, thus, was not included in the confocal imaging experiment. Since confocal imaging is used to qualitatively and solely assess the localisation of single- and double-antibody coated GNPs in the cytoplasm, inclusion of GNPs-PEG would be an irrelevant experiment. ICP-OES was used to quantify the uptake of GNPs-PEG in all three cell lines as a control.

3.3.4 ICP-OES

Quantification of GNPs in nanograms (ng) was carried out using ICP-OES (iCAP 6000 Series). The conditions of ICP-OES being operated are listed in (Table 8). A gold standard calibration curve ($R^2 = 0.9946$) was plotted using gold standard solution in 5% *aqua regia* (3 HCL: 1 HNO₃) in de-ionised water between the range of 0mg/L – 10mg/L. All three cells lines

were grown and passaged as mentioned above and later aliquoted in the 6-well plates at approximately 100,000 cells/well. Cells were allowed to grow until they were 80%-90% confluent. The spent media was aspirated and 2ml of fresh medium containing (10ng – 50ng) of GNPs-PEG, GNPs-PEG-FR- α , GNPs-PEG-Tyro3 and GNPs-PEG-(FR- α +Tyro3) was aliquoted in the wells containing all three cell lines and incubated for 4 hours at 37 °C and in 5% CO₂. After incubation, cells were washed 4 times with 1X PBS to remove free and loosely bound GNPs. Later, the cells in the well were digested using freshly prepared 1ml *aqua regia* for 1 hour. The digested sample with *aqua regia* was later brought up to 10ml by adding de-ionised water and transferred in 15ml centrifuged tubes. Respective samples were then subjected to the ICP-OES experiment to measure the uptake of GNPs. As negative control, each of the 3 cell lines had one well without GNPs.

Table 8: Operating conditions of ICP-OES

Nebuliser	Cross-Flow
Spray Chamber	Glass-Scott type
Power (Watts)	1150 Watts
Coolant gas (L min⁻¹)	12 L min ⁻¹
Auxillary gas (L min⁻¹)	0.5 L min ⁻¹
Nebuliser gas (L min⁻¹)	0.7 L min ⁻¹
Viewing	Axial
Sample Uptake (ml)	1ml
Analyte wavelength	242.795nm
Measurement time per replicate (seconds)	30s
R²	0.9946

3.3.5 Confocal microscopy

All 3 fluorescently-labelled GNP constructs, GNPs-PEG-FR- α , GNPs-PEG-Tyro3 and GNPs-PEG-(FR- α +Tyro3) were subjected to confocal microscopy. Colon epithelium

(CRL1790), Duke's B Colorectal Carcinoma (CRL2159) and colorectal carcinoma (HCT116) were grown and cultured as mentioned before. After trypsinisation, 10,000 cells were pipetted onto the sterilised covers-slips in the 6-well plates and placed in the incubator at 37°C at 5% CO₂ to reach 80%-90% confluence. Later, all 3 antibody-coated GNPs (50ng) was aliquoted in all three cell lines and incubated for 4 hours. For controls, one well of each cell line had no GNPs incubated. Thereafter, the media was discarded, and the non-bound GNPs was washed away by using 1X PBS, 4 times each. 4% paraformaldehyde (PFA) was then pipetted to fix the cells for 30 minutes. The cells were again washed using 1X PBS twice and cover-slips were mounted onto the slides using DAPI (Product no. H-1200) based mounting media. Internalisation of FITC bound GNPs was then visualised using Leica confocal microscopy.

3.3.6 Statistics

Raw data generated were analysed via generating graphs using Microsoft Excel 2016. Data gathered through uptake experiments were analysed using parametric testing: one-way analysis of variance (ANOVA) and student's unpaired *t*-test. ANOVA was carried out where two or more group of means were involved and students unpaired *t*-test where only two group of means were compared. All experiments were biological triplicates and the level of significance was considered $p \leq 0.05$.

3.4 Results

3.4.1 ICP-OES

To assess the uptake of all GNPs constructs into the cell, ICP-OES was chosen due to its sensitivity in tracing abundant gold. GNPs internalised by the cell were also supplemented by confocal microscopy shown later. All three cell lines were subjected with the same treatment in both the techniques; cell density, exposure to GNPs and amount of GNPs incubated. However, whereas ICP-OES was used to quantify the GNPs, confocal microscopy was used to supplement and demonstrate the localisation of GNPs in the cells. Cell internalisation studied via ICP-OES was first subjected to *aqua regia* digestion and subjected to ICP-OES.

ICP-OES results represented by Figure 32, Figure 33 and Figure 34 are of cell lines CRL1790, CRL2159 and HCTL116, respectively. The graph shows the treatment of each GNP construct in 5 different amounts (10ng – 50ng) for each of the three cell lines. The uptake of all GNPs in CRL1790 were minimum and saturated (below 10ng). In comparison to CRL1790, CRL2159 and HCT116 has the most internalisation for all antibody-coated GNPs (single- and double-). For GNPs-PEG-Tyro3, GNPs-PEG-FR- α and GNPs-PEG-(FR- α +Tyro3), the graph depicts the increase in uptake in a concentration-dependent manner in CRL2159 and HCT116. GNPs-PEG was shown at different levels for all three cell lines, however, HCT116 has shown to have internalised the most.

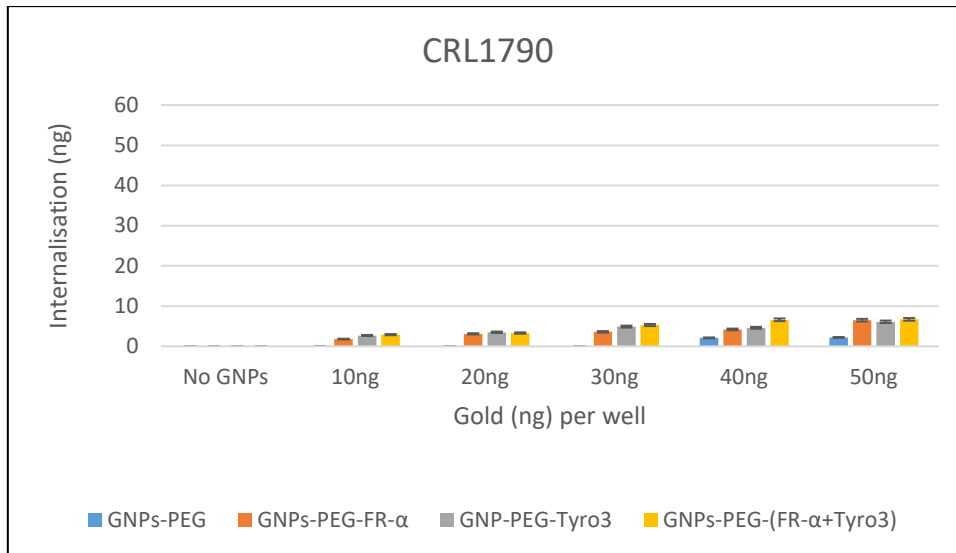


Figure 32: Internalisation all 4 GNPs-constructs in CRL1790 cell lines. Internalisation is shown for each well. Experiments were done in triplicates (n=3). Error bars indicates SD. ANOVA = $p < 0.05$.

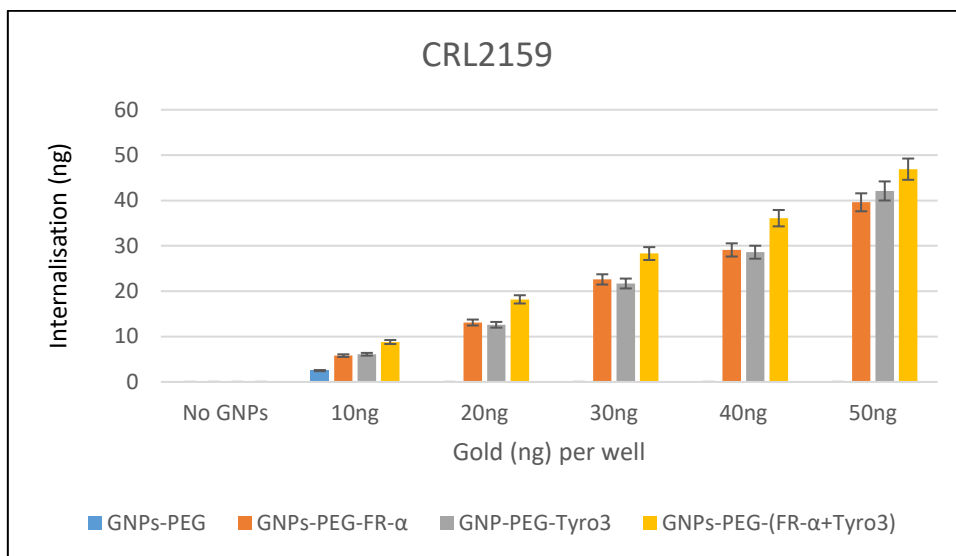


Figure 33: Internalisation all 4 GNPs-constructs in CRL2159 cell lines Internalisation is shown from each well. Experiments were done in triplicates (n=3). Error bars indicates SD. ANOVA = $p < 0.05$.

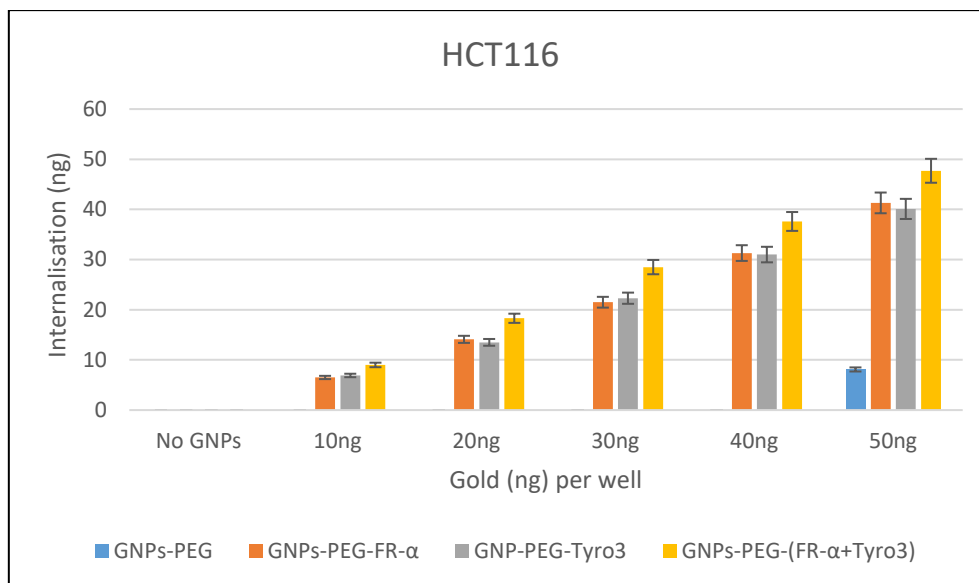


Figure 34: Internalisation all 4 GNPs-constructs in HCT116 cell lines Internalisation is shown from each well. Experiments were done in triplicates (n=3). Error bars indicates SD. ANOVA = $p < 0.05$.

3.4.2 Confocal microscopy

To complement ICP-OES results, internalisation and localisation of antibody-coated GNPs construct was studied via confocal microscopy. All three cell lines were incubated with GNPs construct was studied via confocal microscopy. All three cell lines were incubated with GNPs-PEG-Tyro3, GNPs-PEG-FR- α and GNPs-PEG-(FR- α +Tyro3). GNPs-PEG was not included in the experiment due to its inability to pair with FITC as explained above. Therefore, confocal microscopy only entails the study of all three antibody-coated GNPs and their subsequent localisation. Unlike ICP-OES, only 50ng of each of the antibody-coated GNPs was studied since it was the most internalised amount in CRL2159 and HCT116 to visualise *in situ*. The fluorescent signal in the figures represents the clusters of GNPs (in green) and nuclei of the cell (stained in blue). All three antibody-coated GNPs were shown to have internalised in the cytoplasm of the cell or are in the periphery of the cell wall.

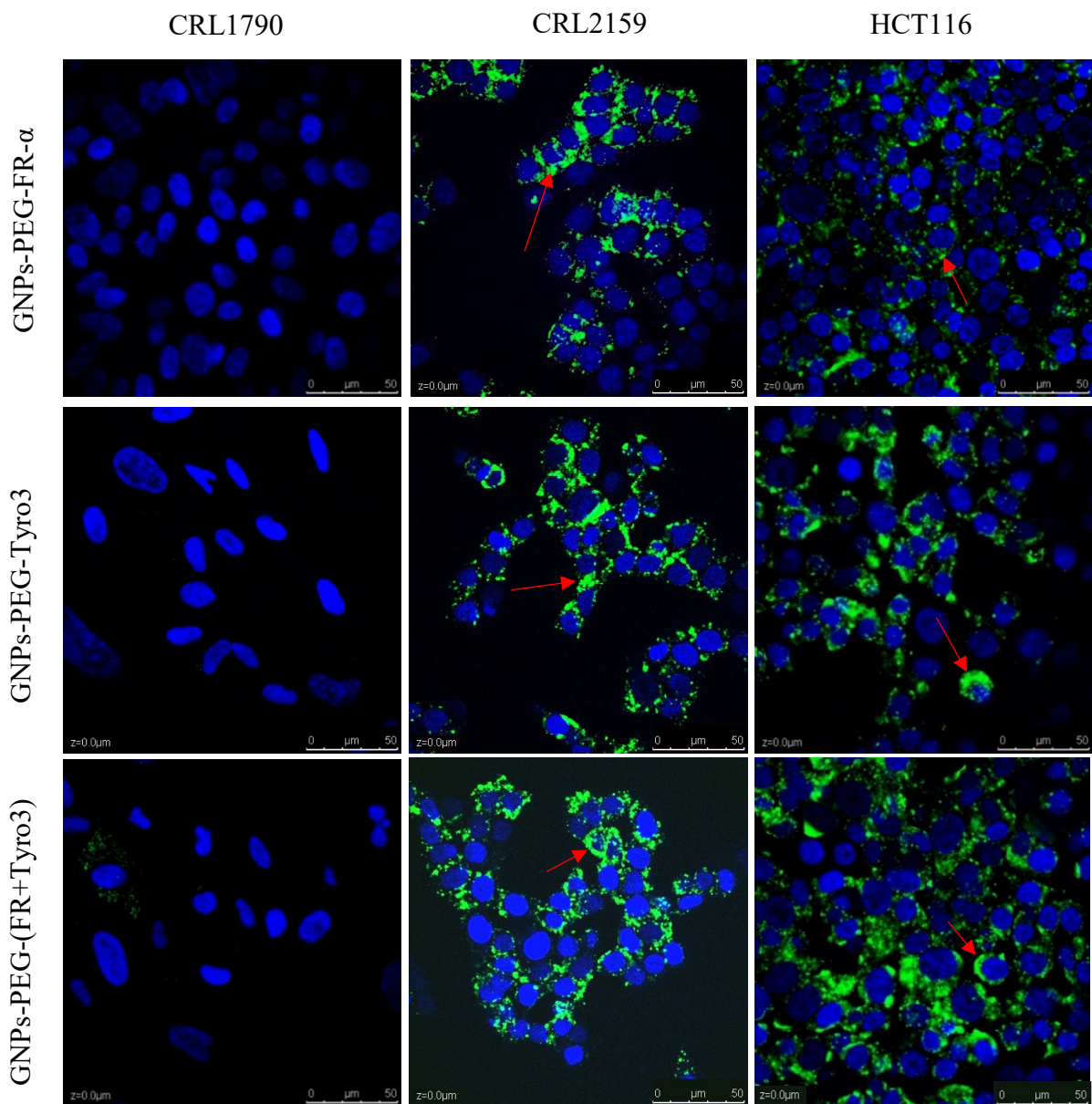


Figure 35: Figure shows the internalisation of GNPs-PEG-FR- α , GNPs-PEG-Tyro3 and GNPs-PEG-(FR- α +Tyro3) (red arrows) at 50ng in all three cell lines. Nuclei were stained in blue and GNPs in green. Experiments were repeated in triplicates (n=3). Scale bar = 50 μ m. Magnification 40X.

3.5 Discussion

In CRL1790, there was no uptake of GNPs-PEG until 30ng volume. Due to a low number of Tyro3 and FR- α receptors, the internalisation of all antibody-coated GNPs remained below 10ng (Figure 32). However, there was a visible difference of non-specific uptake between GNPs-PEG and all antibody-coated GNPs. This could be explained due to the RME mechanism mediated by targeted FR- α and Tyro3 receptors. Although there was marginal increase of GNPs uptake with increase in GNPs amount, there is no statistical difference seen between single antibody-coated GNPs vs. double antibodies-coated GNPs ($p>0.05$) ($n=3$). Again, this pattern can be attributed to the low numbers of FR- α and Tyro3 receptors in CRL1790.

For CRL2159, with increase in amount of different types of antibody-coated GNPs, there was a concomitant increase in uptake. Moreover, compared to CRL1790, and due to overexpressed FR- α and Tyro3 receptors, the overall uptake of GNPs into CRL2159 has increased (Figure 33). For example, at 20ng, GNPs-PEG-FR- α and GNPs-PEG-Tyro3 is above 10ng in CRL2159 compared to less than 10ng in CRL1790 ($p<0.05$). Also, unlike CRL1790, double antibody-coated GNPs (GNPs-PEG-(FR- α +Tyro3)) has surpassed the uptake rate of single antibody-coated GNPs for every amount used ($p<0.05$). This has shown that simultaneous targeting of FR- α and Tyro3 receptors has increased the efficiency of GNPs in CRC cells. Additionally, there was no statistical difference ($p>0.05$) seen between GNPs-PEG-FR- α and GNPs-PEG-Tyro3 implicating that Tyro3 receptors are equally vital in cell internalisation and uptake of GNPs as FR- α . This is the novel finding as Tyro3 receptors has never been attempted in assessing the internalisation efficiency of GNPs.

Internalisation of all 4 types of GNP in HCT116 cell line is shown in Figure 34. Like CRL2159, with an increase in amount of GNPs incubated, the rate of GNPs uptake also increases. Also, single antibody-coated GNPs (GNPs-PEG-FR- α & GNPs-PEG-Tyro3) have

greater internalisation efficacy than non-specific GNPs-PEG, which is absent until 40ng GNPs was reached. At 50ng, there is an uptake of GNPs-PEG or non-specific internalisation. This can be due to the high number of GNPs incubated with HCT116 that GNPs-PEG internalised and interacted with the cell line non-specifically. However, the uptake of GNPs-PEG was very minimal. In turn, double antibody-coated GNPs (GNPs-PEG-(FR- α +Tyro3)) has even greater potential in internalisation than single antibody-coated GNPs ($p<0.05$) proving double antibody-coated GNPs have higher internalisation efficiency compare to single antibody-coated GNPs.

Number of research has been published focusing on improving the efficacy and cellular uptake of GNPs in cancer cells (Patra *et al.*, 2018). In the current project, the increase in overall uptake of GNPs due to simultaneous targeting is ~10%. Likewise, in an independent study, peptides and photosensitizer phthalocyanine 4 (Pc 4) conjugated GNPs were used as photodynamic therapy using EGFR and transferrin receptors to treat glioblastoma multiform, a subset of glioma. Uptake of GNPs *in vitro* in this regards was 2-fold more compared to targeting EGFR and transferring receptors alone in U87 cell line (Dixit *et al.*, 2015). However, a point to be noted that the quantification was done using confocal microscopy alone and not ICP-OES/MS. Quantification done this way using fluorescence intensity can overestimate the number of GNPs internalised. This is because single GNPs cannot be differentiated using fluorescence and rather one signal could easily be several GNPs clustered together (Drasler *et al.*, 2017). In another investigation, using rodent and dose-dependent studies, only ~12% of increase in GNPs concentration was found (Ouyang *et al.*, 2020). Similarly, an external magnetic field and endovascular targeting was applied to increase localised concentration of magnetite nanoparticles near tumour. This increased overall incubation time and bioavailability of nanoparticles with tumour. As a result, there was 4-fold uptake of nanoparticle in mice. However, the size of the nanoparticles were in μm range and have subsequently been

accumulated in vital organs such as lung, liver, spleen and kidney. This can result in induced toxicity in a long-term (Mayorova *et al.*, 2020).

An additional experiment was conducted to investigate if GNPs can bind to the plastic surface of 6-well plate non-specifically (Figure 55). 50ng of every GNPs samples were processed through the same conditions as confocal microscopy and ICP-OES and washed stringently; except no cells were attached to the well of the 6-well plate surface. Only marginal GNPs signal intensity was detected ensuring that GNPs do not stick to the plastic surface ($p < 0.05$) (Figure 55). Furthermore, another experiment was carried out to explore if the matrix effect was introduced by using *aqua regia* for digesting the sample. All 4 GNPs at 50ng with no cells were subjected through ICP-OES with and without *aqua regia* (Figure 56). The recovery was nearly the same ($p > 0.05$) as that of the original concentration concluding that *aqua regia* do not interfere with the signal generated by ICP-OES.

After the quantification of internalised GNPs, it was necessary to investigate the localisation of antibody-conjugated GNPs. GNPs (at 50ng) labelled with FITC were incubated with respective cell lines to qualitatively analyse their uptake and localisation in the cells. 50ng amount was chosen as the fluorescent signals were constant compare to other amounts used and also were most internalised amount using ICP-OES. In the present experiment, GNPs-PEG-FR- α , GNPs-PEG-Tyro3 and GNPs-PEG-(FR- α +Tyro3) were successfully used to target CRC cells using FR- α and Tyro3 receptors as quantified by ICP-OES. Due to FITC being attached to the GNPs, they were visualised with ease using confocal microscopy (Figure 35). GNPs were found to have located in the cytoplasm of the cell and its periphery. CRL1790, CRL2159 and HCT116 were used to investigate cell uptake of all antibody-coated GNPs. CRL1790 gave reduced (non-specific binding) to no signal at all due to low to no expression of FR- α or Tyro3 receptors as proven in chapter 2. On the other hand, CRL2159 and HCT116 had overexpressed FR- α & Tyro3 receptors and, therefore, had more internalisation of GNPs

which was also supported by ICP-OES (Figure 33) and (Figure 34). Similar results can also be seen with strong green fluorescence associated with GNPs uptake using confocal microscopy (Figure 35). For comparison, cells from all three cell lines without GNPs are also shown in Figure 57 in appendix. In a separate study, electron microscopy had demonstrated 4nm and 6nm internalisation by HeLa cells and were sub-localised in endosomes and lysosomes (Kim *et al.*, 2015). In another experiment to demonstrate the uptake, HeLa cells were incubated with folate-conjugated GNPs. GNPs were shown via confocal and electron microscopy to be localised in the cytoplasm due to overexpressed folate receptors (Zhang *et al.*, 2010). These results strongly suggests the presence of GNPs in the cytoplasm was due to receptor mediated endocytosis (RME) via invagination of the plasma membrane in the cytoplasm. Results as shown in Figure 35 are also in line with the experiments conducted here and previous literature as stated above confirming the hypothesis that simultaneous targeting of FR- α and Tyro3 receptors has led to an increase in cellular uptake of GNPs.

3.6 Conclusion

To increase GNP uptake efficiency two distinct receptors were chosen; FR- α and Tyro3 to be targeted simultaneously. ICP-OES results confirmed that GNPs-PEG-(FR- α +Tyro3) were the most internalised in CRL2159 and HCT116 cell lines. This was further supplemented with strong fluorescent signals associated with the GNPs inside the cytoplasm of the cells. Another observation was also made that Tyro3 has similar internalisation efficiency as FR- α . GNPs-PEG-FR- α and GNPs-PEG-Tyro3 had almost no difference in uptake of GNPs ($p>0.05$) in cancer cells. GNPs-PEG were not internalised due to absence of mAbs attached to it although minimum uptake was seen which can be attributed to non-specific interaction between GNPs-PEG and the cells. Hence, using ICP-OES and confocal microscopy, it was concluded that targeting FR- α and Tyro3 simultaneously can result into uptake of GNPs at a higher threshold. Next chapter will demonstrate the development of 3D *in vitro* normal and CRC models.

CHAPTER 4
Development of 3D
Normal and CRC *in vitro*
models

4.1 Aim

The aim and objective of this chapter is to develop normal vs. CRC 3D *in vitro* models in order to test the internalisation efficiency of the GNPs in 3D environment. Three different cell lines were chosen to make the 3D *in vitro* models; human colon epithelium (CRL1790), Duke's B Colorectal carcinoma (CRL2159) and Colorectal Carcinoma (HCT116). Immunohistochemistry technique was utilised to stain cytokeratin 7 and 20 distribution in these models for validation.

4.2 Introduction

There is a constant reliance on 2D cell culture for *in vitro* experiments and drug discovery in the present day. While 2D cell culture provides an efficient cell growth in real time, it is limited by only 2-dimensional growth of the cells in a monolayer on the glass flasks or petridishes. Such an organisation of the cell does not reflect the overall structural environment within which the tumour grows. *In vivo*, the tumour is facing the extracellular matrix (ECM) as well as it is contact with other cell types (Figure 36). 2D cell culture cannot provide such an organisation. Hence, concomitant results coming from such 2D scenarios are not accurate (Birgersdotter, Sandberg and Ernberg, 2005). Also, cells *in vivo* perform differently in 3-dimensions (3D), the response to any given stimulus is highly complexed relative to that occurring in conventional 2D cell culture (Burdick and Vunjak-Novakovic, 2009). To overcome these scenarios, *in vitro* 3D cell cultures are utilised that represent and mimic more closely the actual microenvironment of cancer compared to 2D cell cultures. 3D cell cultures produce *in vivo* like cell arrangements and are also referred to as 'spheroid' or 'organoid cell culture' (Duval *et al.*, 2017). 3D *in vitro* tumour models have an essential role in tumour biology and can provide valuable insights into cancer research. Because behaviour of cells cultured in 3D are more reflective of a tumour and its surrounding microenvironment *in vivo* than its 2D counterparts, it gives nearly-similar responses to any given stimuli. Cells cultured in 3D also vary in morphological as well as physiological properties compared with

2D cell culture (Baharvand *et al.*, 2006). Key features and characteristics of 2D vs 3D models are listed in Table 9.

Table 9: Table shows key differences of cells grown in 2D vs. 3D cell culture systems.

CELL CHARACTERISTICS	2D	3D	REFERENCES
Morphology	Flattened and grown in monolayers	Natural shape is retained in 3D arrangements of the cells	(Huang <i>et al.</i> , 2013)
Proliferation	Cells proliferate much faster compared to <i>in vivo</i>	Proliferates at different rates depending on the cell types and types of 3D culture used	(Xu <i>et al.</i> , 2012)
Exposure to medium/drugs	Cells in monolayers are equally exposed to nutrients, drugs found in the media	Due to the 3D growth of the cells, exposure to the media and drugs are site specific	(Yip and Cho, 2013)
Stage of cell cycle	More than 90% of the cells will be in the same stage of the cell cycle	3D cell culture models, e.g., spheroid, will exhibit different stages of the cell cycle: proliferating, quiescent, hypoxic and necrotic cells	(Tibbitt and Anseth, 2009)
Gene/protein expression	Displays differential gene and protein expressions compared to <i>in vivo</i> models	Cells in 3D arrangements often express genes and proteins similar to that of <i>in vivo</i> tissue and organs	(Price <i>et al.</i> , 2012)
Drug Sensitivity	Cells treated with a particular drug will appear to have more effect than <i>in vivo</i>	Cells are found to be more resistant to treatment compared to their 2D counterparts; 3D models better represent <i>in vivo</i> cells and tissue response	(Hongisto <i>et al.</i> , 2013)

The addition of the third dimension in this arrangement is the driving mechanism

behind the 3D cell culture system. It permits spatial and temporal organisation of the receptors on the cell's surface used in communicating with other cells. Such 3D structural design allows for signal transduction from outside to inside of the cells efficiently, thereby influencing cell behaviour and gene expressions (Shield *et al.*, 2009). Moreover, cells grown in 2D cell cultures are flattened and stretched. Such flawed structural organisation of the cells affects cell proliferation, differentiation, apoptosis and gene and protein expressions. Consequently, they do not behave in a similar manner as they would *in vivo* microenvironment (Huh, Hamilton and Ingber, 2011). Additionally, 3D cell culture offers many advantages over its 2D counterparts in testing anti-cancer drugs *in vitro*. Such advantages are 1) oxygen and nutrients gradients 2) increased cell-to-cell interactions due to organised 3D cell culture 3) non-uniform exposure of the cells 4) Extracellular matrix to cell interactions 5) different rates of cell division (Lovitt, Shelper and Avery, 2014)

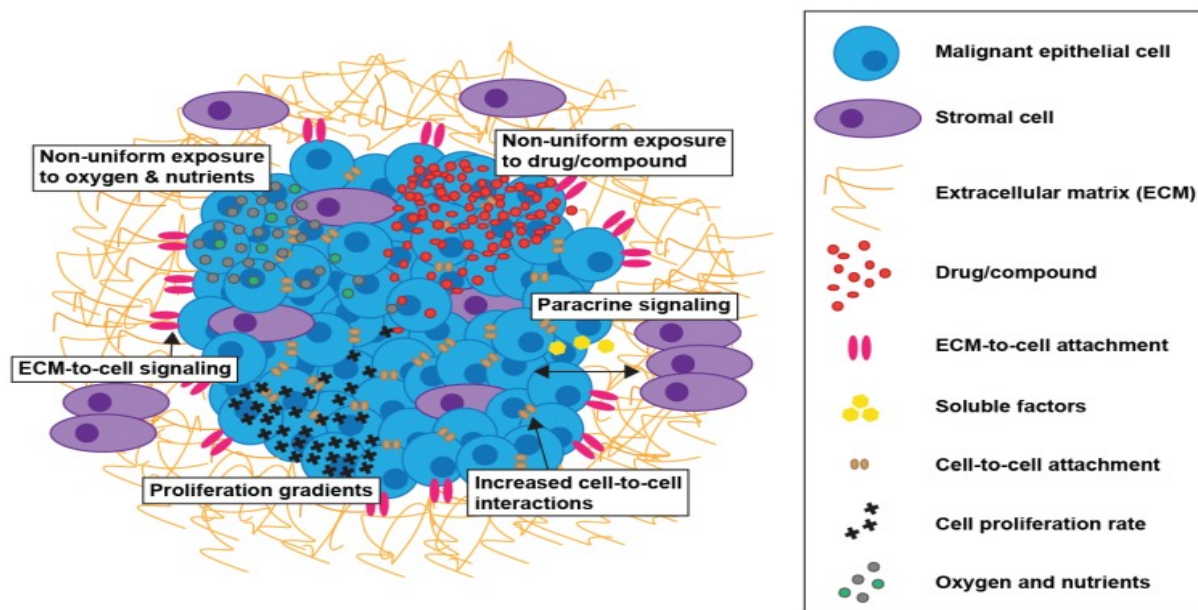


Figure 36: - Schematic representation shows tumour and its interaction with surrounding microenvironment (Lovitt, Shelper and Avery, 2014).

An ideal 3D culture model will manifest tissue-specific physiological and pathophysiological features of the disease as well as specific tumour microenvironment where cells can proliferate, aggregate and differentiate (Griffith and Swartz, 2006). Currently, not all

3D culture models meet these criteria as above and have their own strengths and limitations. There are different 3D cell culture systems such as non-scaffold, anchorage-independent and scaffold-based systems as well as hybrid 3D culture models wherein cells form spheroids and are later incorporated into a 3D polymeric scaffold (Ho *et al.*, 2010). These models are chosen according to the nature of an experiment. For the purpose of this project, an organotypic-raft culture model was adapted for development of normal and CRC tumour models. Our current objective is to develop 3D cell culture for CRC and normal colon epithelium to enable us to better understand the internalisation efficiency of gold nanoparticles interacting with cells arranged in 3D.

4.3 Types of 3D culture models

Different models are envisaged for replicating *in vivo* characteristics and features of the cancer. Amongst them, cell-seeding scaffold based 3D models, hydrogel embedding, microfluidics chips and cell patterning devices are common (Langhans, 2018) (Figure 37). Therefore, these model systems are employed keeping one's needs and interest in mind. The latest addition to the 3D culture systems offer microscale 3D culture with automated high throughput screening for identifying the best drug candidate for cancer (Langhans, 2018).

4.3.1 Anchorage-independent 3D cell culture

An anchorage-independent system is based on the cell's self-aggregation capability in specialised culture plates such as hanging-drop microplates, low adhesion plates, with an ultra-low coating which promotes spheroid formation, and micropatterned plates that offer microfluidic cell culture. In general, spheroid effectively replicates physiological features of the tumours *in vivo* including cell-to-cell interactions and cell-to-ECM, if ECM is utilised in the culture (Mueller-Klieser, 1987) and (Sutherland, 1988). A number of cells seeded can determine the size of the spheroid formation and can grow large enough to have its own oxygen and nutrient gradient in the 3D cell culture like a tumour *in vivo* (Ekert *et al.*, 2014). However,

the disadvantage of the spheroid is to obtain reproducibility and not to reach a size too large to prevent oxygen and nutrients to its core (Langhans, 2018).

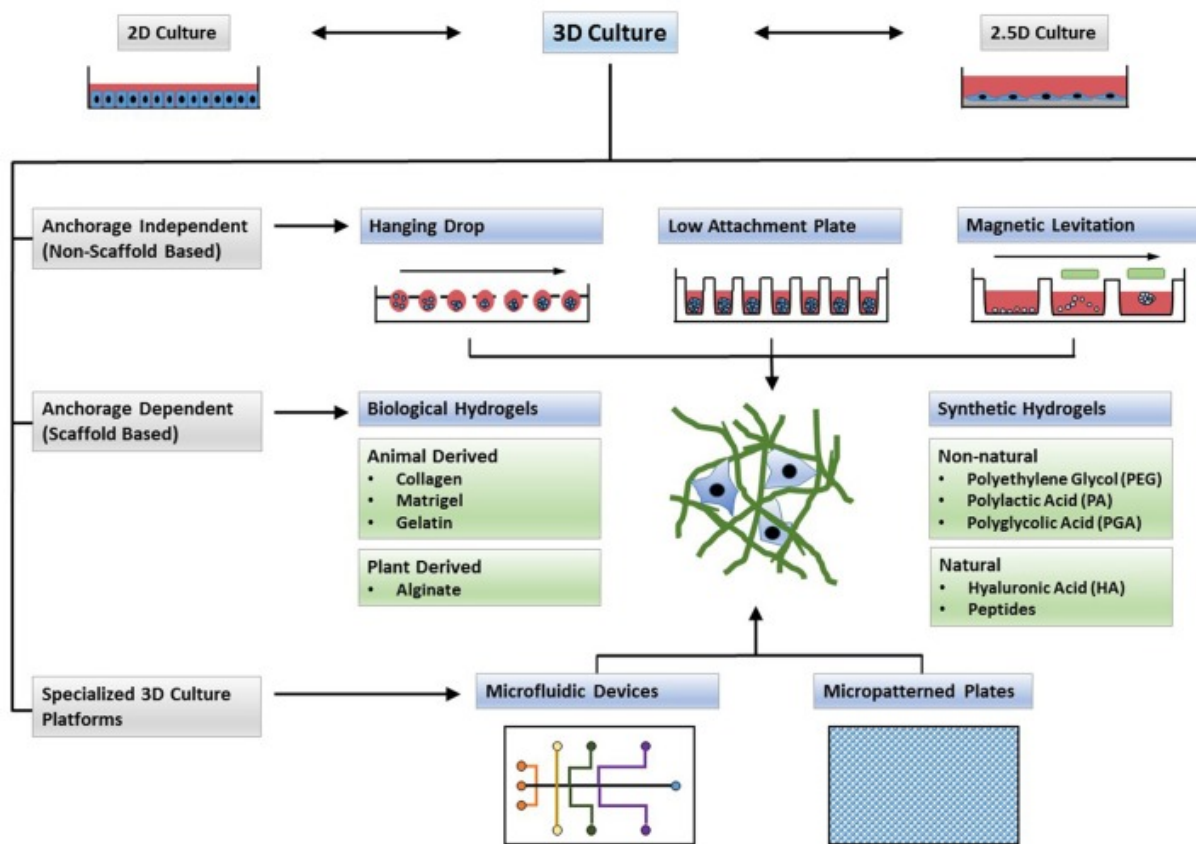


Figure 37: Figure shows the types of 3D cell cultures systems. Unlike 2D monolayer and 2.5D cell culture system, wherein cells are grown and cultured on top of thick layer of ECM, 3D models exhibits complex structures. Cells can be grown in spheroids (anchorage independent system) or seeded on the prefabricated 3D scaffolds (anchorage dependent). Moreover, spheroids in ECM scaffolds, microfluidics devices and micropatterned plates can together form a hybrid cell culture system that can offer advantages of both the systems to form a complex microenvironment for 3D cell culture (Langhans, 2018).

4.3.1a Hanging drop model and Ultra low attachment (ULA) plates

As mentioned above, the hanging drop model form spheroids by self-aggregation of the cells in the culture plates, when a surface is unavailable for cell attachment (Figure 38). This model is created in a specialised plate with open, bottom-less wells that promote the development of small media droplets. This droplet is large enough for the formation of the spheroid but small enough for its easy manipulation preventing it from being dislodged. Once cultured for several days, it exhibits three layers of the cells, the outermost being the

proliferating layer of cells, the middle is quiescent cells and innermost being the necrotic core. Such formation of layers allows oxygen and nutrients to diffuse inwards while draining the waste out of the spheroid core along with low pH. Therefore, it mimics an *in vivo* like tumour gradient. Later, the spheroid is transferred to another plate which has higher medium volume to preserve and maintain adequate nutrient supply and pH over a longer duration and can even form bigger spheres (Langhans, 2018).

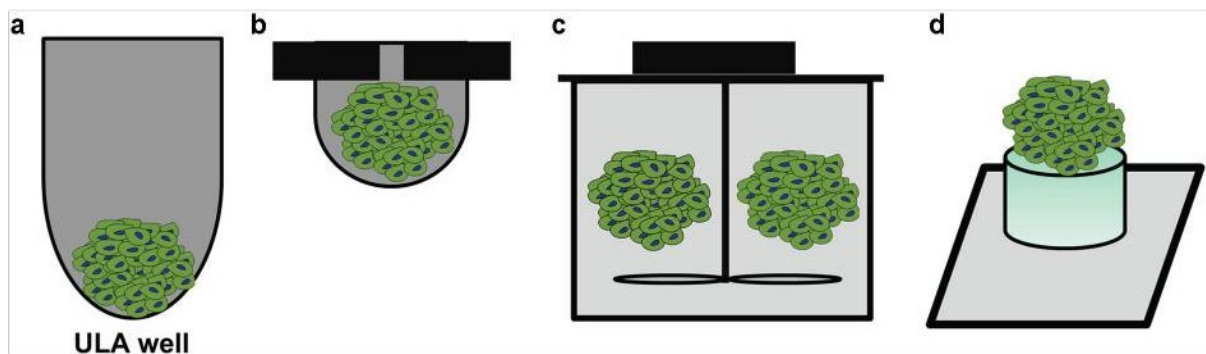


Figure 38: Four different techniques of developing spheroids are shown a) ultra-low adhesion (ULA) coated plates with a round bottom wells b) suspension of a droplet in a hanging drop model wherein the cells are self-aggregated and form spheroids c) Culture suspended in a bioreactor wherein the cells are self-aggregated forming spheroids and d) a random pillar in micropatterned plates where the cells are grown on the top of the pillar to form spheroids (Fang and Eglen, 2017).

ULA plates (Figure 38) are used similarly, the only difference is that the cells are grown in the round, tapered or V-shaped bottoms to exploit the lack of surfaces for cells attachment which encourages self-aggregation necessary for spheroid formation. Another difference is, unlike in the hanging drop model where the spheroid is transferred to another non-attachment plate, the spheroid in ultra-low attachment coated plates is not transferred, as 96- and 384-wells are large enough to contain more medium, maintain low pH and accumulate waste for a longer a period of time. These plates are mostly made up of polystyrene and have to be treated with hydrophilic or hydrophobic coatings prior to their use (Li *et al.*, 2011).

4.3.1b Magnetic levitation

The magnetic levitation technique relies on the formation of spheroids using magnetic nanoparticles. Magnetic nanoparticles are incubated with cells, and the magnetic field is

applied externally. Due to the externally applied magnetic field, these cells are now floating on the surface of the media, at the air-to-surface interface to promote cell-to-cell aggregation and spheroid formation. Magnetic levitation had been used to form spheroids using cells from various tissues to form multicellular mesenchymal stem cells spheroids and in tissue engineering (Lewis *et al.*, 2016) and (Lewis *et al.*, 2017).

4.3.2 Anchorage-dependent 3D cell cultures

Anchorage-dependent 3D cell culture systems rely on the provision of mechanical structures or matrices made up of ECM to promote cell-to-cell self-aggregation, proliferation and migration. As shown in Figure 37, 2.5D culture based technology requires the cells to grow on ECM proteins superficially, which then allows tissue differentiation, pertaining to a specific cell type, to take place (Langhans, 2018). The Scaffold used in this type of 3D culture system is made up of a variety of materials including polystyrene or can be from biological origin to replicate firmness, charge or other adhesive structures. Additionally, growth factors, hormones and other biological molecules can be used to achieve increased growth and proliferation rate and to mimic a specific cell phenotype (Langhans, 2018).

4.3.2a Hydrogel

In vitro hydrogel is the network of polymeric chains with given sets of structure and properties. It is created by intermolecular crosslinks using an artificial polymer or by interfibrillar crosslinks using a supramolecular fibrillary hydrogel network (Worthington, Pochan and Langhans, 2015) and (Yan and Pochan, 2010). Hydrogels are made either from natural sources such as collagen, fibrin or Matrigel or from artificial sources such as polyethylene glycol (PEG), polylactic acid and polyglycolic acid. Different types of hydrogels can be mixed to produce a hybrid with desired traits and features. Hydrogels created from natural sources have natural adhesive properties and can retain cell viability, controlled proliferation and differentiation found *in vivo*. Amongst all natural sources, collagen I is the most abundantly used ECM protein in hydrogels (Orgel, Persikov and Antipova, 2014). With

different collagen I concentration, and due to its biocompatibility, a varying degree of stiffness in the hydrogel can be produced for controlled cell proliferation (Doyle *et al.*, 2015). Collagen and Matrigel both induce cell attachment via integrin receptors and can also activate cell-signalling pathways for cell proliferation, growth and differentiation (Kutschka *et al.*, 2006). This, in turn, also help to stimulate appropriate responses to chemotherapy, radiotherapy and immunotherapy (Dickreuter and Cordes, 2017). The advantages of this system is low antigenicity whereas limitations include poor mechanical properties and low stiffness restrictions (Kutschka *et al.*, 2006).

4.3.2b Microfluidic devices and micropatterned surfaces

Imprinting wide arrays of microscopic patterns onto the surface of the plates, with low adhesion coating, allows for better cell-to-cell adhesion and scaffold-free growth of microspheroids within the microspace (Figure 38). In contrast, scaffold-based polymeric micropatterned devices such as porous discs, electrospun scaffolds or orthogonally layered polymers are also available that provide physical support for cell attachment and migration. These scaffolds can be an inert matrix or designed to mimic ECM found *in vivo* (Knight *et al.*, 2011). The most common use of such scaffold-based technology is for tissue regeneration to create the right physical and structural environment of bone, ligaments and cartilage and for skin, vascular, skeletal muscle or central nervous system tissue (Weeber *et al.*, 2017). This system of microfluidic devices allows for *in situ* visualisation of the tumour or spheroids using existing microplate readers (Hsiao *et al.*, 2009). These models significantly allow monitoring of the growth of 3D models in real time with low volumes of media (Dimov *et al.*, 2011).

4.3.2c Organotypic epithelial rafts

Organotypic cultures are a subtype of 3D culture system that is adapted to mimic *in vivo* structure and function of the tissue. Organotypic culture systems are used to study the differentiation of the cells and cell-cell interactions within the same tissue. Raft based organotypic culture, a subclass of 3D organoid culture, helps reconstruction of epithelial tissue

consisting of avascular epithelium that is attached via a basement membrane to supporting connective tissue stroma (Robichaux Viehovever *et al.*, 2004). The development of organotypic epithelial raft cultures has provided researchers with an efficient *in vitro* system that faithfully recapitulates epithelial differentiation (Anacker and Moody, 2012).

In an attempt to construct epithelial rafts, briefly Ozburn and Patterson, 2014, mixed human fibroblasts cells with type I collagen to form a gelatinous lattice which acted as a scaffold for human keratinocytes to grow and differentiate. The matrix was then propped onto a wire mesh in the 6-well plate to achieve an air-to-liquid interface. Keratinocytes have grown and stratified upon the gelatinous lattice over a 3-week period. Such epithelial rafts were used to study the effect of α -herpesviruses herpes simplex virus type 1 (HSV-1) and type 2 (HSC-2) and varicella-zoster virus (VZV) as they particularly target keratinocytes in the skin (Andrei *et al.*, 2005). Three-dimensional organotypic epithelial rafts of keratinocytes also helped capture the entire life cycle of Human Papilloma Virus (HPV) and is considered a stepping stone in 3D cell culture modelling (Davy *et al.*, 2005). A similar approach has been used in the present project to recreate normal and CRC *in vitro* 3D models. Dead de-epidermalised dermis (DDED) was used as a scaffold for the 3D models. Upon DDED the epithelial cells of CRL1790, CRL2159 and HCT116 were incubated and grown over a period of 4 weeks providing a platform that allows diffusion of the nutrients from the growth media below to the cells on the apical surface (Figure 39). Newly developed CRC and normal 3D models using organotypic raft culture system were the first to demonstrate 3D cells arrangements of CRC. Additionally, application of GNPs in these 3D cultured models of CRC will also be the first to demonstrate the uptake of GNPs in the cells.

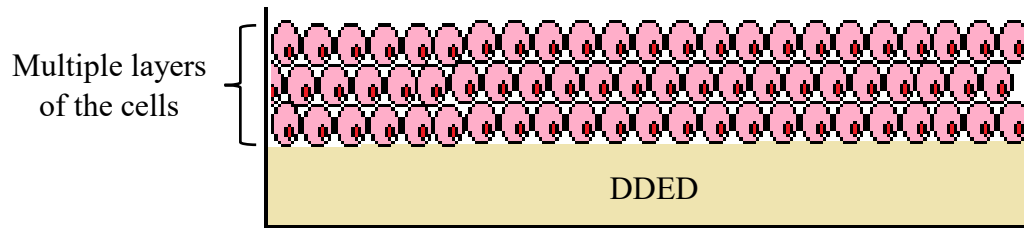


Figure 39: Schematic representation of 3D models developed. DDED of the skin is used as a scaffold to grow and culture multiple layers of cells on top.

4.4 Extracellular matrix in CRC

The role of the extracellular matrix (ECM) has been recently revealed in the tumorigenesis of CRC (Lu, Weaver and Werb, 2012). For successful migration and invasion, CRC epithelial cells must degrade ECM components. ECM, with its distinctive biochemical and biomechanical properties, is one of the vital features in normal colon physiology and maintains a niche between proliferation, cell adhesion, migration, differentiation, apoptosis and in regulating overall cell behaviour (Figure 40) (Radtke and Clevers, 2005). ECM proteins conform isotropic arrangements of various proteins and functions to maintain homeostasis and to regulate tissue repair in case of injury and damage (Crotti *et al.*, 2017). In CRC, anisotropic and disorganised arrangements of ECM leads to CRC progression, malignant transformation of the cells and metastasis (Figure 40). This arrangement of ECM proteins and components in CRC are the hallmark of a pathological microenvironment (Goetz *et al.*, 2011). Normal colon epithelial (columnar and cuboidal) cells act as a physical barrier and help in absorptive and exocrine functions. These epithelial cells are polarised which can be recognised via their apical pole, consisting of two lateral surfaces and imparting inter-cellular connectivity and a basal surface attached to the basement membrane (BM). BM, another form of ECM, separates colonic mucosa from submucosa (Crotti *et al.*, 2017). The main component of BM is collagen IV along with other proteins such as proteoglycan, glycoproteins, laminin, fibronectin and nidogen (Worthley, Giraud and Wang, 2010). However, collagen IV is replaced by collagen I

in the lamina propria which lacks disulphide bridges giving less rigidity and more elasticity to ECM compared to BM (Tlsty and Hein, 2001). Along with structural proteins, ECM also comprises secretome, a group of proteins and molecules secreted by the CRC tumour. These proteins are secreted by the cleavage of the signal peptide in the tumour cells as well as through exosomes (Mathias *et al.*, 2012).

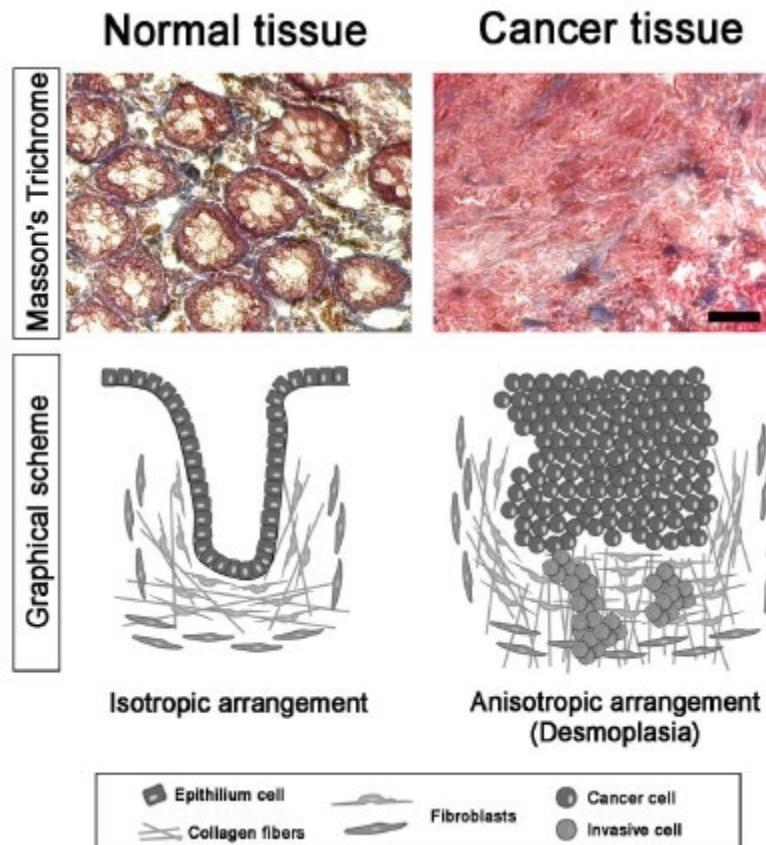


Figure 40: Schematic representation of the normal colon and CRC tissue. Top panels: Masson's trichrome staining showing the connective tissue (blue), nuclei (red/purple), and cytoplasm (red/pink). Lower panel: Graphical scheme showing the transition of the normal colon (isotropic) mucosa to cancer (anisotropic) microenvironment (Crotti *et al.*, 2017).

Like any tumour, CRC has three basic features: 1) the parenchyma which contains both proliferative neoplastic cells and supporting stroma 2) tumour associated cells (activated macrophages and fibroblasts) and 3) blood vessels (Crotti *et al.*, 2017). Due to excess collagen fibres being deposited around parenchymal cells following BM degradation in CRC, the term desmoplasia is also used to characterise such arrangement. Degradation of BM paves the way for tumour progression via the release of angiogenic, growth-stimulating and

chemotactic factors that were embedded in BM (Tlsty and Coussens, 2006). Laminin-332 (also known as laminin-5) degradation in the BM of the normal colon activates EGFR receptor pathway leading to reduced cell-matrix adhesion and migration (Guess *et al.*, 2009). Loss of BM is one of the most common markers to study in CRC invasion and metastasis leading to poor survival rate in patients without BM (Mylonas and Lazaris, 2014). Besides the above mentioned changes, alterations in elasticity also play a crucial role in CRC pathogenesis. ECM possesses collagen I type fibres that do not form disulphide cross-links and, as such, contribute to tissue elasticity. However, due to upregulation of lysyl oxidases, it modifies the ECM by cross-linking proteins and increases the stiffness in ECM by forming these disulphide bridges. The change from softness to the rigidity of the matrix is thus an important factor in CRC (Baker *et al.*, 2011) and (Baker *et al.*, 2013). Thus, ECM plays a vital role in CRC and a valid normal vs CRC *in vitro* 3D models can be developed.

4.5 Cytokeratins

The cytoplasm of the eukaryotic cell is made up of a cytoskeleton that affects the structure and functions of the cell. This cytoskeleton consists of three different filaments, Intermediate Filaments (IFs), microtubules and microfilaments (Fuchs and Cleveland, 1998). IFs are further categorised into five different subtypes based on their amino acid sequences and structure of the protein (Kim and Coulombe, 2007). Cytokeratin (CK), also known as keratin, constitutes the largest subtype of IFs and is preferentially expressed in the epithelial cells (Omary *et al.*, 2009). They are classified into two types, type I (acidic) and type II (basic) keratins. Type I keratins includes 28 keratins; CK9-10, CK12-20 and CK23-24 are epithelial keratins, CK25-28 are hair follicle epithelial keratins, and CK31-40 (including CK33a and CK33b) are hair keratins. Type II includes 25 keratins; CK1-8 (including CK6a, CK6b and CK6c) and CK76-80 (epithelial keratins), CK71-75 are for epithelial hair follicles and CK81-86 are hair follicle keratins (Pastuszak *et al.*, 2015). Keratins confer mechanical support to the

tissue and its differential expression leads to various pathophysiological phenotypes including cancer (Coulombe *et al.*, 1991). Keratin forms by heterodimerisation of type I and type II CK, by the interaction of coiled-coil domains in the protein pairs, generating coiled structures with free globular domains at the amino (N)- and carboxyl (C)-termini (Omary *et al.*, 2009). For example CK5 and 14 is preferentially expressed in epidermal basal keratinocytes, whereas suprabasal keratinocytes express CK1/10 (Omary *et al.*, 2009). In simple normal epithelium (single layered epithelia), CK7, CK8, CK18, CK19, and CK20 are predominantly expressed and, thus, are classified as simple epithelial keratins (Chu and Weiss, 2002). Simple epithelia are found around the glands and organs involved in secretion and absorption including colon and small intestine (Oriolo *et al.*, 2007).

4.5.1 Cytokeratins 7 and 20 in CRC

In CRC, having a reliable tool to determine a diagnosis is indispensable as CRC largely remain asymptomatic, and when diagnosed, the survival rate is <5%. Cytokeratins or keratins, hence, can play a crucial role in determining the diagnosis of the patient, and cytokeratin profiles can be created for different malignant tissues from different epithelial origin (Chu and Weiss, 2002). Tissue-specific distribution of CK from normal tissue is highly preserved in various neoplasms and not amenable to degradation due to malignant transformation (Bayrak, Yenidünya and Haltas, 2011). This CK pattern remains the same in primary and their metastatic sites in all carcinomas and is independent of its location and size (Moll *et al.*, 1982). Therefore, antibodies against specific cytokeratin can identify different types of carcinomas to its origin that cannot otherwise be easily distinguished (Jasik, 2012). Relative expression of two such simple epithelial keratins, CK20 and CK7, has thus been implicated in CRC adenocarcinoma, and is used as a diagnostic marker to identify CRC from other epithelial malignancies (Espinosa De Los Monteros *et al.*, 1999). CK7 is a polypeptide of molecular weight 54 kDa and isoelectric point 6. In normal tissue, this basic type II CK have been shown to be expressed in wide arrays of simple epithelia of breast, lung, mesothelium, female genital tract and urinary

bladder. CK7's detection is limited in the gastrointestinal tract of normal epithelium. On the other hand, CK20 has molecular weight 48.5 kDa and isoelectric point 5.66 (Jasik, 2012). Acidic type I CK20 has the most restricted expression pattern. It is only found in goblet cells of gastrointestinal tract, urothelium, Merkel cells in the epidermis and outer sheath of the hair root (Moll *et al.*, 1992). As per the immunohistochemical staining of the normal colon epithelia, CK7 focal expression patterns were visualised on the surface and crypt, due to its limited expression in the gastrointestinal tract, whereas CK20 was found to be diffusive on the surface of the normal colon epithelium and decreases towards the crypt (Bayrak, Yenidünya and Haltas, 2011).

Table 10: Relative expression of CK7 and CK20 in colorectal cancer is shown in the table below. Adapted from (Chu, Wu and Weiss, 2000).

CK20	CK7(+)	CK7(-)
CK20(+)	Normal colon epithelium	Colorectal Cancer
CK20(-)	Stomach and Pancreatic cancer	Oesophagus – Squamous cell carcinoma

By contrast, primary CRC adenocarcinoma has been shown to harbour relative keratin expression profile of CK20+/CK7- . It also help distinguish CRC from other epithelial origin such as breast, lung and liver because CK7 expression in CRC is very rare and can be utilised to rule out CRC from other cancers (Park *et al.*, 2007). CK7 is an intermediate filament that is not found in squamous epithelium whereas CK20 is found in gastric and colon adenocarcinomas (Gheini and Jalayer Naderi, 2017). A project that investigated 435 cancers found that CK7 was expressed in almost all cancers except for colon, prostate gland, kidney and thyroid cancers. On the other hand, CK20 expression was found in all CRC samples and none observed in other cancers (Table 10) (Chu, Wu and Weiss, 2000). In an another study conducted between 2008 and 2014 of the patients suffering from CRC, the expression of keratin CK20+/CK7- was also found to be aligning with other literature making (CK7-) and (CK20+)

a good diagnostic marker for CRC (Gheini and Jalayer Naderi, 2017). Similarly, the relative expression of CK20+/CK7- was also found in a study that undertook 196 patients suffering from CRC. In that, CK7 was hardly observed (17%), whereas CK20 was found in 159 (81.1%) of the total 196 CRC cases (Bayrak, Yenidünya and Haltas, 2011). Thus, to validate the 3D *in vitro* models, relative expression of CK7 and CK20 was used to demonstrate the feasibility of the models. To validate 3D normal models, positive expression of CK7 and CK20 was used (CK20+/CK7+). For CRC 3D *in vitro* models, absence of CK7 and positive expression of CK20 on the surface (CK20+/CK7-) was utilised.

4.6 Methods and Materials

4.6.1 Cell lines and cell culture

All three cell lines human colon epithelium (CRL1790), Duke's B colorectal carcinoma (CRL2159) and CRC carcinoma (HCT116) were grown and cultured as described previously in chapter 2 using appropriate culture media. Each cell line was trypsinised and passaged for increasing the cell density needed for subsequent 3D cell culture. Using a haemocytometer, approximately 1×10^6 cells were counted for the use in 3D cell culture application (see below).

4.6.2 3D cell culture scaffold preparation

In 3D cell culture, DDED was used as a scaffold to seed CRL1790, CRL2159 and HCT116 cells for growth and proliferation. Initially, the piece of the DDED was kept in the solution of 1X phosphate buffer saline (PBS) for 2 days supplemented with 500 μ l of antifungal solution (Antibiotic and Antimycotic) (Gibco® 15240-062) to prevent any fungal growth. After two days, the DDED scaffold in PBS was shaken well so that the epidermis had slowly started to peel off. A new solution of PBS was then added to the centrifuge tube containing the scaffold along with fresh 500 μ l of the antifungal solution. The steps were repeated until the DDED scaffold was left with almost no epidermis and the layer of dermis was visible. Lastly, the scaffold, with almost no epidermis, was taken out and placed on a sterilised plate and, using a scalpel, the rest of epidermis was removed. The DDED was then cut into small square pieces ($\sim 1\text{cm}^2$) and kept in the relevant solution of complete medium, according to the cell type requirement, until its further use.

4.6.3 3D cell culture seeding

Individually, cells from each of the cell lines, CRL1790, CRL2159 and HCT116, were grown and cultured as mentioned in Chapter 2. Once the flasks were confluent to 80%-90%, cells were extracted and counted using the haemocytometer. DDED was then placed in a 6-well plate and a sterilised metal ring was placed on top to fix its position in the well (Figure 41). Later, approximately 1×10^6 cells in 100 μ l were seeded onto the scaffold, inside the metal

ring, for each cell line. A 6-well plate was then placed in the incubator at 37°C and 5% CO₂ for 4 hours for optimum attachment of the cells to the dermis. Later, complete medium, as required for each different cell type, was aliquoted in the centre of the ring for cell nourishment, binding and growth overnight. Next day, the metal ring was removed using a sterilised forceps and the well was flooded with 2ml of relevant media. The DDED scaffold harbouring the cells was later incubated over the period of 4-5 weeks with media changing at every 2-3 days interval.

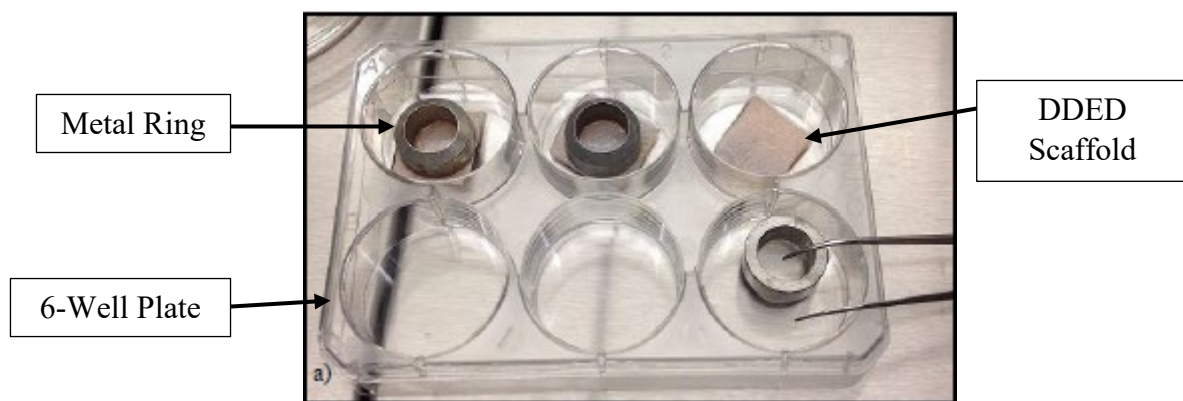


Figure 41: Figure shows an example of the 3D cell culture of the normal (CRL1790) and CRC (CRL2159 and HCT116) colon epithelium. Metal rings were placed on the top of the scaffold to affix the DDED in the well. 1×10^6 in 100 μ l were then seeded inside the ring and left in the incubator for optimum cell attachment to the dermis.

4.6.4 Histology

After the incubation for 3-4 weeks, the models or DDED were washed three times with 1X PBS and fixed using 4% paraformaldehyde for 24 hours. After fixation, the DDED were dehydrated using 70%, 80%, 90% alcohol sequentially for 1 hour and absolute 100% alcohol for 2 hours. Models were then treated with 100% xylene for 2 hours, and then 50%:50% (xylene: wax), 25%:75% (xylene: wax) for 1 hour each and ended with 100% wax for 2 hours. DDED, for every model, was then embedded in tissue cassette in the right orientation and left overnight on the freezing plate followed by tissue sectioning of 7 μ m thickness with a microtome using a water bath at 37°C. Samples were fixed on the slides for hematoxylin and eosin (H&E) staining and other immunohistochemistry (IHC) experiments.

4.6.5 Hematoxylin and Eosin (H&E) staining

Slides containing tissue sections were deparaffinised in 2 changes of 100% xylene for 5 minutes each. Models were then rehydrated in 2 changes of absolute alcohol, 90% and 70% for 3 minutes. Later, the samples were incubated in water for a few seconds and stained in Gill's hematoxylin solution for 10 minutes followed by briefly washing in water and differentiating in 1% Acid alcohol solution for a few seconds. Slides were again briefly washed in water and counterstained with eosin for 30 seconds. Sections were then exposed to 70%, 90%, and 2 changes of 100% ethanol for 3 minutes and 2 changes of 100% xylene for 5 minutes. Finally, cover-slips were mounted using xylene-based mounting medium (DPX mounting medium Lot no. =1400611). Images were captured using Image-Pro 6.3 programme.

4.6.6 Characterisation of 3D models by Immunochemical staining

Paraffin embedded tissue section on slides were deparaffinised by immersing in 2 changes of 100% xylene for 5 minutes followed by 2 changes of absolute alcohol and 90% and 70% ethanol for 3 minutes each. To block endogenous peroxidase action, sections were exposed to hydrogen peroxide (H₂O₂) for 10 minutes. This was followed by washing with water and 1X PBS for 5 minutes each. In order to retrieve the antigen's epitopes, boiled 1X sodium citrate buffer at pH 6 or 0.1% Triton-100 in 1X PBS was aliquoted on the tissue sections as per requirement and incubated for 10 minutes. Again, the step was followed by washing with water and 1X PBS for 5 minutes each. 50% horse serum in 1X PBS (1:1) was then used to block unwanted and nonspecific binding of the primary antibody for 10 minutes. Primary monoclonal mouse antibodies for CK7 (1:500) (product no. ab9021) and rabbit monoclonal antibodies for CK20 (1:100) (product no. ab219589) were used to detect CK7 and CK20 expression in order to characterise and validate normal and CRC 3D models. Respective CK7 and CK20 primary antibodies were incubated with the tissue sections. Only CK7 primary antibody was reacted overnight at 4°C whereas CK20 was reacted only for 90 minutes as per manufacture's protocol. Later, using a VECTASTAIN ABC kit, the biotinylated-secondary antibody was incubated

with the sections for 30 minutes and rinsed with 1X PBS twice for 5 minutes each. Next, tertiary antibody conjugated with avidin was reacted for 20 minutes at room temperature. Sections were rinsed again with 1X PBS twice for 5 minutes each. 3,3'-Diaminobenzidine (DAB) substrate was used to develop the sections by incubation for 10 minutes. The sample was then briefly run through Gill's hematoxylin and eosin solution as mentioned before and washed briefly with water. Slides then were processed through 90% and 70% alcohol and 2 changes of absolute alcohol for 3 minutes, respectively. Next, the samples were incubated with 2 changes of xylene 5 minutes each and mounted with xylene based mounting media (DPX mounting medium Lot no. =1400611). Images were captured using Image-Pro 6.3 programme.

4.7 Results

The main aim behind developing normal and CRC cancer 3D models was to test the internalisation efficacy of GNPs in a near-similar *in vivo* environment. *In vitro*, human colon epithelium 3D model and two CRC 3D models were tested for the presence of CK7 and CK20 markers. To achieve this, first, H&E staining was carried out to visualise the 3D arrangements of cells from each type of 3D models. Secondly, validation of 3D models was done by demonstrating the relative pattern of keratin CK20 and CK7. In CRC 3D models, the relative pattern of CK20+/CK7- was observed, whereas a CK20+/CK7+ pattern was identified in the normal 3D model using 3,3'-diaminobenzidine (DAB) IHC staining.

4.7.1 Hematoxylin and Eosin staining

H&E staining was done on 7µm tissue sections from each type of 3D model, on the tissue containing slides. H&E staining has been in used for at least a century to characterise various components and morphological changes in the cells. Using H&E, cytoplasm, nucleus and extracellular characteristics can be visualised in cancer diagnosis. Hematoxylin develops a deep blue colour and stains the nucleic acid whereas eosin stains proteins non-specifically and is pink in colour. In normal fixed tissue, nuclei stain blue and cytoplasm in varying degree of pink depending upon the components can be seen. This helps to identify the histology between the normal and cancerous tissue (Fischer *et al.*, 2008).

4.7.1a Normal colon epithelium model (CRL1790)

Characterisation of the normal 3D model made from CRL1790 is essential to establish a control to compare the results with. Here, H&E staining for the normal colon 3D model is shown in Figure 42. Cells have formed multilayers as observed *in vivo* and in some areas are tightly arranged to mimic the tissue histology.

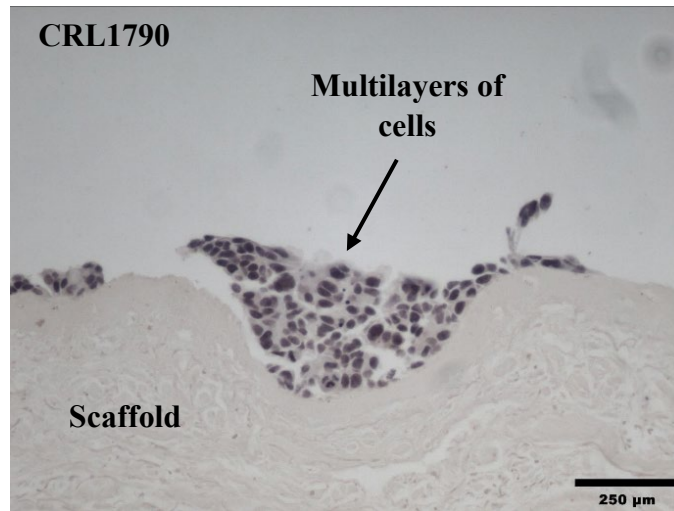


Figure 42:- Figure shows H&E staining of CRL1790 normal 3D model at 20X magnification. Cells have formed multilayers upon the scaffold as seen *in vivo* environment. Scale bar = 250μm.

4.7.1b CRC 3D model (CRL2159 AND HCT116)

3D CRC models cultured from CRL2159 Duke's B colorectal carcinoma and HCT116 CRC carcinoma stages are shown in Figure 43. Cells on DDED have formed a significant 3D arrangement of cells as different monolayers are laid on top of each other. ECM of DDED worked as a matrix to support the 3D cell arrangements. CRL2159 and HCT116 shows a good potential in creating CRC *in vitro* 3D models.

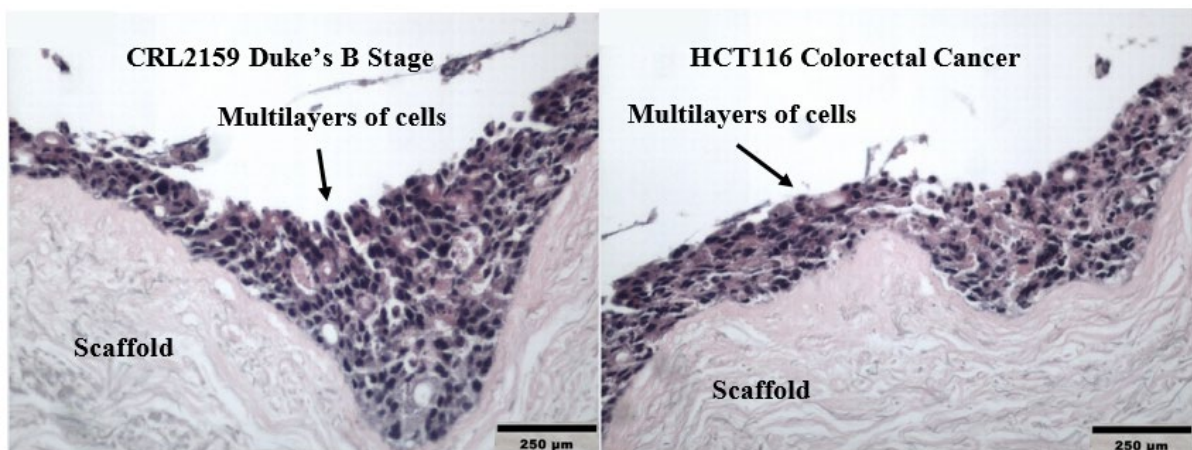


Figure 43: Figure shows H&E staining of CRL2159 (left) and HCT116 (right) 3D models at 20X magnification. Cells have formed multilayers upon the scaffold as seen *in vivo* environment. Scale bar = 250μm.

4.7.2 Characterisation of 3D cell models using Immunohistochemistry

To verify the potential of normal and CRC in vitro 3D cell models, relative expression patterns of keratins CK7 and CK20 were utilised. In CRC, the expression of keratin CK7 was absent (Figure 44) and (Figure 45). On the other hand, the expression of keratin CK20 was positive and diffuse (Figure 47) and (Figure 48). Therefore, the expression pattern of CK20+/CK7- was observed in both CRC 3D in vitro models. Moreover, in the normal colon 3D model, limited and intermittent expression patterns of CK7+ have been seen, whereas CK20 was found in mostly all cells. Therefore, the expression pattern CK20+/CK7+ was used to characterise normal colon 3D model (Figure 43) and (Figure 46).

4.7.2a CK7 expression in normal colon epithelium 3D model (CRL1790)

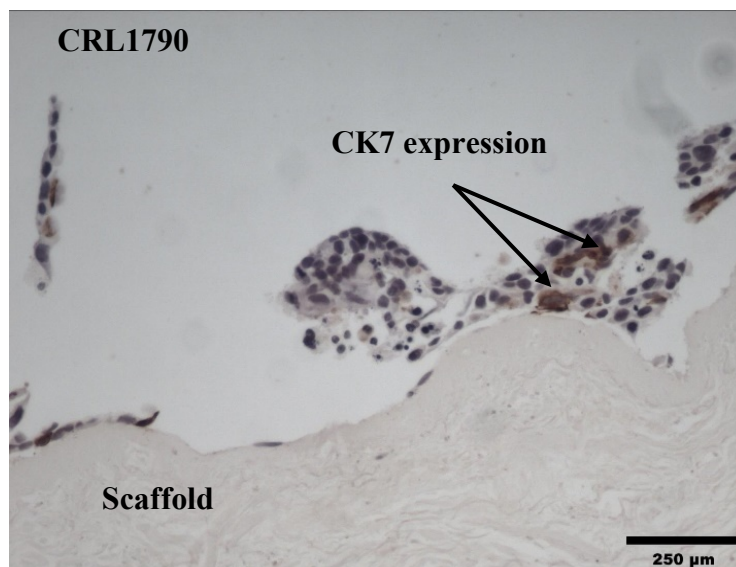


Figure 44:- Focal expression of CK7 is shown in the normal 3D model. CK7 is expressed in the normal colon epithelium cells at 20X Magnification. Scale bar = 250μm.

4.7.2b CK7 expression in CRC 3D models (CRL2159 and HCT116)

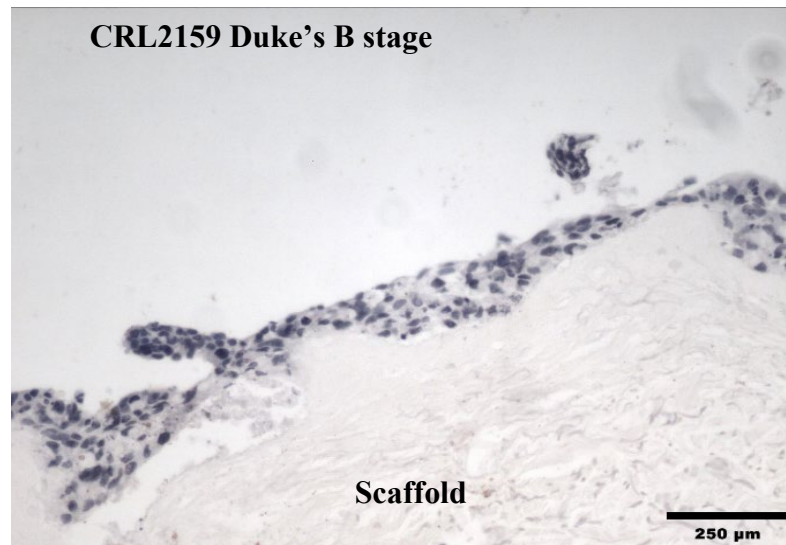


Figure 45: CK7 expression pattern was absent in CRL2159 Duke's B 3D model. No DAB staining in the regions has been found. The image is shown at 20X magnification. Scale bar = 250 μ m.

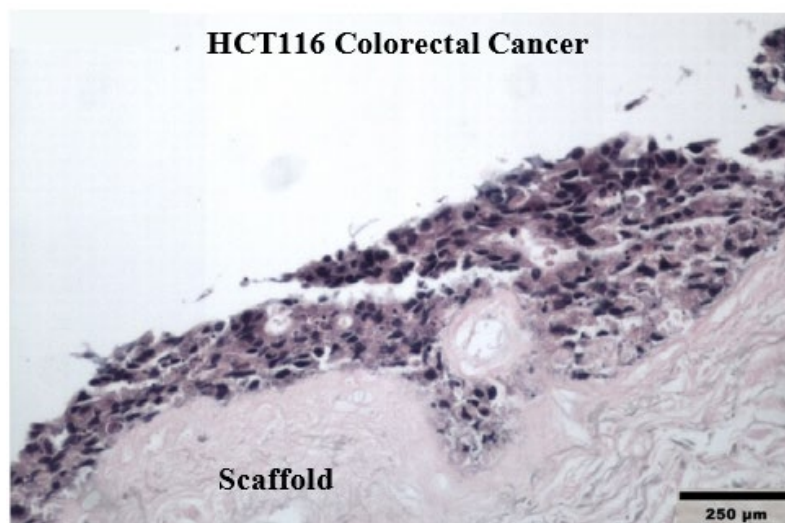


Figure 46: CK7 expression pattern was absent in the HCT116 Colorectal Carcinoma 3D model. No DAB staining in the regions has been found. The image is shown at 20X magnification. Scale bar = 250 μ m.

4.7.2c CK20 expression in normal colon epithelium (CRL1790)

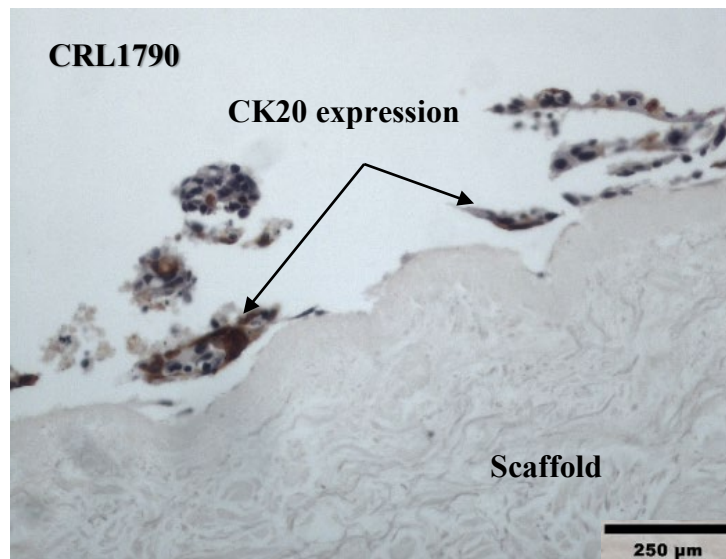


Figure 47:- CK20 expression is positive and at higher level in the normal 3D model compared to CK7. Image is shown at 20X magnification. Scale bar = 250μm.

4.7.2d CK20 expression in CRC 3D models (CRL2159 and HCT116)

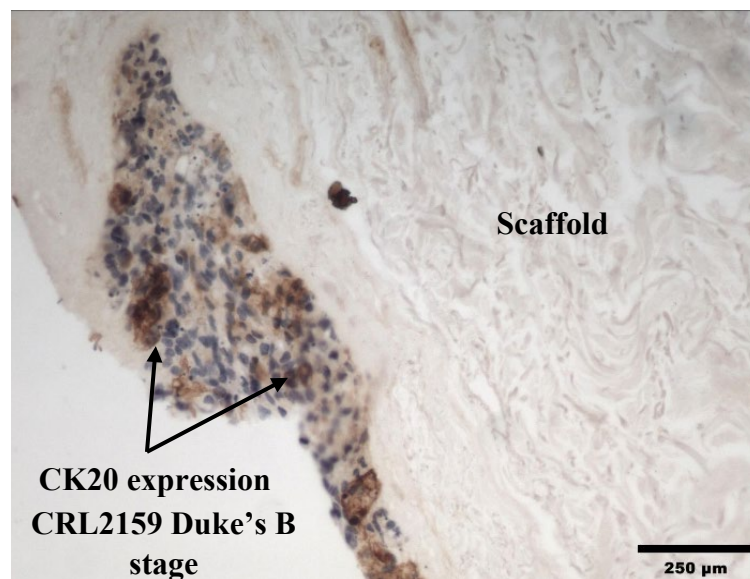


Figure 48: Images shows the expression of CK20 in CRL2159 3D model at 20X magnification. A high level of DAB staining for CK20 is revealed in this model making it a potential 3D model for Colorectal Cancer. Scale bar = 250μm.

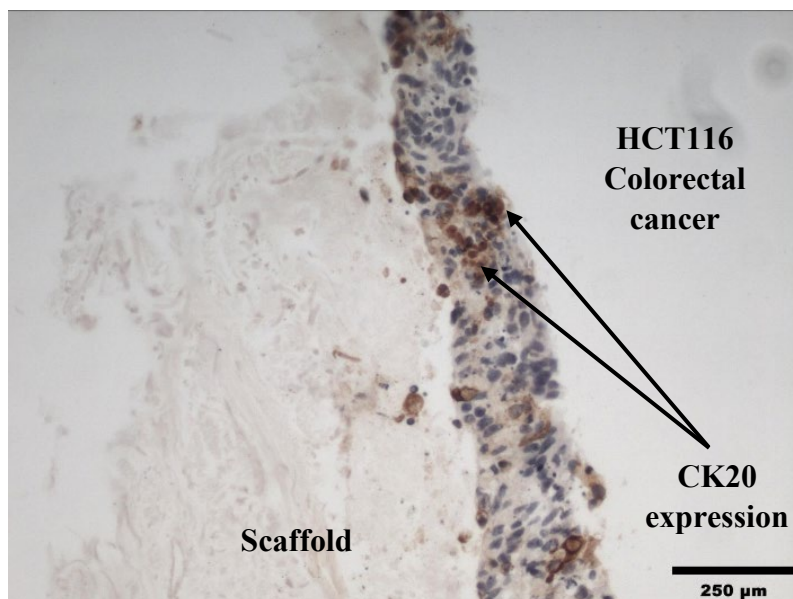


Figure 49: Images shows the expression of CK20 in HCT116 3D models at 20X magnification. High levels of DAB staining for CK20 is revealed in this model making it a potential 3D model for Colorectal Cancer. Scale bar = 250μm.

The presence of keratin markers is denoted as positive (+) and negative (-), if >5 cells are stained it is denoted by (+), >10 by (++) strong positive and >20 by (+++) for very strong positive signals for relevant keratin markers. The method of scoring was adapted from one of the study conducted that validated the expression of DAB staining from normal colon and CRC samples of 196 patients using CK7 and CK20 (Bayrak, Yenidünya and Haltas, 2011). For the purpose of counting the cells, 3 different field views were selected along the path of each 3D model with most number of cells. Also, intensity of the stain was not considered, instead only positive or negative expression of DAB staining was used to ascertain the expression of CK7 and CK20. The presence of these markers has shown a good potential of the 3D models to be used for testing GNP's efficacy.

Table 11: IHC staining for CK7 and CK20 is shown in the table below for each type of 3D *in vitro* models.

3D MODELS	CK7	CK20	Results in line with literature
CRL1790	+	++	(Bayrak, Haltas and Yenidunya, 2012)
CRL2159	-	+++	(Chu, Wu and Weiss, 2000)
HCT116	-	+++	(Gheini and Jalayer Naderi, 2017)

4.8 Discussion

3D cell culture has great advantages for the study of the effects of drugs and other chemicals because of the 3-dimensional arrangement of the cells *in vitro*. *In vivo*, cells are not only in contact with each other but also with the extracellular matrix. In contrast, cells cultured in 2D monolayers are flattened and all the cells are adjacently grown and in 100% contact with the drugs they are exposed to superficially (Kim, 2005). Thus, the results gathered from the cell arrangement in 2D monolayers are poorly translated into the clinical trials (Griffith and Swartz, 2006). As such, 3D *in vitro* models for normal colon epithelium, Duke's B stage and CRC carcinoma were envisaged to understand *in vivo*-like efficiency of GNPs. The model opted to culture these 3D models were organotypic-raft models where the cells were seeded on the top of the DDED scaffold and cultured for 3-4 weeks. Such a culture system is referred to as a organotypic raft culture system (Davy *et al.*, 2005). This allows one to faithfully recapitulate epithelial cell arrangement. Normally, organotypic rafts are created using mouse or human fibroblasts reconstituted with collagen type I to form a gelatinous scaffold, upon which the cells are seeded (Ozbun and Patterson, 2014). However, the scaffold used here was DDED. Cells were seeded superficially and cultured for 3-4 weeks after which they were organised in multilayers as found *in vivo*. This was a better alternative as it diminished the use of 2-3 types of cell lines and ECM components to recreate the scaffold.

Moreover, ECM components of the scaffold acted as an extracellular matrix for all type of normal and CRC 3D models. In a normal colon, the lamina propria contains various ECM proteins along with fibroblasts and recruited inflammatory cells (Levine and Haggitt, 1989). ECM in this region forms a 3-dimensional matrix or a network providing a scaffold of support to basement membrane (BM) and columnar epithelial cells above (Rowe and Weiss, 2009). The main constituent of the ECM is collagen type I glycoprotein (Berk *et al.*, 2008). Other ECM components contributing towards this 3-dimensional scaffold are heparin sulphate, proteoglycans and fibronectin (Hynes and Yamada, 1982). Similarly, 3-dimensional ECM of

the DDED scaffold plays a crucial role in supporting the epidermis above. Collagen is the predominant ECM protein in the dermis (Weinstein and Boucek, 1960) and Collagen I and III are considered to be the abundant interstitial collagens present in the ECM of the normal human dermis (Weber *et al.*, 1984) and (Watt and Fujiwara, 2011). Besides collagen I and III, other BM associated ECM molecules present are heparin sulphate, fibronectin and nidogen that renders additional support to the epidermis above (Uitto, Olsen and Fazio, 1989). Therefore, the similarities in ECM proteins in colon physiology and in the de-epidermalised dermis has helped faithfully to recapitulate the normal and CRC 3D *in vitro* models.

Hematoxylin and eosin staining of all the three models shows multiple monolayers of cells, in 3 dimensions, aligned horizontally which is similar to that of the tissue architecture found *in vivo* (Figure 42) and (Figure 43). Additionally, cells are also attached to the ECM of the scaffold as well as with other neighbouring cells mimicking the natural physiology of the tissue. This 3D arrangement of the cells, mimicking the normal and cancer pathophysiology of the tissue, will help in understanding the GNPs's internalisation efficacy in a near-similar environment. Moreover, to validate these models further, the analysis of cytokeratins were carried out. Cytokeratins are a subgroup of IFs that constitute the cytoskeleton structure of the cells. Upon differentiation, a specific type of cells expresses different subtype of keratins depending on the epithelial cell origin. Cytokeratin CK7 and CK20 are simple types of keratins in epithelial cells that were used to verify the potential of 3D normal and CRC *in vitro* models. In normal colon epithelia, the expression of CK7 is absence or limited, whereas CK20 is expressed throughout (Jasik, 2012) and (Bayrak, Yenidünya and Haltas, 2011). In an attempt to differentiate between the presence of CK7 and CK20 in normal colonic tissue and colon adenocarcinoma, the CK7 and CK20 expression pattern was studied in normal colon epithelia. It was observed that CK7 was found to be focal and on the surface and crypt of the normal colonic epithelium. On the other hand, CK20 was observed throughout but was less expressed

towards the crypts (Bayrak, Yenidünya and Haltas, 2011). Similar staining for CK7 and CK20 was observed in normal colon 3D model, wherein CK7 was expressed only in a few cells (Figure 44), whereas CK20 was most expressed (Figure 47). Therefore, it can be said conclusively that the model so developed using organotypic raft is a normal colon 3D *in vitro* model.

In contrast, the presence of CK7 in adenocarcinoma is found only in cells originating from breast, urinary bladder, female genital tract, lung and pancreatobiliary tract (Bayrak, Yenidünya and Haltas, 2011). CK20, on the other hand, is only found in CRC cell epithelium, urothelium and Merkel cell carcinoma (Bayrak, Yenidünya and Haltas, 2011). Hence, their combined expression pattern of CK20+ and CK7- had been used to investigate the diagnosis and prognosis of CRC. Studies that investigated numerous clinical CRC samples have observed differential arrangement of these keratins in malignant transformation of the normal epithelial cells, particularly in CRC tumours (Rullier *et al.*, 2000). As a result, specific patterns of CK20+/CK7- have been generated and observed in >95% of the patient sample in primary and metastatic CRC (Saad *et al.*, 2009). In a study, 64% (75 from 118) of the patient sample showed a similar expression pattern for CK20+ and CK7- in CRC (Saad *et al.*, 2009). Similar results have been obtained while characterising 3D *in vitro* CRC models. Both the models have demonstrated CK7- and a very strong positive signature (+++) for CK20 (Table 11). The CK20+/CK7- pattern had also been found in clinical samples and attributed to the CRC (Chu, Wu and Weiss, 2000) and (Gheini and Jalayer Naderi, 2017). Hence, through CK7 and CK20 staining, both CRC 3D *in vitro* models were validated. Lastly, 3D arrangement of cells and the collective expression pattern of CK20 and CK7 in respective models has helped validate the normal and CRC cancer 3D models *in vitro*.

4.9 Conclusions

To develop normal and cancer 3D *in vitro* models, three types of cell lines were used CRL1790, CRL2159 and HCT116. An organotypic raft model were used to successfully create each of the three 3D *in vitro* models. Cytokeratin markers CK7 and CK20 were utilised to validate 3D models. The relative expression of CK20 and CK7 was used to see the level of these keratins in each of the 3D models. In CRC, the expression of CK7 and CK20 has been implemented in diagnosis and prognosis. CK7 is rarely observed in CRC and CK20 is found in almost all CRC stages. Thus, in the CRC 3D models, the CK20+/CK7- expression pattern was found whilst CK20+/CK7+ was demonstrated in normal 3D model as found in the normal colonic epithelium. Furthermore, homogeneous multilayers of cells were also seen in these models that resembles that of *in vivo* tissue histology. Together with the cytokeratin expression and 3D arrangement of cells, normal and cancer 3D models were developed and validated. Next chapter will demonstrate the GNPs internalisation efficacy in 3D *in vitro* models and its subsequent comparison with 2D internalisation.

CHAPTER 5
Internalisation of GNPs
in 3D Normal and CRC
in vitro models

5.1 Aim

The aim of this chapter is to evaluate the uptake efficiency of GNPs-PEG, GNPs-PEG-FR- α , GNPs-PEG-Tyro3 and GNPs-PEG-(FR- α +Tyro3) in normal and CRC 3D *in vitro* models. Subsequently, to evaluate the uptake difference between 2D and 3D cell models for all types of GNPs constructs.

5.2 Introduction

In order to validate GNPs for their efficacy in delivery and internalisation, all 4 samples of GNPs constructs were incubated with 3D *in vitro* normal and CRC models as developed and characterised in chapter 4. Each of the 4 GNPs samples at 50ng were incubated with all three cell models under the same conditions as all the 2D experiments conducted in chapter 3. 50ng was chosen as it was the most internalised quantity of the samples in the cells using ICP-OES as well as evident from visualising the GNPs using the confocal microscopy. As mentioned earlier in chapter 4, 3D normal and CRC *in vitro* organotypic raft models were developed to demonstrate the uptake and delivery efficiency due to the fact that 2D monolayer of cells do not represent *in vivo* pathophysiology. Consequently, the results obtained from the 2D monolayers experiments are poorly translated in the clinical trials (Duval *et al.*, 2017). The organotypic raft model used provides a scaffold for the cells to grow, proliferate and organise in 3D similar to that observed *in vivo*. ECM proteins such as collagen I and III, along with others, are abundantly found in the dermis of the skin (Weber *et al.*, 1984) and (Watt and Fujiwara, 2011) which are also present in the lamina propria of the normal colon (Berk *et al.*, 2008). Therefore, the de-epidermalised dermis as scaffold provides similar structure of support mimicking the colonic physiology found *in vivo*. This chapter presents results from studies in detail interaction of GNPs with 3D normal and CRC models and compares it with 2D experiments performed on monolayer of cells grown upon a plastic surface.

5.3 Methods and materials

5.3.1 3D cell culture

3D models were developed and characterised in chapter 4. Prior to the internalisation experiments, 3D models were developed and placed in a humidified atmosphere in the incubators under the relevant cell culture media.

5.3.2 Uptake in normal vs. CRC models

Before being subjected to GNPs internalisation experiments, the media in the 6-well plate containing 3D models was aspirated. Unlike 2D models where a constant flat surface was available for GNPs in the media to attach to, 3D models had only limited surface area for GNPs treatment. Therefore, great precaution was taken that GNPs were not aliquoted out of the 3D-



Figure 50: An example of GNPs aliquoting inside the O-ring placed on a CRC 3D model.

-model area as it would underestimate the total internalisation efficiency. 3D organotypic raft models were immersed in 600 μ l of media: normal colon 3D model in MEM, and Duke's B and colorectal cancer 3D models in RPMI1640 and DMEM, respectively. To ensure all GNP constructs used in the experiment do not leak out, rubber O-rings were placed on top of each models and 50ng of all GNP constructs in relevant medium were allowed to interact with 3D models in the centre of the ring for 4 hours at 37 °C and 5% CO₂. One 3D model from every 3D normal and CRC models was used as a control without any GNPs treatment.

5.3.3 ICP-OES

After the incubation, O-rings were removed, and all 3D models were washed 4 times with 1X PBS to remove excess GNPs. Subsequently, all 3D models were digested and dissolved in fresh *aqua regia* for 24 hours. The 24 hours' time frame was chosen since it took full 24 hours to digest the entire 3D model along with the scaffold. Later, the entire content of the digested 3D model was diluted up to 100ml by adding de-ionised water in a round-bottomed flask and subjected to ICP-OES analysis. All the condition of the operated ICP-OES instrument was similar to the 2D experiment as mentioned in chapter 3.

5.4 Results

5.4.1 GNPs uptake in all normal vs CRC 3D models

The ICP-OES technique was utilised here again (similar to chapter 3) due to its versatility in detecting minute gold amounts in the sample. Here, entire 3D models after excess washing with 1X PBS were processed in *aqua regia*, decomposed and ionised to trace the gold content via photoemission spectra. Due to the above-mentioned washing step, any gold amount retrieved from the experiment is considered to have up taken or internalised by the 3-dimensional arrangement or multiple layers of the cells. Hence, results reveal the internalisation efficiency of GNPs in a 3D environment.

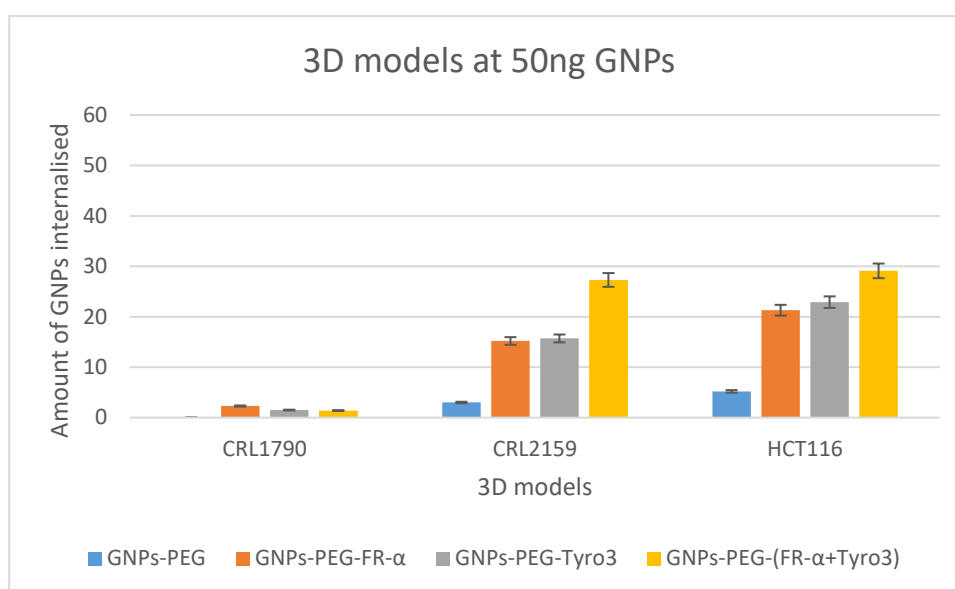


Figure 51: Internalisation efficiency of all GNPs constructs in normal and CRC 3D models (n=3). Name of the cell lines are mentioned that is representative of model developed using it. Error bars represents SD.

All three models incubated with all 4 GNPs showed selective uptake in 3D CRC models vs. normal 3D models. After incubation, the entire 3D model was digested in *aqua regia* and the resulting suspension processed via ICP-OES. The data expressed here are the amount of GNPs internalised by the cells arranged in 3 dimensions. GNPs-PEG was used as a control. In a normal 3D model, the internalisation was minimal with less than 5ng for each type of GNPs and no significant uptake for GNPs-PEG. However, with CRC models there was a high number of GNPs penetration due to overexpressed FR-α and Tyro3 receptors. Although there was some

uptake of GNPs-PEG in cancer 3D models, they were in extremely low amount (<5ng) compared to single and double-antibody coated GNPs owing to upregulated FR- α and Tyro3 receptors. In both CRC 3D models, single antibody-coated GNPs (GNPs-PEG-FR- α and GNPs-PEG-Tyro3) had internalisation significantly less than that of double antibody-coated GNPs (GNPs-PEG-(FR- α +Tyro3)) ($p<0.05$). The difference in internalisation between single and double antibody-coated GNPs was approximately 10ng for both CRC 3D models ($p<0.05$). All 3D models without GNPs showed no GNPs signals which further implies that no matrix effects were observed that can overestimate the GNPs signal in 3D *in vitro* models (data not shown).

5.4.2 Comparison of uptake between 2D and 3D models

Comparison of uptake of all GNPs constructs at 50ng between 3D models and cells grown in monolayers (2D) from all three cell lines is shown in Figure 52, Figure 53 and Figure 54, respectively. In general, GNPs 2D cell monolayers from every cell line had internalised more GNPs in comparison with their respective 3D models. For a normal 3D model (Figure 52), uptake of all GNPs construct remained low due to low expression of FR- α and Tyro3 receptors compared to 2D monolayer, especially for GNPs-PEG where no internalisation had been observed. Similarly, CRC 3D models out of CRL2159 and HCT116 cell lines had internalisation lower than that of 2D counterparts, respectively. For CRC CRL2159 3D model (Figure 53), the internalisation was 15ng-20ng less than that of uptake into monolayers of CRL2159 cells. Likewise, HCT116 3D model (Figure 54) also had internalisation up to 15ng less than of HCT116 monolayer of cells.

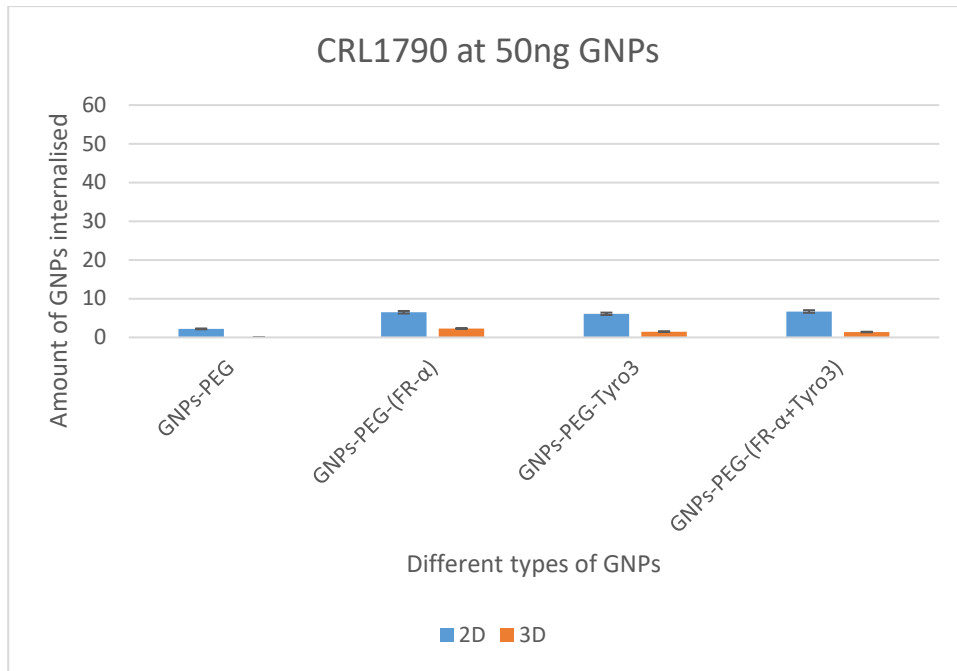


Figure 52: Internalisation of all 4 GNPs constructs in normal 3D model vs CRL1790 2D monolayer of cells at 50ng. Error bars represents SD (n=3).

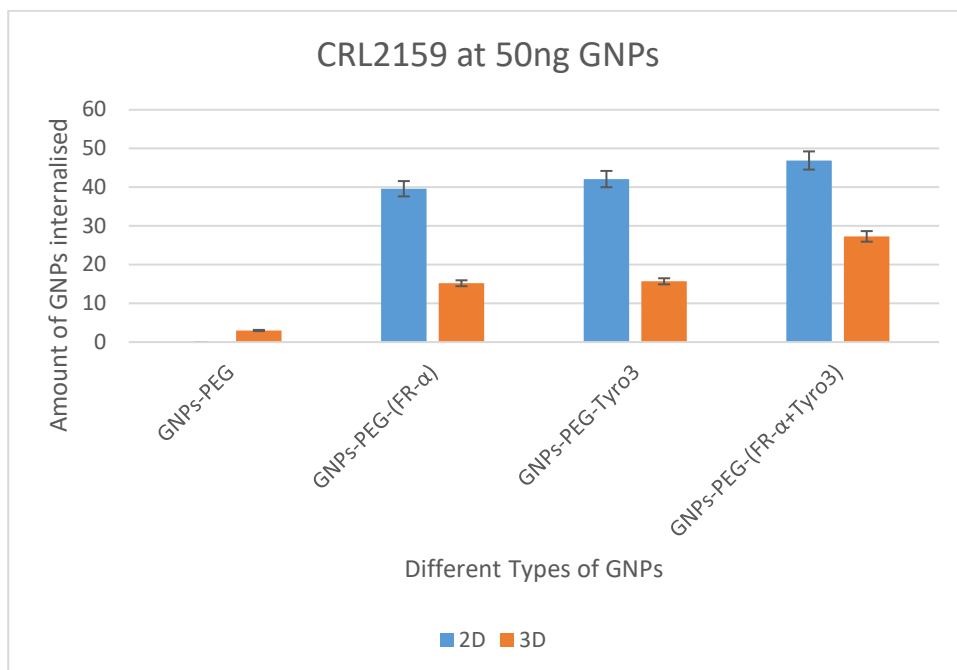


Figure 53: Internalisation of all 4 GNPs constructs in CRC 3D model vs CRL2159 2D monolayer of cells at 50ng. Error bars represents SD (n=3).

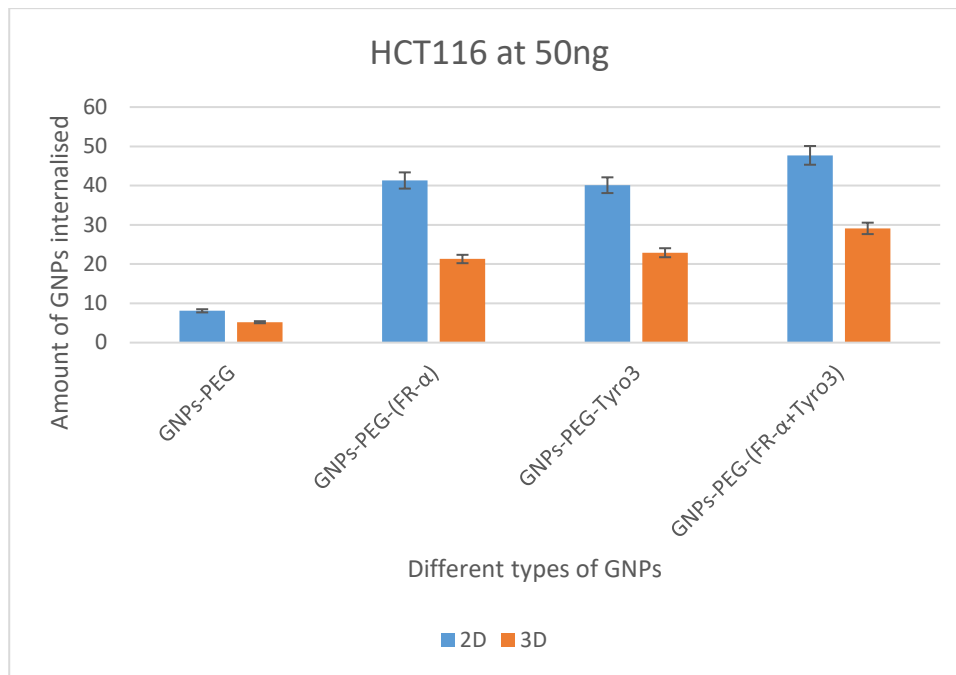


Figure 54: Internalisation of all 4 GNPs constructs in CRC 3D model vs HCT116 2D monolayer of cells at 50ng. Error bars represents SD (n=3).

5.5 Discussion

In the present study, organotypic *in vitro* normal and two CRC 3D models were used to test the efficacy of 1) internalisation of antibody-coated GNPs vs control (GNPs-PEG) 2) internalisation of single antibody-coated GNPs vs. double antibody-coated GNPs and 3) internalisation difference of all GNPs constructs at 50ng between 2D grown monolayer of cells vs. 3D *in vitro* models. This is the first study to investigate GNPs internalisation in 3D models using de-epidermalised dermis unlike other studies involving spheroids (Huang *et al.*, 2012; Rane and Armani, 2016). The experiments have resulted in showing FR- α and Tyro3 targeted GNPs had significantly higher uptake efficiencies rather than control GNPs-PEG in 3D CRC models compared to normal 3D model. This is due to the overexpressed FR- α and Tyro3 receptors. Secondly, double antibody-coated GNPs had higher internalisation efficacy than that of single antibody-coated GNPs. A minute uptake of GNPs-PEG in CRC 3D models was seen but it was very minimal. Targeting FR- α and Tyro3 receptors simultaneously has revealed superior uptake efficiency of double antibody-coated GNPs in comparison to GNPs-PEG and single antibody-coated GNPs, respectively in CRC 3D models.

With regards to uptake and internalisation between 2D vs. 3D models, a considerable difference was observed between the two platforms. A vital factor influencing the uptake of GNPs is to penetrate the tumour (multilayer of cells). Regardless of the size, shape and type of conjugation, an important aspect remains is a large-scale testing of synthesised GNPs. To circumvent it, 2D monolayer is opted normally to narrow down the types of GNPs chosen for *in vitro* experiments. However, these experiments do not fully translate the result clinically *in vivo*. Hence, 3D models are opted more and more. It is very well demonstrated that there are significant differences of cell behaviour between the cells in 2D and 3D (Debnath and Brugge, 2005; Pampaloni, Reynaud and Stelzer, 2007; Yamada and Cukierman, 2007). For e.g., potential drug that had proven effective in 2D cell monolayers was proven less effective in 3D cell culture models (Hirschhaeuser *et al.*, 2010). Similarly, the experiment concluded in

showing a significant difference in uptake efficiency between 2D format and 3D *in vitro* models. All 3D *in vitro* models have demonstrated an attenuated uptake of GNPs across all types of GNPs constructs compared to 2D counterparts at 50ng. This results from the penetration efficiency of all the GNPs across multiple layers of the cells arranged in 3D.

Several other experiments have envisaged to study the difference between uptake in 2D and 3D *in vitro* models. In one experiment, 2nm, 6nm and 15nm tiopronin coated GNPs were used to study the internalisation in breast cancer cells (MCF-7). It was seen that the internalisation of small GNPs (2nm) was higher in 3D cellular spheroid than 2D monolayer compared to 6nm and 15nm GNPs (Huang *et al.*, 2012). This result is contrary to the one obtained in this thesis. However, it should be noted that the size of the GNPs used in this project was ~30nm compared to their 2nm. Therefore, the reduced uptake could be due to the large size of the GNPs used. However, in a separate experiment citrate-capped and protein-functionalised 50nm GNPs have shown the highest internalisation efficiency in cervical cancer cells (HeLa) (Chithrani and Chan, 2007) and (Chithrani, Ghazani and Chan, 2006). Such contrary evidence proves that uptake is highly dependent on interaction between protein on GNPs surface and its targeted biomolecule (Yue *et al.*, 2017). Therefore, work carried in a present project results from the highest possible uptake as it was mediated via the interaction of mAbs on the GNPs surface to its designated target receptors. Additionally, in an attempt to understand the uptake efficiency of GNPs in 3D cultured spheroid using HCT116 cell lines, it was observed that 30nm naked GNPs had highest internalisation efficiency compared to 10nm, 50nm, and 70nm GNPs. However, when compared with 2D monolayers of HCT116 cell lines, the uptake of 10nm, 50nm and 70nm GNPs had shown significant differences in uptake. This signifies the importance of lack of inter-cellular and nano-architecture in 2D platform that helps in diffusion and transportation of GNPs (Rane and Armani, 2016). Similar difference of uptake was also seen in this project; 3D microenvironment has played a crucial role in determining

GNPs internalisation efficiency. The reduced uptake of GNPs in the 3D *in vitro* models compared to its 2D counterpart has demonstrated GNPs behaviour in its delivery and internalisation.

5.6 Conclusions

3D cell culture was used to determine the internalisation and uptake efficacy of GNPs in CRC vs normal models. Normal colon 3D model showed no uptake of GNPs-PEG whereas single and double antibody-coated GNPs had seen slight increase in GNPs uptake (Figure 51). In comparison, 3D CRC models have higher internalisation due to upregulated FR- α and Tyro3 receptors (Figure 51). In that, single antibody-coated GNPs were less internalised than that of double antibody-coated GNPs (GNPs-PEG-(FR- α +Tyro3)). This outcome is due to simultaneous targeting of FR- α and Tyro3 novel receptor in CRC compared to FR- α or Tyro3 alone. Another deduction from these results is the difference of uptake between 3D *in vitro* models and 2D monolayers of cell. Normal and CRC 3D *in vitro* models developed showed the discrepancy between 2D monolayer and 3D models for their ability to show GNPs internalisation efficacy. Due to direct availability and absence of complex multicellular structure, GNPs were largely internalised in 2D monolayers of cells compared to the respective 3D models.

CHAPTER 6

Discussion

6.1 Discussion

CRC ranks fourth worldwide as the cause of mortality and morbidity. CRC develops over the span of 10 years in a process called adenoma-carcinoma sequence (Gonzalez-Pons and Cruz-Correa, 2015; Tariq *et al.*, 2016). Due to its asymptomatic nature, there is no method for early diagnosis. Later, however, upon diagnosis CRC will have metastasised to distant sites in the body where it becomes inoperable. Therefore, novel means are envisaged to target the CRC tumour. As such, GNPs are opted and considered to be suitable for targeting CRC. GNPs have been extensively reviewed in chapter 1. GNPs possess unique chemical, physical and electrical properties which are different than its bulk form. GNPs also exhibit SPR property that is characteristic of GNPs with specific shapes and sizes (Yang *et al.*, 2019). Thus, different facets of biomedical sciences can facilitate the use of GNPs for e.g. biosensor, antibiotic resistance, imaging, drug delivery and cancer (Elahi, Kamali and Baghersad, 2018). However, in order to make viable use of GNPs in clinical settings for diagnosis and treatment, its delivery threshold in the tumour must be increased. It is noted that of all the GNPs used to target tumours, only a meagre 0.7% (median) reaches to a solid tumour which leads to its poor clinical translation (Wilhelm *et al.*, 2016). Therefore, GNPs were engineered to target specific receptors on CRC cell's surface to enhance overall delivery and internalisation of GNPs.

Various protein/antibodies-coated GNPs were used to target different cancers and its cell lines. This includes EGFR-targeted GNPs in epithelial carcinoma (El-Sayed, Huang and El-Sayed, 2006), breast cancer (Dreaden *et al.*, 2009) and pancreatic cancer (Patra *et al.*, 2010) as well as folate receptors in cervical cancer (Zhang *et al.*, 2010) and transferrin receptors in breast tumour (Li *et al.*, 2009). To overcome potential problem of delivery and internalisation, two different receptors were selected for targeting simultaneously; FR- α and Tyro3, both of which are overexpressed on CRC cells (shown in chapter 2). Tyro3 is a novel tyrosine kinase receptor recently shown to be a viable target in CRC (Schmitz *et al.*, 2016) and FR- α was shown before for its targeting efficiency (Garcia-Bennett, Nees and Fadeel, 2011). The thesis

was aimed at increasing the overall threshold of GNPs (GNPs-PEG-(FR- α +Tyro3)) in CRC cells so that they can be used in biomedical applications. However, before its cellular applications, GNPs were characterised for their size, stability, attachment of antibodies and amount of antibodies attached to a single GNP. Consequently, the results demonstrated that GNPs had an average size of 30nm and were highly stable as concluded via a stability assay. Stability of the GNPs against the salt in physiological conditions is vital when considered for biological applications. Consequently, increase in ionic strength via addition of salt results in aggregation of GNPs as a measure to test the potency of the GNPs (Boisselier and Astruc, 2009). Hence, GNPs constructs have been tested at different NaCl concentrations. GNPs used in this research were, therefore, highly stable (at 1M NaCl) and feasible for biological application. Similar assay was also performed to test the stability of glutamic-coated GNPs wherein different NaCl concentration was used to determine its stability and were found highly monodispersed (Wangoo *et al.*, 2008). UV-Vis, DLS and MALDI-TOF mass spectrometry ascertained the attachment of the antibodies. Besides analytical techniques as mentioned above, Bradford assay quantified the average number of antibodies attached to GNPs which was approximately 7 antibodies per GNP as consistently found in two separate studies using similar sized GNPs (S. Kumar, Aaron and Sokolov, 2008) and (Eck *et al.*, 2008).

Internalisation of GNPs into CRC cells was studied via two mechanisms; 1) confocal microscopy and 2) ICP-OES. Whereas confocal ascertained the localisation of GNPs in the cells via fluorescence, ICP-OES were able to determine the amount internalised in the cells. As demonstrated in chapter 3, GNPs was found in the cytoplasm of the cells and around its periphery. The possible mechanism of entry into the cells was RME. This can be deduced from the study where GNPs conjugated with folate targeted HeLa cells and found to have entered the cytoplasm via RME (Kim *et al.*, 2015). ICP-OES mass spectrometry helped quantified GNPs (0ng- 50ng) in the CRC cells. This thesis has also shown for the first time the targeting

of GNPs using Tyro3 receptors as well as its comparison with FR- α receptor in up taking the GNPs. To that end, it was shown that the internalisation of GNPs using GNPs-PEG-FR- α and GNPs-PEG-Tyro3 were almost similar implicating that the respective receptors had similar internalisation efficiency. Furthermore, for all antibody-coated GNPs incubated (0ng – 50ng), there was a concomitant increase in the GNPs levels in the CRC cells (CRL2159 and HCT116) using ICP-OES. CRL1790 had least internalisation due to the fact that it did not express or had a low number of FR- α or Tyro3 receptors. ICP-OES also showed that GNPs-PEG-(FR- α +Tyro3) was the most internalised compared to GNPs-PEG-FR- α or GNPs-PEG-Tyro3. Although the difference of uptake was small between single and double-antibody coated GNPs in CRC (CRL2159 and HCTL116) cells, it was statistically significant ($p<0.05$).

Recently, under a similar rationale to increase delivery of GNPs into a tumour, 4T1 tumour-bearing BALB/c mouse were injected with two different GNPs doses; low (0.2 trillion GNPs) and high (50 trillion GNPs). Consequently, it was found that with a high dose 12% of the GNPs were taken up by the tumour whereas only 0.7% for the low dose (Ouyang *et al.*, 2020). The increase from 0.7% to 12% is nevertheless still low required for successful biomedical application. This strongly suggests that more work needed to be done in order to circumvent the GNPs delivery into the tumour. It must also be noted that GNPs used in this experiment were non-targeted (PEGylated GNPs) unlike the one used in this thesis. Therefore, using GNPs targeting specific proteins could lead to increased internalisation than observed. Visually, confocal microscopy had shown the localisation of GNPs to be in the cytoplasm which was associated with the green fluorescent signals.

Furthermore, 1 normal and 2 CRC organotypic raft models were developed in order to assess the internalisation efficiency in 3-dimensionally arranged cells to mimic an *in vivo* like environment. These models were validated using H&E and IHC staining before being subjected for GNPs internalisation experiments. CK7 and CK20 markers were used to characterise

normal and cancer 3D models where the normal model had demonstrated the expression pattern of CK20+/CK7+ and cancer models CK20+/CK7-. All four types of GNPs at 50ng were exposed to normal and cancer 3D models were under similar condition as 2D cell culture to compare and contrast the internalisation efficacy between 2D and 3D platforms. 3D models too have shown higher internalisation efficiency for GNPs-PEG-(FR- α +Tyro3) compared to GNPs-PEG-FR- α and GNPs-PEG-Tyro3. However, when compared with the internalisation with its 2D counterparts, 3D format showed less uptake. This could in part due to the 3D arrangement of cells where the multiple layers of cells are observed in contrast to one single layer of cells. Furthermore, several studies were conducted to analyse the distribution and penetration profile of nanoparticles using 3D cell culture system. In one study, GNPs <20nm were used in multicellular spheroids had shown superior penetration ability than that of large sized GNPs (Huang *et al.*, 2012). In yet another study, particles <10nm were shown to be internalised in the breast cancer tumour sphere than larger sizes. Therefore, size also contributes towards the internalisation efficacy. As such, reduced uptake in this research can be reconciled by the fact that GNPs were 30nm and larger. Also, in 3D *in vitro* models, GNPs would have to circumvent their way to reach every cell whereas in 2D monolayer the cells are directly and superficially available. This thesis is also the first to use de-epidermalised dermis for CRC 3D model development in order to investigate the role of GNPs internalisation.

6.2 Conclusions

This thesis has demonstrated and bridged the gap by exploring simultaneous targeting of FR- α and Tyro3 receptors in order to increase uptake and delivery efficiency of GNPs into the CRC cells. By comparison, works carried out so far mostly used single receptor targeting with either folate (Banu *et al.*, 2015), transferrin (Li *et al.*, 2009), EGFR (Patra *et al.*, 2010) or VEGFR targeted GNPs (Pan *et al.*, 2014). Additionally, Tyro3, a novel tyrosine kinase receptor was used in order to increase GNP's uptake efficiency together with FR- α . The research has shown for the first time the targeting of Tyro3 using GNPs to enhance delivery and uptake. Cellular internalisation was quantified using ICP-OES and localisation was studied using confocal microscopy. Both methods have shown the internalisation of the GNPs into the cells. GNPs-PEG-(FR- α +Tyro3) mediated targeting resulted in superior uptake when compared with GNPs-PEG-FR- α and GNPs-PEG-Tyro3 increasing overall uptake threshold of GNPs in cancer cells. Such construct can be employed using different nanoparticles such as iron oxide, quantum dots, silver nanoparticles as well as liposomes which exploits different weaknesses of cancer. Targeting different receptors also helps in targeting cancer cells with heterogeneous cell populations (Hosta-Rigau *et al.*, 2010). Additionally, once GNPs are inside the cytoplasm of the cancer cell, it can be used in conjunction with other technologies such as hyperthermia using non-invasive radiofrequency, X-contrast behaviour etc as well as delivery vehicle for therapeutic intervention and diagnosis of cancer (Huang *et al.*, 2006).

Moreover, 3D organotypic models that were developed and validated to investigate the internalisation of the GNPs in a 3D environment was observed to show difference in uptake due to 3-dimensional organisation of cells and larger GNPs size compare to its 2D counterparts. Therefore, GNPs <20nm can increase further penetration and uptake of GNPs *in vivo*. Also, the study of penetration efficiency of all the GNPs constructs in CRC and normal 3D models would have proven beneficial to see how size, shape and conjugation affects their internalisation in multiple layers of cells. Results obtained from current 3D *in vitro* models

does not allow to understand the amount of GNPs penetration. Since ICP-OES quantifies overall GNPs internalised, it does not say if the data gathered were from the GNPs internalised from the top layer of cells or penetrated through the multiple layers of cells. As an example, two-photon microscopy was used on 14 μ m thick histological sections of the skin to assess the penetration capability of different charge, shape and functionality of GNPs (Fernandes *et al.*, 2015). In another study, tape-stripping method was employed wherein different layers of skins were tape-stripped, digested and subjected to ICP-OES to quantify the level of GNPs penetration through the skin (Larese Filon *et al.*, 2011). Therefore, penetration efficiency of GNPs combined with internalisation can shed more light on GNPs uptake in cancer cells and behaviour in 3D environment.

6.3 Future work

In order for GNPs to be fully successful in biomedicine further testing on its uptake efficiency needs to be carried out. To begin with, I would study size dependent internalisation to assess different sizes of GNPs that can increase the minimum threshold of GNPs entering the tumour cells. It would also have high penetration and, therefore, increased internalisation rates. Smaller size would also help in excretion from the biological system as pores in the glomerulus walls of the kidney are approximately 6nm (Bayford *et al.*, 2017). Also, since toxicity depends on the proteins and ligands attached, I would assess the toxicity of the used GNPs via MTT or LDH assay. Furthermore, if possible, I would also employ mouse models to understand pharmacokinetics of the used GNPs, its deposition in the organs such as kidney, liver and spleen including its excretion criteria.

Appendix

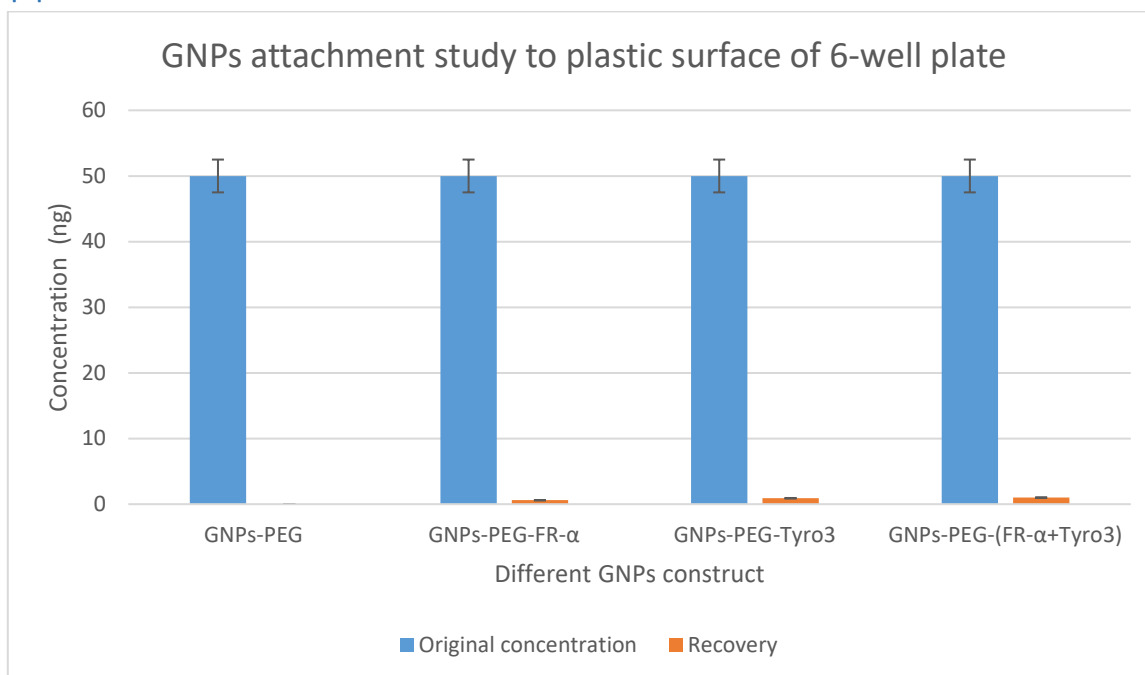


Figure 55: GNPs attachment study to plastic surface of 6-well plate. All GNPs were incubated for 4 h at 37 °C and in 5% CO₂ in the absence of cells ($p < 0.05$). Each sample in the well was processed through in a similar manner as with the cell sample. Error bars indicate SD. n=3

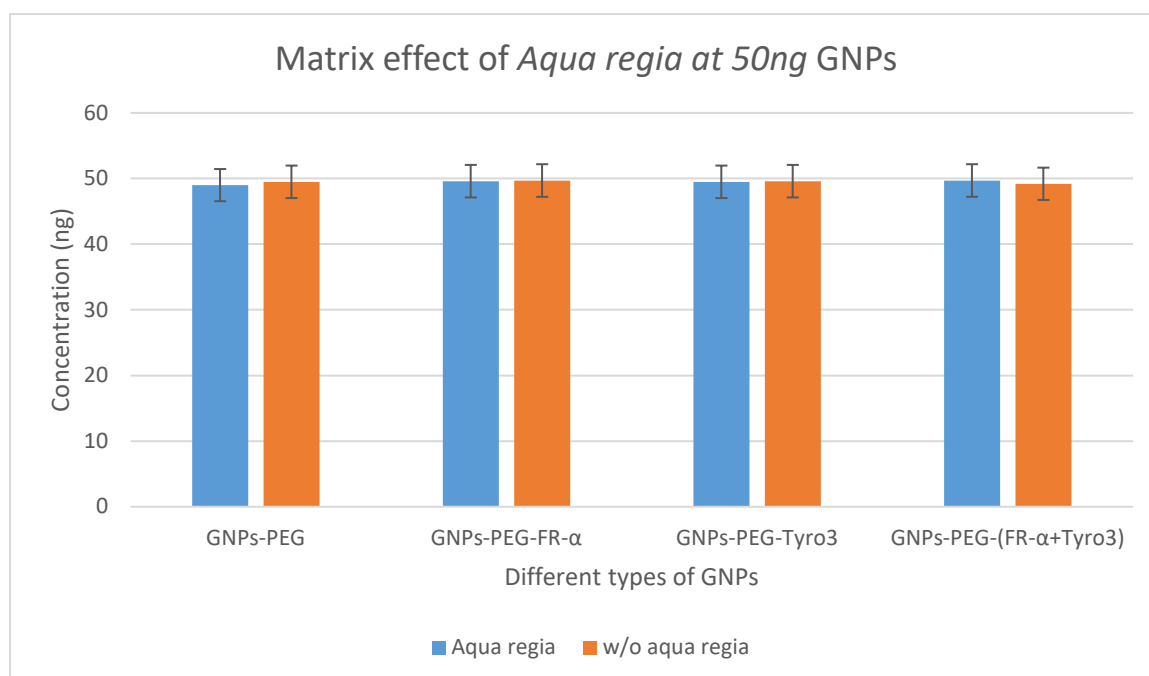


Figure 56: *Aqua regia* matrix effect study. ICP-OES detection of 50ng GNPs with and without *aqua regia* for all GNPs constructs. All GNPs were incubated for 4 h at 37 °C and in 5% CO₂ in the absence of cells ($p > 0.05$). Error bars indicate SD. n=3

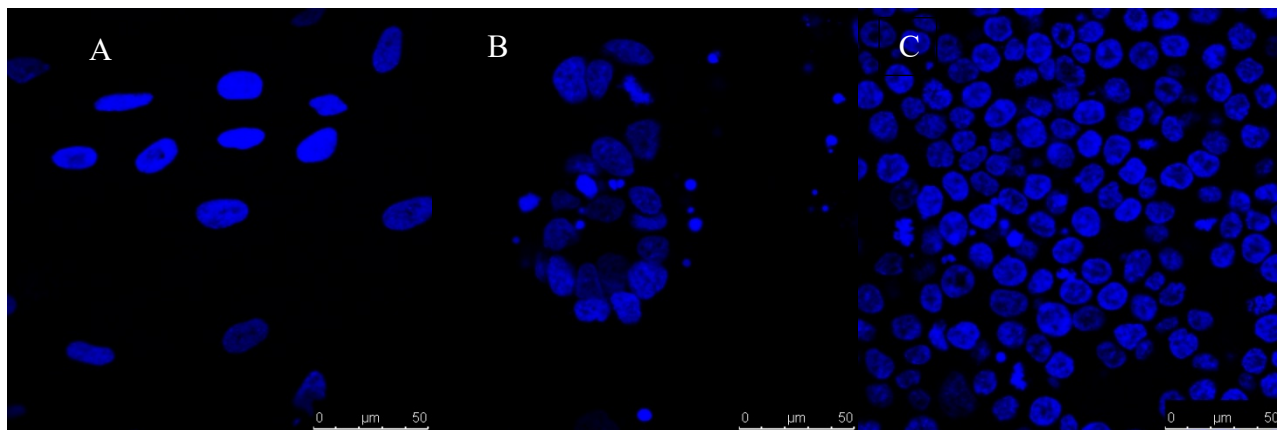


Figure 57: All three cell lines A) CRL1790, B) CRL2159 and C) HCT116 from confocal microscopy is shown. The images represented as control for each cell line without any antibody-coated GNPs. The nuclei of the cell is represented in blue. Scale bar = 50 μ m. Magnification 40X.

Bibliography

1. Akhter, S. *et al.* (2011) 'Cancer Targeted Metallic Nanoparticle: Targeting Overview, Recent Advancement and Toxicity Concern.', *Current pharmaceutical design*. doi: 10.2174/138161211796391001.
2. Ali Mansoori, G., Brandenburg, K. S. and Shakeri-Zadeh, A. (2010) 'A comparative study of two folate-conjugated gold nanoparticles for cancer nanotechnology applications', *Cancers*. doi: 10.3390/cancers2041911.
3. Alivisatos, P. (2004) 'The use of nanocrystals in biological detection', *Nature Biotechnology*, 22(1), pp. 47–52. doi: 10.1038/nbt927.
4. Alkilany, A. M. and Murphy, C. J. (2010) 'Toxicity and cellular uptake of gold nanoparticles: what we have learned so far?', *Journal of nanoparticle research : an interdisciplinary forum for nanoscale science and technology*. Department of Chemistry, University of Illinois at Urbana-Champaign, Urbana, IL 61801 USA., 12(7), pp. 2313–2333. doi: 10.1007/s11051-010-9911-8 [doi].
5. Allen, T. M. (2002) 'Ligand-targeted therapeutics in anticancer therapy', *Nat Rev Cancer*, 2(10), pp. 750–763. Available at: <http://dx.doi.org/10.1038/nrc903>.
6. Amendola, V. and Meneghetti, M. (2009) 'Size evaluation of gold nanoparticles by UV-vis spectroscopy', *Journal of Physical Chemistry C*. doi: 10.1021/jp8082425.
7. Anacker, D. and Moody, C. (2012) 'Generation of Organotypic Raft Cultures from Primary Human Keratinocytes', *Journal of Visualized Experiments*. MyJoVE Corporation, (60). doi: 10.3791/3668.
8. Andrei, G. *et al.* (2005) 'Organotypic epithelial raft cultures as a model for evaluating compounds against alphaherpesviruses', *Antimicrobial Agents and Chemotherapy*. doi: 10.1128/AAC.49.11.4671-4680.2005.
9. Antony, A. C. (1996) 'Folate Receptors', *Annual Review of Nutrition*, 16(1), pp. 501–521. doi: 10.1146/annurev.nu.16.070196.002441.
10. Arbea, L. *et al.* (2010) 'Intensity-modulated radiation therapy (IMRT) vs. 3D conformal radiotherapy (3DCRT) in locally advanced rectal cancer (LARC): Dosimetric comparison and clinical implications', *Radiation Oncology*. BioMed Central, 5(1), pp. 1–9. doi: 10.1186/1748-717X-5-17.
11. Arvizo, R., Bhattacharya, R. and Mukherjee, P. (2010) 'Gold nanoparticles: opportunities and challenges in nanomedicine', *Expert opinion on drug delivery*. Cancer Center, Department of Biochemistry and Molecular Biology, Mayo Clinic, Rochester, MN 55905, USA., 7(6), pp. 753–763. doi: 10.1517/17425241003777010 [doi].
12. AshaRani, P. V. *et al.* (2009) 'Cytotoxicity and genotoxicity of silver nanoparticles in human cells', *ACS Nano*. doi: 10.1021/nn800596w.
13. Baharvand, H. *et al.* (2006) 'Differentiation of human embryonic stem cells into hepatocytes in 2D and 3D culture systems in vitro', *International Journal of Developmental Biology*. doi: 10.1387/ijdb.052072hb.
14. Baish, J. W. *et al.* (2011) 'Scaling rules for diffusive drug delivery in tumor and normal tissues', *Proceedings of the National Academy of Sciences*, 108(5), pp. 1799–1803. doi: 10.1073/pnas.1018154108.
15. Baker, A. M. *et al.* (2011) 'The role of lysyl oxidase in SRC-dependent proliferation and metastasis of colorectal cancer', *Journal of the National Cancer Institute*. doi: 10.1093/jnci/djq569.
16. Baker, A. M. *et al.* (2013) 'Lysyl oxidase enzymatic function increases stiffness to drive colorectal cancer progression through FAK', *Oncogene*. doi: 10.1038/onc.2012.202.
17. Banu, H. *et al.* (2015) 'Doxorubicin loaded polymeric gold nanoparticles targeted to human folate receptor upon laser photothermal therapy potentiates chemotherapy in breast cancer cell lines', *Journal of Photochemistry and Photobiology B: Biology*. doi:

- 10.1016/j.jphotobiol.2015.05.008.
18. Bardelli, A. and Siena, S. (2010) ‘Molecular Mechanisms of Resistance to Cetuximab and Panitumumab in Colorectal Cancer’, *Journal of Clinical Oncology*, 28(7), pp. 1254–1261. doi: 10.1200/JCO.2009.24.6116.
 19. Barui, S. *et al.* (2014) ‘Simultaneous delivery of doxorubicin and curcumin encapsulated in liposomes of pegylated RGDK-lipopeptide to tumor vasculature’, *Biomaterials*. Elsevier, 35(5), pp. 1643–1656. doi: 10.1016/j.biomaterials.2013.10.074.
 20. Bayford, R. *et al.* (2017) ‘Emerging applications of nanotechnology for diagnosis and therapy of disease: A review’, *Physiological Measurement*, pp. R183–R203. doi: 10.1088/1361-6579/aa7182.
 21. Bayrak, R., Haltas, H. and Yenidunya, S. (2012) ‘The value of CDX2 and cytokeratins 7 and 20 expression in differentiating colorectal adenocarcinomas from extraintestinal gastrointestinal adenocarcinomas: cytokeratin 7-/20+ phenotype is more specific than CDX2 antibody.’, *Diagnostic pathology*. BioMed Central, 7, p. 9. doi: 10.1186/1746-1596-7-9.
 22. Bayrak, R., Yenidunya, S. and Haltas, H. (2011) ‘Cytokeratin 7 and cytokeratin 20 expression in colorectal adenocarcinomas’, *Pathology Research and Practice*. doi: 10.1016/j.prp.2010.12.005.
 23. Berk, L. • *et al.* (2008) *MOLECULAR CELL BIOLOGY SIXTH EDITION MOLECULAR CELL BIOLOGY SIXTH EDITION Integrating Cells into Tissues Integrating Cells into Tissues*. Available at: [http://www2.nsysu.edu.tw/wzhlab/cell biology PDF/ch19 part I.pdf](http://www2.nsysu.edu.tw/wzhlab/cell%20biology/PDF/ch19%20part%20I.pdf) (Accessed: 5 March 2019).
 24. Berners-Price, S. J. and Filipovska, A. (2011) ‘Gold compounds as therapeutic agents for human diseases’, *Metallomics*. doi: 10.1039/c1mt00062d.
 25. Bhatia, S. N. *et al.* (2009) ‘Computationally Guided Photothermal Tumor Therapy Using Long-Circulating Gold Nanorod Antennas’, *Cancer Research*.
 26. Bhattacharya, R. *et al.* (2007) ‘Attaching folic acid on gold nanoparticles using noncovalent interaction via different polyethylene glycol backbones and targeting of cancer cells’, *Nanomedicine: Nanotechnology, Biology, and Medicine*. doi: 10.1016/j.nano.2007.07.001.
 27. Bian, J. and Olesik, S. V. (2017) ‘Surface-assisted laser desorption/ionization time-of-flight mass spectrometry of small drug molecules and high molecular weight synthetic/biological polymers using electrospun composite nanofibers’, *Analyst*, 142(7), pp. 1125–1132. doi: 10.1039/c6an02444k.
 28. Biesecker, L. G., Gottschalk, L. R. and Emerson, S. G. (1993) ‘Identification of four murine cDNAs encoding putative protein kinases from primitive embryonic stem cells differentiated in vitro.’, *Proceedings of the National Academy of Sciences of the United States of America*. National Academy of Sciences, 90(15), pp. 7044–8. Available at: <http://www.ncbi.nlm.nih.gov/pubmed/8346215> (Accessed: 6 January 2019).
 29. Bird, A. P. (1986) ‘CpG-rich islands and the function of DNA methylation’, *Nature*, 321(6067), pp. 209–213. doi: 10.1038/321209a0.
 30. Birgersdotter, A., Sandberg, R. and Ernberg, I. (2005) ‘Gene expression perturbation in vitro - A growing case for three-dimensional (3D) culture systems’, *Seminars in Cancer Biology*. doi: 10.1016/j.semcancer.2005.06.009.
 31. Boisselier, E. and Astruc, D. (2009) ‘Gold nanoparticles in nanomedicine: preparations, imaging, diagnostics, therapies and toxicity’, *Chemical Society Reviews*. doi: 10.1039/b806051g.
 32. Boland, C. R. *et al.* (1998) ‘A National Cancer Institute Workshop on Microsatellite Instability for cancer detection and familial predisposition: development of international criteria for the determination of microsatellite instability in colorectal cancer.’, *Cancer research*, 58(22), pp. 5248–57. Available at: <http://www.ncbi.nlm.nih.gov/pubmed/9823339> (Accessed: 18 November 2018).
 33. Bosch, L. J. W. *et al.* (2011) ‘Molecular tests for colorectal cancer screening.’, *Clinical*

- colorectal cancer*, 10(1), pp. 8–23. doi: 10.3816/CCC.2011.n.002.
34. Bradford, M. (1976) ‘A Rapid and Sensitive Method for the Quantitation of Microgram Quantities of Protein Utilizing the Principle of Protein-Dye Binding’, *Analytical Biochemistry*. Elsevier BV, 72(1–2), pp. 248–254. doi: 10.1006/abio.1976.9999.
 35. Brar, S. K. and Verma, M. (2011) ‘Measurement of nanoparticles by light-scattering techniques’, *TrAC - Trends in Analytical Chemistry*. doi: 10.1016/j.trac.2010.08.008.
 36. Burdick, J. A. and Vunjak-Novakovic, G. (2009) ‘Engineered Microenvironments for Controlled Stem Cell Differentiation’, *Tissue Engineering Part A*. doi: 10.1089/ten.tea.2008.0131.
 37. Cai, W. *et al.* (2008) ‘Applications of gold nanoparticles in cancer nanotechnology’, *Nanotechnology, science and applications*. Departments of Radiology and Medical Physics, School of Medicine and Public Health, University of Wisconsin - Madison, Madison, Wisconsin, USA ; University of Wisconsin Paul P. Carbone Comprehensive Cancer Center, Madison, Wisconsin, USA., 1, pp. 17–32.
 38. Cao-Milán, R. and Liz-Marzán, L. M. (2014) ‘Gold nanoparticle conjugates: recent advances toward clinical applications’, *Expert Opinion on Drug Delivery*, 11(5), pp. 741–752. doi: 10.1517/17425247.2014.891582.
 39. Cassidy, J. *et al.* (2004) ‘XELOX (capecitabine plus oxaliplatin): Active first-line therapy for patients with metastatic colorectal cancer’, *Journal of Clinical Oncology*. J Clin Oncol, 22(11), pp. 2084–2091. doi: 10.1200/JCO.2004.11.069.
 40. Chan, P. W. W. *et al.* (2017) ‘Colorectal cancer screening.’, *Singapore medical journal*, 58(1), pp. 24–28. doi: 10.11622/smedj.2017004.
 41. Chen, C. *et al.* (2013) ‘Structural basis for molecular recognition of folic acid by folate receptors’, *Nature*, 500(7463), pp. 486–489. doi: 10.1038/nature12327.
 42. Chen, J. *et al.* (2012) ‘A restricted cell population propagates glioblastoma growth after chemotherapy.’, *Nature*. NIH Public Access, 488(7412), pp. 522–6. doi: 10.1038/nature11287.
 43. Cheung, A. *et al.* (2016) ‘Targeting folate receptor alpha for cancer treatment’, *Oncotarget*, 7(32), pp. 52553–52574. doi: 10.18632/oncotarget.9651.
 44. Chien, C. W. *et al.* (2016) ‘Targeting TYRO3 inhibits epithelial-mesenchymal transition and increases drug sensitivity in colon cancer’, *Oncogene*, 35(45), pp. 5872–5881. doi: 10.1038/onc.2016.120.
 45. Chithrani, B. D. and Chan, W. C. (2007) ‘Elucidating the mechanism of cellular uptake and removal of protein-coated gold nanoparticles of different sizes and shapes’, *Nano letters*. Institute of Biomaterials and Biomedical Engineering, Terrence Donnelly Center for Cellular and Biomolecular Research, University of Toronto, 160 College Street, 4th Floor, Toronto, Ontario M5S 3G9, Canada., 7(6), pp. 1542–1550. doi: 10.1021/nl070363y [doi].
 46. Chithrani, B. D., Ghazani, A. A. and Chan, W. C. W. (2006) ‘Determining the size and shape dependence of gold nanoparticle uptake into mammalian cells’, *Nano Letters*, 6(4), pp. 662–668. doi: 10.1021/nl052396o.
 47. Chnari, E. *et al.* (2006) ‘Nanoscale Anionic Macromolecules Can Inhibit Cellular Uptake of Differentially Oxidized LDL’, *Biomacromolecules*, 7(2), pp. 597–603. doi: 10.1021/bm0506905.
 48. Cho, K. *et al.* (2008) ‘Therapeutic Nanoparticles for Drug Delivery in Cancer’, *Clinical Cancer Research*. American Association for Cancer Research, 14(5), pp. 1310–1316. doi: 10.1158/1078-0432.CCR-07-1441.
 49. Choi, C. H. *et al.* (2010) ‘Mechanism of active targeting in solid tumors with transferrin-containing gold nanoparticles’, *Proceedings of the National Academy of Sciences of the United States of America*. Chemical Engineering, California Institute of Technology, Pasadena, CA 91125, USA., 107(3), pp. 1235–1240. doi: 10.1073/pnas.0914140107 [doi].
 50. Chu, P. G. and Weiss, L. M. (2002) ‘Keratin expression in human tissues and neoplasms.’,

- Histopathology*, 40(5), pp. 403–39. Available at: <http://www.ncbi.nlm.nih.gov/pubmed/12010363> (Accessed: 15 January 2019).
51. Chu, P., Wu, E. and Weiss, L. M. (2000) ‘Cytokeratin 7 and Cytokeratin 20 expression in epithelial neoplasms: A survey of 435 cases’, *Modern Pathology*. doi: 10.1038/modpathol.3880175.
 52. Cisterna, B. A. *et al.* (2016) ‘Targeted nanoparticles for colorectal cancer’, *Nanomedicine*, 11(8), pp. 2443–2456. doi: 10.2217/nnm-2016-0194.
 53. Connor, E. E. *et al.* (2005) ‘Gold Nanoparticles Are Taken Up by Human Cells but Do Not Cause Acute Cytotoxicity’, *Small*, 1(3), pp. 325–327. doi: 10.1002/sml.200400093.
 54. Corbierre, M. K. *et al.* (2001) ‘Polymer-stabilized gold nanoparticles and their incorporation into polymer matrices [13]’, *Journal of the American Chemical Society*. *J Am Chem Soc*, pp. 10411–10412. doi: 10.1021/ja0166287.
 55. Coulombe, P. A. *et al.* (1991) ‘Point mutations in human keratin 14 genes of epidermolysis bullosa simplex patients: genetic and functional analyses.’, *Cell*, 66(6), pp. 1301–11. Available at: <http://www.ncbi.nlm.nih.gov/pubmed/1717157> (Accessed: 15 January 2019).
 56. Crotti, S. *et al.* (2017) ‘Extracellular Matrix and Colorectal Cancer: How Surrounding Microenvironment Affects Cancer Cell Behavior?’, *Journal of Cellular Physiology*. doi: 10.1002/jcp.25658.
 57. Daniel, M. C. and Astruc, D. (2004) ‘Gold Nanoparticles: Assembly, Supramolecular Chemistry, Quantum-Size-Related Properties, and Applications Toward Biology, Catalysis, and Nanotechnology’, *Chemical Reviews*. doi: 10.1021/cr030698+.
 58. Davis, M. E., Chen, Z. and Shin, D. M. (2008) ‘Nanoparticle therapeutics: an emerging treatment modality for cancer’, *Nature Reviews Drug Discovery*, 7(9), pp. 771–782. doi: 10.1038/nrd2614.
 59. Davy, C. *et al.* (2005) ‘Using an Immortalized Cell Line to Study the HPV Life Cycle in Organotypic’, in *Human Papillomaviruses*. New Jersey: Humana Press, pp. 141–156. doi: 10.1385/1-59259-982-6:141.
 60. Debnath, J. and Brugge, J. S. (2005) ‘Modelling glandular epithelial cancers in three-dimensional cultures’, *Nature Reviews Cancer*. doi: 10.1038/nrc1695.
 61. Debucquoy, A. *et al.* (2009) ‘Molecular response to cetuximab and efficacy of preoperative cetuximab-based chemoradiation in rectal cancer’, *Journal of Clinical Oncology*. *J Clin Oncol*, 27(17), pp. 2751–2757. doi: 10.1200/JCO.2008.18.5033.
 62. Delaney, G. *et al.* (2005) ‘The role of radiotherapy in cancer treatment: Estimating optimal utilization from a review of evidence-based clinical guidelines’, *Cancer*. John Wiley & Sons, Ltd, pp. 1129–1137. doi: 10.1002/cncr.21324.
 63. Dickreuter, E. and Cordes, N. (2017) ‘The cancer cell adhesion resistome: Mechanisms, targeting and translational approaches’, *Biological Chemistry*. doi: 10.1515/hsz-2016-0326.
 64. Dimov, I. K. *et al.* (2011) ‘Integrated microfluidic array plate (iMAP) for cellular and molecular analysis’, *Lab on a Chip*, 11(16), p. 2701. doi: 10.1039/c1lc20105k.
 65. Dixit, S. *et al.* (2015) ‘Dual Receptor-Targeted Theranostic Nanoparticles for Localized Delivery and Activation of Photodynamic Therapy Drug in Glioblastomas’, *Molecular Pharmaceutics*. *Mol Pharm*, 12(9), pp. 3250–3260. doi: 10.1021/acs.molpharmaceut.5b00216.
 66. Doherty, G. J. and McMahon, H. T. (2009) ‘Mechanisms of Endocytosis’, *Annual Review of Biochemistry*, 78(1), pp. 857–902. doi: 10.1146/annurev.biochem.78.081307.110540.
 67. Doyle, A. D. *et al.* (2015) ‘Local 3D matrix microenvironment regulates cell migration through spatiotemporal dynamics of contractility-dependent adhesions’, *Nature Communications*. doi: 10.1038/ncomms9720.
 68. Drasler, B. *et al.* (2017) ‘Quantifying nanoparticle cellular uptake: Which method is best?’, *Nanomedicine*. Future Medicine Ltd., pp. 1095–1099. doi: 10.2217/nnm-2017-0071.
 69. Dreaden, E. C. *et al.* (2009) ‘Tamoxifen-poly(ethylene glycol)-thiol gold nanoparticle

- conjugates: enhanced potency and selective delivery for breast cancer treatment’, *Bioconjugate chemistry*. Department of Chemistry and Biochemistry, Georgia Institute of Technology, 901 Atlantic Drive NW, Atlanta, Georgia 30332-0400, USA., 20(12), pp. 2247–2253. doi: 10.1021/bc9002212 [doi].
70. Duan, Y. *et al.* (2016) ‘Overexpression of Tyro3 and its implications on hepatocellular carcinoma progression’, *International Journal of Oncology*, 48(1), pp. 358–366. doi: 10.3892/ijo.2015.3244.
 71. Duval, K. *et al.* (2017) ‘Modeling Physiological Events in 2D vs. 3D Cell Culture.’, *Physiology (Bethesda, Md.)*. American Physiological Society, 32(4), pp. 266–277. doi: 10.1152/physiol.00036.2016.
 72. Dykman, L. A. and Khlebtsov, N. G. (2014) ‘Uptake of engineered gold nanoparticles into mammalian cells’, *Chemical Reviews*. American Chemical Society, pp. 1258–1288. doi: 10.1021/cr300441a.
 73. Eck, W. *et al.* (2008) ‘PEGylated gold nanoparticles conjugated to monoclonal F19 antibodies as targeted labeling agents for human pancreatic carcinoma tissue’, *ACS Nano*, 2(11), pp. 2263–2272. doi: 10.1021/nn800429d.
 74. Ekert, J. E. *et al.* (2014) ‘Three-dimensional lung tumor microenvironment modulates therapeutic compound responsiveness in vitro - Implication for drug development’, *PLoS ONE*. doi: 10.1371/journal.pone.0092248.
 75. El-Sayed, I. H., Huang, X. and El-Sayed, M. A. (2005) ‘Surface plasmon resonance scattering and absorption of anti-EGFR antibody conjugated gold nanoparticles in cancer diagnostics: Applications in oral cancer’, *Nano Letters*. doi: 10.1021/nl050074e.
 76. El-Sayed, I. H., Huang, X. and El-Sayed, M. A. (2006) ‘Selective laser photo-thermal therapy of epithelial carcinoma using anti-EGFR antibody conjugated gold nanoparticles’, *Cancer Letters*, 239(1), pp. 129–135. doi: 10.1016/j.canlet.2005.07.035.
 77. Elahi, N., Kamali, M. and Baghersad, M. H. (2018) ‘Recent biomedical applications of gold nanoparticles: A review’, *Talanta*. Elsevier B.V., 184, pp. 537–556. doi: 10.1016/j.talanta.2018.02.088.
 78. Elnakat, H. and Ratnam, M. (2004) ‘Distribution, functionality and gene regulation of folate receptor isoforms: Implications in targeted therapy’, *Advanced Drug Delivery Reviews*. doi: 10.1016/j.addr.2004.01.001.
 79. Espinosa De Los Monteros, A. *et al.* (1999) ‘Coordinate Expression of Cytokeratins 7 and 20 in Feline and Canine Carcinomas’, *Veterinary Pathology*. doi: 10.1354/vp.36-3-179.
 80. Fang, C. *et al.* (2009) ‘Functionalized nanoparticles with long-term stability in biological media’, *Small*, 5(14), pp. 1637–1641. doi: 10.1002/smll.200801647.
 81. Fang, Y. and Eglen, R. M. (2017) ‘Three-Dimensional Cell Cultures in Drug Discovery and Development.’, *SLAS discovery : advancing life sciences R & D*. SAGE Publications, 22(5), pp. 456–472. doi: 10.1177/1087057117696795.
 82. Fernandes, R. *et al.* (2015) ‘Interactions of skin with gold nanoparticles of different surface charge, shape, and functionality’, *Small*. doi: 10.1002/smll.201401913.
 83. Feynman, R. (1959) ‘Conclusion : “ Plenty of Room at the Bottom ”’, *Engineering and Science* 22–36. doi: 10.1109/84.128057.
 84. Filbrun, S. L. and Driskell, J. D. (2016) ‘A fluorescence-based method to directly quantify antibodies immobilized on gold nanoparticles’, *Analyst*. doi: 10.1039/c6an00193a.
 85. Finkelstein, A. E. *et al.* (1976) ‘Auranofin. New oral gold compound for treatment of rheumatoid arthritis’, *Annals of the Rheumatic Diseases*, 35(3), pp. 251–257. doi: 10.1136/ard.35.3.251.
 86. Fischer, A. H. *et al.* (2008) ‘Hematoxylin and Eosin Staining of Tissue and Cell Sections’, *Cold Spring Harbor Protocols*, 2008(6), p. pdb.prot4986-pdb.prot4986. doi: 10.1101/pdb.prot4986.
 87. Fuchs, E. and Cleveland, D. W. (1998) ‘A structural scaffolding of intermediate filaments in

- health and disease.’, *Science (New York, N.Y.)*, 279(5350), pp. 514–9. Available at: <http://www.ncbi.nlm.nih.gov/pubmed/9438837> (Accessed: 15 January 2019).
88. Gao, H., Shi, W. and Freund, L. B. (2005) ‘Mechanics of receptor-mediated endocytosis’, *Proceedings of the National Academy of Sciences of the United States of America*, 102(27), pp. 9469–9474. doi: 10.1073/pnas.0503879102.
 89. Garcia-Bennett, A., Nees, M. and Fadeel, B. (2011) ‘In search of the Holy Grail: Folate-targeted nanoparticles for cancer therapy’, *Biochemical Pharmacology*. doi: 10.1016/j.bcp.2011.01.023.
 90. Geißler, A.-L. *et al.* (2017) ‘ATM mutations and E-cadherin expression define sensitivity to EGFR-targeted therapy in colorectal cancer’, *Oncotarget*, 8(10), pp. 17164–17190. doi: 10.18632/oncotarget.15211.
 91. Gheini, M. H. and Jalayer Naderi, N. (2017) ‘The Relationship Between Cytokeratins 7 and 20 Expression, and Prognostic Factors in Colon Adenocarcinoma: An Immunohistochemical Study.’, *Iranian journal of pathology*. Iranian Society of Pathology, 12(2), pp. 94–98. Available at: <http://www.ncbi.nlm.nih.gov/pubmed/29515629> (Accessed: 16 January 2019).
 92. Giljohann, D. A. and Mirkin, C. A. (2009) ‘Drivers of biodiagnostic development’, *Nature*, 462(7272), pp. 461–464. doi: 10.1038/nature08605.
 93. Goetz, J. G. *et al.* (2011) ‘Biomechanical remodeling of the microenvironment by stromal caveolin-1 favors tumor invasion and metastasis’, *Cell*. doi: 10.1016/j.cell.2011.05.040.
 94. Goitein, M. (2009) ‘How Best To Dispose of Extra-Tumoral Dose: A Cautionary Note for Intensity-Modulated Radiation Therapy’, *International Journal of Radiation Oncology*Biophysics*Physics*, 75(1), pp. 1–3. doi: 10.1016/j.ijrobp.2009.05.053.
 95. Gonzalez-Pons, M. and Cruz-Correa, M. (2015) ‘Colorectal Cancer Biomarkers: Where Are We Now?’, *BioMed Research International*. Hindawi, p. 149014. doi: 10.1155/2015/149014.
 96. Gonzalez, A. L. *et al.* (2005) ‘Optical absorbance of colloidal suspensions of silver polyhedral nanoparticles’, *Journal of Physical Chemistry B*. American Chemical Society, 109(37), pp. 17512–17517. doi: 10.1021/jp0533832.
 97. Graham, D. K. *et al.* (2014) ‘The TAM family: Phosphatidylserine-sensing receptor tyrosine kinases gone awry in cancer’, *Nature Reviews Cancer*, 14(12), pp. 769–785. doi: 10.1038/nrc3847.
 98. Griffith, L. G. and Swartz, M. A. (2006) ‘Capturing complex 3D tissue physiology in vitro’, *Nature Reviews Molecular Cell Biology*. doi: 10.1038/nrm1858.
 99. Gromnicova, R. *et al.* (2013) ‘Glucose-coated gold nanoparticles transfer across human brain endothelium and enter astrocytes in vitro’, *PLoS ONE*. doi: 10.1371/journal.pone.0081043.
 100. Gu, F. X. *et al.* (2007) ‘Targeted nanoparticles for cancer therapy’, *Nano Today*. Elsevier, 2(3), pp. 14–21. doi: 10.1016/S1748-0132(07)70083-X.
 101. Guess, C. M. *et al.* (2009) ‘A decreased ratio of laminin-332 $\beta 3$ to $\gamma 2$ subunit mRNA is associated with poor prognosis in colon cancer’, *Cancer Epidemiology Biomarkers and Prevention*. doi: 10.1158/1055-9965.EPI-08-1027.
 102. Hainfeld, J. F. *et al.* (2006) ‘Gold nanoparticles: a new X-ray contrast agent’, *The British Journal of Radiology*, 79(939), pp. 248–253. doi: 10.1259/bjr/13169882.
 103. Haiss, W. *et al.* (2007) ‘Determination of Size and Concentration of Gold Nanoparticles from UV/vis Spectra - Supporting Information’, *Analytical Chemistry*, 79(11), pp. 4215–4221. doi: 10.1021/ac0702084.
 104. Half, E., Bercovich, D. and Rozen, P. (2009) ‘Familial adenomatous polyposis’, *Orphanet Journal of Rare Diseases*, 4(1), p. 22. doi: 10.1186/1750-1172-4-22.
 105. Hatcher, O. and Kumar, Aswin A. (2014a) ‘Chemotherapy and radiotherapy for colorectal cancers’, *Surgery (United Kingdom)*. Elsevier Ltd, pp. 179–184. doi: 10.1016/j.mpsur.2014.01.005.
 106. Hatcher, O. and Kumar, Aswin A. (2014) ‘Chemotherapy and radiotherapy for colorectal cancers’, *Intestinal Surgery I*, 32(4), pp. 179–184. Available at:

<http://www.sciencedirect.com/science/article/pii/S0263931914000180>.

107. Hatcher, O. and Kumar, Aswin A. (2014b) 'Chemotherapy and radiotherapy for colorectal cancers', *Surgery (Oxford)*. Elsevier, 32(4), pp. 179–184. doi: 10.1016/J.MPSUR.2014.01.005.
108. Her, S., Jaffray, D. A. and Allen, C. (2017) 'Gold nanoparticles for applications in cancer radiotherapy: Mechanisms and recent advancements', *Advanced Drug Delivery Reviews*, pp. 84–101. doi: 10.1016/j.addr.2015.12.012.
109. Hirschhaeuser, F. *et al.* (2010) 'Multicellular tumor spheroids: An underestimated tool is catching up again', *Journal of Biotechnology*. doi: 10.1016/j.jbiotec.2010.01.012.
110. Ho, W. J. *et al.* (2010) 'Incorporation of multicellular spheroids into 3-D polymeric scaffolds provides an improved tumor model for screening anticancer drugs', *Cancer Sci*. doi: 10.1111/j.1349-7006.2010.01723.x.
111. Hojjat-Farsangi, M. (2014) 'Small-molecule inhibitors of the receptor tyrosine kinases: Promising tools for targeted cancer therapies', *International Journal of Molecular Sciences*. Int J Mol Sci, pp. 13768–13801. doi: 10.3390/ijms150813768.
112. Holleczeck, B. *et al.* (2015) 'On-going improvement and persistent differences in the survival for patients with colon and rectum cancer across Europe 1999-2007 - Results from the EURO CARE-5 study', *European Journal of Cancer*. doi: 10.1016/j.ejca.2015.07.024.
113. Hong, Y. and Rao, Y. (2019) 'Current status of nanoscale drug delivery systems for colorectal cancer liver metastasis', *Biomedicine and Pharmacotherapy*, 114. doi: 10.1016/j.biopha.2019.108764.
114. Hongisto, V. *et al.* (2013) 'High-Throughput 3D Screening Reveals Differences in Drug Sensitivities between Culture Models of JIMT1 Breast Cancer Cells', *PLoS ONE*. doi: 10.1371/journal.pone.0077232.
115. Hosta-Rigau, L. *et al.* (2010) 'Multifunctionalized gold nanoparticles with peptides targeted to gastrin-releasing peptide receptor of a tumor cell line', *Bioconjugate Chemistry*. American Chemical Society, 21(6), pp. 1070–1078. doi: 10.1021/bc1000164.
116. Hsiao, A. Y. *et al.* (2009) 'Microfluidic system for formation of PC-3 prostate cancer co-culture spheroids', *Biomaterials*. doi: 10.1016/j.biomaterials.2009.02.047.
117. Huang, H. *et al.* (2013) 'Peptide Hydrogelation and Cell Encapsulation for 3D Culture of MCF-7 Breast Cancer Cells', *PLoS ONE*. doi: 10.1371/journal.pone.0059482.
118. Huang, K. *et al.* (2012) 'Size-dependent localization and penetration of ultrasmall gold nanoparticles in cancer cells, multicellular spheroids, and tumors in vivo', *ACS Nano*. doi: 10.1021/nn301282m.
119. Huang, X. *et al.* (2006) 'Cancer cell imaging and photothermal therapy in the near-infrared region by using gold nanorods', *Journal of the American Chemical Society*. J Am Chem Soc, 128(6), pp. 2115–2120. doi: 10.1021/ja057254a.
120. Huff, T. B. *et al.* (2007) 'Hyperthermic effects of gold nanorods on tumor cells', *Nanomedicine*. doi: 10.2217/17435889.2.1.125.
121. Huh, D., Hamilton, G. A. and Ingber, D. E. (2011) 'From 3D cell culture to organs-on-chips', *Trends in Cell Biology*. doi: 10.1016/j.tcb.2011.09.005.
122. Hynes, R. O. and Yamada, K. M. (1982) 'Fibronectins: multifunctional modular glycoproteins.', *The Journal of cell biology*, 95(2 Pt 1), pp. 369–77. Available at: <http://www.ncbi.nlm.nih.gov/pubmed/6128348> (Accessed: 5 March 2019).
123. Jasik, A. (2012) 'Cytokeratin 7 and 20', in *Cytokeratins - Tools in Oncology*, pp. 55–66. doi: 10.5772/35246.
124. Jazayeri, M. H. *et al.* (2016) 'Various methods of gold nanoparticles (GNPs) conjugation to antibodies', *Sensing and Bio-Sensing Research*. doi: 10.1016/j.sbsr.2016.04.002.
125. Kaliberov, S. A. and Buchsbaum, D. J. (2012) 'Cancer treatment with gene therapy and radiation therapy.', *Advances in cancer research*. NIH Public Access, 115, pp. 221–63.

doi: 10.1016/B978-0-12-398342-8.00007-0.

126. Kannan, K. (2015) 'Design of Nanoparticles for Colon Target Drug Delivery – A Review Research Journal of Pharmaceutical , Biological and Chemical Sciences REVIEW ARTICLE Design of Nanoparticles for Colon Target Drug Delivery – A Review October – December', (October 2011).
127. Kaszuba, M. *et al.* (2008) 'Measuring sub nanometre sizes using dynamic light scattering', *Journal of Nanoparticle Research*. doi: 10.1007/s11051-007-9317-4.
128. Kaufman, N. *et al.* (1989) 'Remote afterloading intraluminal brachytherapy in the treatment of rectal, rectosigmoid, and anal cancer: A feasibility study', *International Journal of Radiation Oncology, Biology, Physics*. Int J Radiat Oncol Biol Phys, 17(3), pp. 663–668. doi: 10.1016/0360-3016(89)90121-1.
129. Kelly, K. L. *et al.* (2003) 'The optical properties of metal nanoparticles: The influence of size, shape, and dielectric environment', *Journal of Physical Chemistry B*. doi: 10.1021/jp026731y.
130. Kim, C. S. *et al.* (2015) 'Cellular imaging of endosome entrapped small gold nanoparticles', *MethodsX*. Elsevier, 2(6), pp. 306–315. doi: 10.1016/j.mex.2015.06.001.
131. Kim, J. Bin (2005) 'Three-dimensional tissue culture models in cancer biology', *Seminars in Cancer Biology*. doi: 10.1016/j.semcancer.2005.05.002.
132. Kim, S. and Coulombe, P. A. (2007) 'Intermediate filament scaffolds fulfill mechanical, organizational, and signaling functions in the cytoplasm', *Genes & Development*, 21(13), pp. 1581–1597. doi: 10.1101/gad.1552107.
133. Knight, E. *et al.* (2011) 'Alvetex®: Polystyrene Scaffold Technology for Routine Three Dimensional Cell Culture', in *Methods in molecular biology (Clifton, N.J.)*, pp. 323–340. doi: 10.1007/978-1-60761-984-0_20.
134. Kodiha, M. *et al.* (2015) 'Off to the organelles - killing cancer cells with targeted gold nanoparticles', *Theranostics*. Ivyspring International Publisher, pp. 357–370. doi: 10.7150/thno.10657.
135. Ku, G. Y. and Ilson, D. H. (2009) 'Role of Neoadjuvant Therapy for Esophageal Adenocarcinoma', *Surgical Oncology Clinics of North America*. doi: 10.1016/j.soc.2009.03.004.
136. Kumar, S, Aaron, J. and Sokolov, K. (2008) 'Directional conjugation of antibodies to nanoparticles for synthesis of multiplexed optical contrast agents with both delivery and targeting moieties', *Nature Protocols*. Nature Publishing Group, 3(2), pp. 314–320. doi: 10.1038/nprot.2008.1.
137. Kumar, S., Aaron, J. and Sokolov, K. (2008) 'Directional conjugation of antibodies to nanoparticles for synthesis of multiplexed optical contrast agents with both delivery and targeting moieties', *Nature Protocols*, 3(2), pp. 314–320. doi: 10.1038/nprot.2008.1.
138. Kutschka, I. *et al.* (2006) 'Collagen matrices enhance survival of transplanted cardiomyoblasts and contribute to functional improvement of ischemic rat hearts', *Circulation*. doi: 10.1161/CIRCULATIONAHA.105.001297.
139. de la Chapelle, A. and Hampel, H. (2010) 'Clinical relevance of microsatellite instability in colorectal cancer.', *Journal of clinical oncology : official journal of the American Society of Clinical Oncology*. American Society of Clinical Oncology , 28(20), pp. 3380–7. doi: 10.1200/JCO.2009.27.0652.
140. Langhans, S. A. (2018) 'Three-dimensional in vitro cell culture models in drug discovery and drug repositioning', *Frontiers in Pharmacology*. Frontiers Media SA, p. 6. doi: 10.3389/fphar.2018.00006.
141. Lapolla, A. *et al.* (1997) 'Evaluation of IgG glycation levels by matrix-assisted laser desorption/ionization mass spectrometry', *Rapid Communications in Mass Spectrometry*. Rapid Commun Mass Spectrom, 11(12), pp. 1342–1346. doi: 10.1002/(SICI)1097-0231(199708)11:12<1342::AID-RCM972>3.0.CO;2-T.

142. Lapolla, A. *et al.* (2000) 'Matrix-assisted laser desorption/ionization mass spectrometry, enzymatic digestion, and molecular modeling in the study of nonenzymatic glycation of IgG', *Journal of the American Society for Mass Spectrometry*. No longer published by Elsevier, 11(2), pp. 153–159. doi: 10.1016/S1044-0305(99)00134-8.
143. Larese Filon, F. *et al.* (2011) 'Human skin penetration of gold nanoparticles through intact and damaged skin', *Nanotoxicology*. *Nanotoxicology*, 5(4), pp. 493–501. doi: 10.3109/17435390.2010.551428.
144. Ledermann, J. A., Canevari, S. and Thigpen, T. (2015) 'Targeting the folate receptor: Diagnostic and therapeutic approaches to personalize cancer treatments', *Annals of Oncology*. doi: 10.1093/annonc/mdv250.
145. Lee, J.-S. *et al.* (2008) 'A DNA–Gold Nanoparticle-Based Colorimetric Competition Assay for the Detection of Cysteine', *Nano Letters*, 8(2), pp. 529–533. doi: 10.1021/nl0727563.
146. Levine, D. S. and Haggitt, R. C. (1989) 'Normal histology of the colon', *American Journal of Surgical Pathology*. doi: 10.1097/00000478-198911000-00008.
147. Lévy, R. *et al.* (2010) 'Gold nanoparticles delivery in mammalian live cells: a critical review', *Nano Reviews*. Taylor & Francis, 1(1), p. 4889. doi: 10.3402/nano.v1i0.4889.
148. Lewis, E. E. L. *et al.* (2016) 'A Quiescent, Regeneration-Responsive Tissue Engineered Mesenchymal Stem Cell Bone Marrow Niche Model via Magnetic Levitation', *ACS Nano*. doi: 10.1021/acsnano.6b02841.
149. Lewis, N. S. *et al.* (2017) 'Magnetically levitated mesenchymal stem cell spheroids cultured with a collagen gel maintain phenotype and quiescence', *Journal of Tissue Engineering*. doi: 10.1177/2041731417704428.
150. Li, C. H. *et al.* (2015) 'Gold nanoparticles increase endothelial paracellular permeability by altering components of endothelial tight junctions, and increase blood-brain barrier permeability in mice', *Toxicological Sciences*. doi: 10.1093/toxsci/kfv176.
151. Li, J. L. *et al.* (2009) 'In vitro cancer cell imaging and therapy using transferrin-conjugated gold nanoparticles', *Cancer Letters*. doi: 10.1016/j.canlet.2008.09.024.
152. Li, Q. *et al.* (2011) '3D models of epithelial-mesenchymal transition in breast cancer metastasis: High-throughput screening assay development, validation, and pilot screen', *Journal of Biomolecular Screening*. doi: 10.1177/1087057110392995.
153. Linger, R. M. A. *et al.* (2008) 'TAM Receptor Tyrosine Kinases: Biologic Functions, Signaling, and Potential Therapeutic Targeting in Human Cancer', *Advances in Cancer Research*. *Adv Cancer Res*, pp. 35–83. doi: 10.1016/S0065-230X(08)00002-X.
154. Liu, H., Lv, L. and Yang, K. (2015) 'Chemotherapy targeting cancer stem cells.', *American journal of cancer research*. e-Century Publishing Corporation, 5(3), pp. 880–93. Available at: <http://www.ncbi.nlm.nih.gov/pubmed/26045975> (Accessed: 28 November 2018).
155. Ljungblad, J. (2009) 'Antibody-conjugated Gold Nanoparticles integrated in a fluorescence based Biochip'. Available at: <http://www.diva-portal.org/smash/record.jsf?pid=diva2%3A271859&dswid=5275> (Accessed: 23 January 2019).
156. Lovitt, C., Shelper, T. and Avery, V. (2014) 'Advanced Cell Culture Techniques for Cancer Drug Discovery', *Biology*. doi: 10.3390/biology3020345.
157. Low, P. S. and Kularatne, S. A. (2009) 'Folate-targeted therapeutic and imaging agents for cancer', *Current Opinion in Chemical Biology*. doi: 10.1016/j.cbpa.2009.03.022.
158. Lu, P., Weaver, V. M. and Werb, Z. (2012) 'The extracellular matrix: A dynamic niche in cancer progression', *Journal of Cell Biology*. doi: 10.1083/jcb.201102147.
159. Lund, T. *et al.* (2011) 'The influence of ligand organization on the rate of uptake of gold nanoparticles by colorectal cancer cells', *Biomaterials*. Centre for Investigative and Diagnostic Oncology, Department of Natural Sciences, School of Health and Social Sciences,

- Middlesex University, The Burroughs, London NW4 4BT, UK. t.lund@mdx.ac.uk: Elsevier Ltd, 32(36), pp. 9776–9784. doi: 10.1016/j.biomaterials.2011.09.018 [doi].
160. Maeda, H. (2001) ‘The enhanced permeability and retention (EPR) effect in tumor vasculature: the key role of tumor-selective macromolecular drug targeting’, *Advances in Enzyme Regulation*. Department of Microbiology, Kumamoto University School of Medicine, 860-0811, Kumamoto, Japan. msmaedah@gpo.kumamoto-u.ac.jp, 41, pp. 189–207. doi: S0065257100000133 [pii].
 161. De Maio, G. *et al.* (2014) ‘Circulating and stool nucleic acid analysis for colorectal cancer diagnosis.’, *World journal of gastroenterology*. Baishideng Publishing Group Inc, 20(4), pp. 957–67. doi: 10.3748/wjg.v20.i4.957.
 162. Mandel, J. S. *et al.* (1993) ‘Reducing Mortality from Colorectal Cancer by Screening for Fecal Occult Blood’, *New England Journal of Medicine*, 328(19), pp. 1365–1371. doi: 10.1056/NEJM199305133281901.
 163. Marijnen, C. A. M. *et al.* (2002) ‘Acute Side Effects and Complications After Short-Term Preoperative Radiotherapy Combined With Total Mesorectal Excision in Primary Rectal Cancer: Report of a Multicenter Randomized Trial’, *Journal of Clinical Oncology*, 20(3), pp. 817–825. doi: 10.1200/JCO.2002.20.3.817.
 164. Marquis, B. J. *et al.* (2009) ‘Analytical methods to assess nanoparticle toxicity’, *Analyst*. doi: 10.1039/b818082b.
 165. Martínez, J. C. *et al.* (2012) ‘Alternative Methodology for Gold Nanoparticles Diameter Characterization Using PCA Technique and UV-VIS Spectrophotometry’, 2(6), pp. 184–189. doi: 10.5923/j.nn.20120206.06.
 166. Massaro, E. J. and Rogers, J. M. (2002) *Folate and Human Development, Folate and Human Development*. Humana Press. doi: 10.1385/1592591647.
 167. Mathias, R. A. *et al.* (2012) ‘Two Distinct Populations of Exosomes Are Released from LIM1863 Colon Carcinoma Cell-derived Organoids’, *Molecular & Cellular Proteomics*. doi: 10.1074/mcp.m112.021303.
 168. Mayorova, O. A. *et al.* (2020) ‘Endovascular addressing improves the effectiveness of magnetic targeting of drug carrier. Comparison with the conventional administration method’, *Nanomedicine: Nanotechnology, Biology, and Medicine*. Nanomedicine, 28. doi: 10.1016/j.nano.2020.102184.
 169. Moll, R. *et al.* (1982) ‘The catalog of human cytokeratins: Patterns of expression in normal epithelia, tumors and cultured cells’, *Cell*. doi: 10.1016/0092-8674(82)90400-7.
 170. Moll, R. *et al.* (1992) ‘Cytokeratin 20 in human carcinomas. A new histodiagnostic marker detected by monoclonal antibodies.’, *The American journal of pathology*.
 171. Mueller-Klieser, W. (1987) ‘Multicellular spheroids - A review on cellular aggregates in cancer research’, *Journal of Cancer Research and Clinical Oncology*. doi: 10.1007/BF00391431.
 172. Mukherjee, P., Bhattacharya, R. and Mukhopadhyay, D. (2006) ‘Gold Nanoparticles Bearing Functional Anti-Cancer Drug and Anti-Angiogenic Agent: A “2 in 1” System with Potential Application in Cancer Therapeutics’, *Journal of Biomedical Nanotechnology*. doi: 10.1166/jbn.2005.016.
 173. Murphy, C. J. *et al.* (2008) ‘Chemical sensing and imaging with metallic nanorods’, *Chemical Communications*. doi: 10.1039/b711069c.
 174. Murray, C. B., Kagan, C. R. and Bawendi, M. G. (2000) ‘Synthesis and characterization of monodisperse nanocrystals and close-packed nanocrystal assemblies’, *Annual Review of Materials Science*. Annual Reviews 4139 El Camino Way, P.O. Box 10139, Palo Alto, CA 94303-0139, USA, 30, pp. 545–610. doi: 10.1146/annurev.matsci.30.1.545.
 175. Mylonas, C. C. and Lazaris, A. C. (2014) ‘Colorectal Cancer and Basement Membranes: Clinicopathological Correlations’, *Gastroenterology Research and Practice*.

doi: 10.1155/2014/580159.

176. Nativo, P., Prior, I. A. and Brust, M. (2008) 'Uptake and intracellular fate of surface-modified gold nanoparticles', *ACS Nano*. doi: 10.1021/nn800330a.
177. Naz, F. *et al.* (2016) 'Biokinetics of ultrafine gold nanoparticles (AuNPs) relating to redistribution and urinary excretion: A long-term in vivo study', *Journal of Drug Targeting*. doi: 10.3109/1061186X.2016.1144758.
178. Niessen, R. C. *et al.* (2009) 'Germline hypermethylation of *MLH1* and *EPCAM* deletions are a frequent cause of Lynch syndrome', *Genes, Chromosomes and Cancer*, 48(8), pp. 737–744. doi: 10.1002/gcc.20678.
179. Nugent, K. P. and Phillips, R. K. S. (1992) 'Rectal cancer risk in older patients with familial adenomatous polyposis and an ileorectal anastomosis: a cause for concern', *British Journal of Surgery*, 79(11), pp. 1204–1206. doi: 10.1002/bjs.1800791136.
180. Omary, M. B. *et al.* (2009) 'Toward unraveling the complexity of simple epithelial keratins in human disease', *Journal of Clinical Investigation*, 119(7), pp. 1794–1805. doi: 10.1172/JCI37762.
181. Orgel, J. P. R. O., Persikov, A. V. and Antipova, O. (2014) 'Variation in the helical structure of native collagen', *PLoS ONE*. doi: 10.1371/journal.pone.0089519.
182. Oriolo, A. S. *et al.* (2007) 'Intermediate filaments: A role in epithelial polarity', *Experimental Cell Research*. doi: 10.1016/j.yexcr.2007.02.030.
183. Osborn, N. K. and Ahlquist, D. A. (2005) 'Stool screening for colorectal cancer: molecular approaches.', *Gastroenterology*, 128(1), pp. 192–206. Available at: <http://www.ncbi.nlm.nih.gov/pubmed/15633136> (Accessed: 20 November 2018).
184. Ouyang, B. *et al.* (2020) 'The dose threshold for nanoparticle tumour delivery', *Nature Materials*. doi: 10.1038/s41563-020-0755-z.
185. Ozburn, M. A. and Patterson, N. A. (2014) 'Using organotypic (raft) epithelial tissue cultures for the biosynthesis and isolation of infectious human papillomaviruses', *Current Protocols in Microbiology*. doi: 10.1002/9780471729259.mc14b03s34.
186. Pal, S., Tak, Y. K. and Song, J. M. (2015) 'Does the antibacterial activity of silver nanoparticles depend on the shape of the nanoparticle? A study of the gram-negative bacterium *Escherichia coli*', *Journal of Biological Chemistry*. doi: 10.1128/AEM.02218-06.
187. Pampaloni, F., Reynaud, E. G. and Stelzer, E. H. K. (2007) 'The third dimension bridges the gap between cell culture and live tissue', *Nature Reviews Molecular Cell Biology*. doi: 10.1038/nrm2236.
188. Pan, Y. *et al.* (2007) 'Size-dependent cytotoxicity of gold nanoparticles', *Small*. doi: 10.1002/sml.200700378.
189. Pan, Y. *et al.* (2014) 'Gold nanoparticles inhibit VEGF165-induced migration and tube formation of endothelial cells via the Akt pathway', *BioMed Research International*. doi: 10.1155/2014/418624.
190. Park, S. Y. *et al.* (2007) 'Panels of immunohistochemical markers help determine primary sites of metastatic adenocarcinoma', *Archives of Pathology and Laboratory Medicine*. doi: 10.1043/1543-2165(2007)131[1561:POIMHD]2.0.CO;2.
191. Pastuszak, Marek *et al.* (2015) 'Cytokeratins in gastroenterology. Systematic review', *Gastroenterology Review*, 2(2), pp. 61–70. doi: 10.5114/pg.2015.51182.
192. Patel, R. (2015) 'MALDI-TOF MS for the Diagnosis of Infectious Diseases', *Clinical Chemistry*, 61(1), pp. 100–111. doi: 10.1373/clinchem.2014.221770.
193. Patra, C. R. *et al.* (2008) 'Targeted delivery of gemcitabine to pancreatic adenocarcinoma using cetuximab as a targeting agent', *Cancer research*. Department of Biochemistry and Molecular Biology, Mayo Clinic, Rochester, MN 55905, USA., 68(6), pp. 1970–1978. doi: 10.1158/0008-5472.CAN-07-6102 [doi].
194. Patra, C. R. *et al.* (2010) 'Fabrication of gold nanoparticles for targeted therapy in pancreatic cancer', *Advanced Drug Delivery Reviews*. doi: 10.1016/j.addr.2009.11.007.

195. Patra, J. K. *et al.* (2018) 'Nano based drug delivery systems: Recent developments and future prospects 10 Technology 1007 Nanotechnology 03 Chemical Sciences 0306 Physical Chemistry (incl. Structural) 03 Chemical Sciences 0303 Macromolecular and Materials Chemistry 11 Medical and He', *Journal of Nanobiotechnology*. BioMed Central, pp. 1–33. doi: 10.1186/s12951-018-0392-8.
196. Price, K. J. *et al.* (2012) 'Matrigel Basement Membrane Matrix influences expression of microRNAs in cancer cell lines', *Biochemical and Biophysical Research Communications*. doi: 10.1016/j.bbrc.2012.09.059.
197. R., S. *et al.* (2016) 'TAM receptors Tyro3 and Mer as novel targets in colorectal cancer', *Oncotarget*. doi: 10.18632/oncotarget.10889.
198. Radtke, F. and Clevers, H. (2005) 'Self-renewal and cancer of the gut: Two sides of a coin', *Science*. doi: 10.1126/science.1104815.
199. Rane, T. D. and Armani, A. M. (2016) 'Two-photon microscopy analysis of gold nanoparticle uptake in 3D cell spheroids', *PLoS ONE*. doi: 10.1371/journal.pone.0167548.
200. Raouf, M. *et al.* (2012) 'Stability of antibody-conjugated gold nanoparticles in the endolysosomal nanoenvironment: Implications for noninvasive radiofrequency-based cancer therapy', *Nanomedicine: Nanotechnology, Biology, and Medicine*, 8(7), pp. 1096–1105. doi: 10.1016/j.nano.2012.02.001.
201. Rayavarapu, R. G. *et al.* (2007) 'Synthesis and bioconjugation of gold nanoparticles as potential molecular probes for light-based imaging techniques.', *International journal of biomedical imaging*. Hindawi, 2007, p. 29817. doi: 10.1155/2007/29817.
202. Resemann, A. *et al.* (2010) 'Top-down de novo protein sequencing of a 13.6 kDa camelid single heavy chain antibody by matrix-assisted laser desorption ionization-time-of-flight/ time-of-flight mass spectrometry', *Analytical Chemistry*. American Chemical Society, 82(8), pp. 3283–3292. doi: 10.1021/ac1000515.
203. Robichaux Viehoever, A. *et al.* (2004) 'Organotypic Raft Cultures as an Effective In Vitro Tool for Understanding Raman Spectral Analysis of Tissue¶', *Photochemistry and Photobiology*. doi: 10.1562/0031-8655(2003)078<0517:orcaae>2.0.co;2.
204. Rougier, P. *et al.* (1998) 'Randomised trial of irinotecan versus fluorouracil by continuous infusion after fluorouracil failure in patients with metastatic colorectal cancer.', *Lancet (London, England)*. Elsevier, 352(9138), pp. 1407–12. doi: 10.1016/S0140-6736(98)03085-2.
205. Rowe, R. G. and Weiss, S. J. (2009) 'Navigating ECM Barriers at the Invasive Front: The Cancer Cell–Stroma Interface', *Annual Review of Cell and Developmental Biology*. doi: 10.1146/annurev.cellbio.24.110707.175315.
206. Rullier, A. *et al.* (2000) 'Cytokeratin 7 and 20 expression in cholangiocarcinomas varies along the biliary tract but still differs from that in colorectal carcinoma metastasis.', *The American journal of surgical pathology*, 24(6), pp. 870–6. Available at: <http://www.ncbi.nlm.nih.gov/pubmed/10843291> (Accessed: 21 January 2019).
207. Saad, R. S. *et al.* (2009) 'CDX2, cytokeratins 7 and 20 immunoreactivity in rectal adenocarcinoma', *Applied Immunohistochemistry and Molecular Morphology*. doi: 10.1097/PAI.0b013e31819268f2.
208. Sabharanjak, S. and Mayor, S. (2004) 'Folate receptor endocytosis and trafficking', *Advanced Drug Delivery Reviews*. Adv Drug Deliv Rev, 56(8), pp. 1099–1109. doi: 10.1016/j.addr.2004.01.010.
209. Samadian, H. *et al.* (2016) 'Folate-conjugated gold nanoparticle as a new nanoplatform for targeted cancer therapy', *Journal of Cancer Research and Clinical Oncology*, 142(11), pp. 2217–2229. doi: 10.1007/s00432-016-2179-3.
210. Schmidt, T. *et al.* (2012) 'Macrophage-tumor crosstalk: Role of TAMR tyrosine kinase receptors and of their ligands', *Cellular and Molecular Life Sciences*, 69(9), pp. 1391–1414. doi: 10.1007/s00018-011-0863-7.

211. Schmitz, R. *et al.* (2016) ‘TAM receptors Tyro3 and Mer as novel targets in colorectal cancer’, *Oncotarget*. Impact Journals LLC, 7(35), pp. 56355–56370. doi: 10.18632/oncotarget.10889.
212. Segal, E. I. and Low, P. S. (2008) ‘Tumor detection using folate receptor-targeted imaging agents’, *Cancer and Metastasis Reviews*. doi: 10.1007/s10555-008-9155-6.
213. Seung, S. J. *et al.* (2005) ‘Structures and properties of self-assembled monolayers of bistable [2]rotaxanes on Au (111) surfaces from molecular dynamics simulations validated with experiment’, *Journal of the American Chemical Society*. American Chemical Society, 127(5), pp. 1563–1575. doi: 10.1021/ja044530x.
214. Seymour, M. T. *et al.* (2007) ‘Different strategies of sequential and combination chemotherapy for patients with poor prognosis advanced colorectal cancer (MRC FOCUS): a randomised controlled trial’, *Lancet*. Lancet, 370(9582), pp. 143–152. doi: 10.1016/S0140-6736(07)61087-3.
215. Shen, F. *et al.* (1994) ‘Identification of a Novel Folate Receptor, a Truncated Receptor, and Receptor Type β in Hematopoietic Cells: cDNA Cloning, Expression, Immunoreactivity, and Tissue Specificity’, *Biochemistry*. American Chemical Society, 33(5), pp. 1209–1215. doi: 10.1021/bi00171a021.
216. Shen, J. *et al.* (2015) ‘Assessment of folate receptor-beta expression in human neoplastic tissues’, *Oncotarget*, 6(16), pp. 14700–14709. doi: 10.18632/oncotarget.3739.
217. Shen, J. *et al.* (2017) ‘Assessment of folate receptor alpha and beta expression in selection of lung and pancreatic cancer patients for receptor targeted therapies’, *Oncotarget*. doi: 10.18632/oncotarget.23321.
218. Shia, J. *et al.* (2008) ‘Immunohistochemical expression of folate receptor α in colorectal carcinoma: patterns and biological significance’, *Human Pathology*. doi: 10.1016/j.humpath.2007.09.013.
219. Shield, K. *et al.* (2009) ‘Multicellular spheroids in ovarian cancer metastases: Biology and pathology’, *Gynecologic Oncology*. doi: 10.1016/j.ygyno.2008.11.032.
220. Shimura, T. (2011) ‘Acquired radioresistance of cancer and the AKT/GSK3 β /cyclin D1 overexpression cycle.’, *Journal of radiation research*, 52(5), pp. 539–44. Available at: <http://www.ncbi.nlm.nih.gov/pubmed/21881296> (Accessed: 28 November 2018).
221. Signor, L. and Erba, E. B. (2013) ‘Matrix-assisted laser desorption/ionization time of flight (MALDI-TOF) mass spectrometric analysis of intact proteins larger than 100 kDa’, *Journal of Visualized Experiments*. Journal of Visualized Experiments, (79). doi: 10.3791/50635.
222. Singh, M. *et al.* (2015) ‘Application of gold nanoparticles for gastrointestinal cancer theranostics: A systematic review’, *Nanomedicine : nanotechnology, biology, and medicine*. Hamlyn Centre for Robotic Surgery, Department of Surgery & Cancer, Imperial College London, London, UK.; Hamlyn Centre for Robotic Surgery, Department of Surgery & Cancer, Imperial College London, London, UK.; Hamlyn Centre for Robotic Surgery, Department: The Authors. Published by Elsevier Inc, 11(8), pp. 2083–2098. doi: 10.1016/j.nano.2015.05.010 [doi].
223. Singhal, N. *et al.* (2015) ‘MALDI-TOF mass spectrometry: an emerging technology for microbial identification and diagnosis.’, *Frontiers in microbiology*. Frontiers Media SA, 6, p. 791. doi: 10.3389/fmicb.2015.00791.
224. Sperling, R. A. *et al.* (2008) ‘Biological applications of gold nanoparticles’, *Chemical Society Reviews*. The Royal Society of Chemistry, pp. 1896–1908. doi: 10.1039/b712170a.
225. Sperling, R. A. and Parak, W. J. (2010) ‘Surface modification, functionalization and bioconjugation of colloidal inorganic nanoparticles’, *Philosophical Transactions of the Royal Society A: Mathematical, Physical and Engineering Sciences*. The Royal Society Publishing, 368(1915), pp. 1333–1383. doi: 10.1098/rsta.2009.0273.
226. Stitt, T. N. *et al.* (1995) ‘The anticoagulation factor protein S and its relative, Gas6,

- are ligands for the Tyro 3/Axl family of receptor tyrosine kinases.’, *Cell*, 80(4), pp. 661–70. Available at: <http://www.ncbi.nlm.nih.gov/pubmed/7867073> (Accessed: 6 January 2019).
227. Stojanovska, V., Sakkal, S. and Nurgali, K. (2015) ‘Platinum-based chemotherapy: gastrointestinal immunomodulation and enteric nervous system toxicity’, *American Journal of Physiology-Gastrointestinal and Liver Physiology*, 308(4), pp. G223–G232. doi: 10.1152/ajpgi.00212.2014.
228. Sutherland, R. M. (1988) ‘Cell and environment interactions in tumor microregions: The multicell spheroid model’, *Science*. doi: 10.1126/science.2451290.
229. Tam, S. Y. and Wu, V. W. C. (2019) ‘A review on the special radiotherapy techniques of colorectal cancer’, *Frontiers in Oncology*. Frontiers Media SA, p. 208. doi: 10.3389/fonc.2019.00208.
230. Tariq, K. *et al.* (2016) ‘Colorectal cancer carcinogenesis: a review of mechanisms’, *Cancer Biology & Medicine*. doi: 10.20892/j.issn.2095-3941.2015.0103.
231. Taylor, I. C. A. *et al.* (1995) ‘Mouse mammary tumors express elevated levels of RNA encoding the murine homolog of SKY, a putative receptor tyrosine kinase’, *Journal of Biological Chemistry*, 270(12), pp. 6872–6880. doi: 10.1074/jbc.270.12.6872.
232. Taylor, I. C., Roy, S. and Varmus, H. E. (1995) ‘Overexpression of the Sky receptor tyrosine kinase at the cell surface or in the cytoplasm results in ligand-independent activation.’, *Oncogene*, 11(12), pp. 2619–26. Available at: <http://www.ncbi.nlm.nih.gov/pubmed/8545119> (Accessed: 6 January 2019).
233. Tazawa, Y. *et al.* (2014) ‘Schedule-dependent cytotoxicity of Etoposide and cyclophosphamide in P-glycoprotein-expressing human leukemic K-562 cells.’, *Biological & pharmaceutical bulletin*, 37(8), pp. 1323–9. Available at: <http://www.ncbi.nlm.nih.gov/pubmed/25087953> (Accessed: 28 November 2018).
234. Thomas, D. C., Umar, A. and Kunkel, T. A. (1996) ‘Microsatellite instability and mismatch repair defects in cancer.’, *Mutation research*, 350(1), pp. 201–5. Available at: <http://www.ncbi.nlm.nih.gov/pubmed/8657182> (Accessed: 13 November 2018).
235. Tibbitt, M. W. and Anseth, K. S. (2009) ‘Hydrogels as extracellular matrix mimics for 3D cell culture’, *Biotechnology and Bioengineering*. doi: 10.1002/bit.22361.
236. Tkachenko, A. G. *et al.* (2004) ‘Cellular trajectories of peptide-modified gold particle complexes: Comparison of nuclear localization signals and peptide transduction domains’, *Bioconjugate Chemistry*, 15(3), pp. 482–490. doi: 10.1021/bc034189q.
237. Tlsty, T. D. and Coussens, L. M. (2006) ‘TUMOR STROMA AND REGULATION OF CANCER DEVELOPMENT’, *Annual Review of Pathology: Mechanisms of Disease*. doi: 10.1146/annurev.pathol.1.110304.100224.
238. Tlsty, T. D. and Hein, P. W. (2001) ‘Know thy neighbor: Stromal cells can contribute oncogenic signals’, *Current Opinion in Genetics and Development*. doi: 10.1016/S0959-437X(00)00156-8.
239. Tripathi, K. and Driskell, J. D. (2018) ‘Quantifying Bound and Active Antibodies Conjugated to Gold Nanoparticles: A Comprehensive and Robust Approach to Evaluate Immobilization Chemistry’, *ACS Omega*, 3(7), pp. 8253–8259. doi: 10.1021/acsomega.8b00591.
240. Turkevich, J., Stevenson, P. C. and Hillier, J. (1951) ‘A study of the nucleation and growth processes in the synthesis of colloidal gold’, *Discussions of the Faraday Society*. The Royal Society of Chemistry, 11(0), pp. 55–75. Available at: <http://dx.doi.org/10.1039/DF9511100055>.
241. Uitto, J., Olsen, D. R. and Fazio, M. J. (1989) ‘Extracellular matrix of the skin: 50 years of progress.’, *The Journal of investigative dermatology*, 92(4f), pp. 61–77. Available at: <http://www.ncbi.nlm.nih.gov/pubmed/2649616> (Accessed: 5 March 2019).
242. Volk-Draper, L. *et al.* (2014) ‘Paclitaxel therapy promotes breast cancer metastasis in a TLR4-dependent manner’, *Cancer Research*. doi: 10.1158/0008-5472.CAN-14-0067.

243. Wang, A. Z., Langer, R. and Farokhzad, O. C. (2012) 'Nanoparticle Delivery of Cancer Drugs', *Annual Review of Medicine*, 63(1), pp. 185–198. doi: 10.1146/annurev-med-040210-162544.
244. Wangoo, N. *et al.* (2008) 'Synthesis and capping of water-dispersed gold nanoparticles by an amino acid: Bioconjugation and binding studies', *Journal of Colloid and Interface Science*. doi: 10.1016/j.jcis.2008.04.043.
245. Watt, F. M. and Fujiwara, H. (2011) 'Cell-extracellular matrix interactions in normal and diseased skin.', *Cold Spring Harbor perspectives in biology*. Cold Spring Harbor Laboratory Press, 3(4), pp. 1–14. doi: 10.1101/cshperspect.a005124.
246. Weber, L. *et al.* (1984) 'Collagen type distribution and macromolecular organization of connective tissue in different layers of human skin', *Journal of Investigative Dermatology*, 82, pp. 156–160. doi: 10.1111/1523-1747.ep12259720.
247. Weeber, F. *et al.* (2017) 'Tumor Organoids as a Pre-clinical Cancer Model for Drug Discovery', *Cell Chemical Biology*. doi: 10.1016/j.chembiol.2017.06.012.
248. Weinstein, G. D. and Boucek, R. J. (1960) 'Collagen and elastin of human dermis.', *The Journal of investigative dermatology*. Elsevier, 35(4), pp. 227–229. doi: 10.1038/jid.1960.109.
249. Wibowo, A. S. *et al.* (2013) 'Structures of human folate receptors reveal biological trafficking states and diversity in folate and antifolate recognition', *Proceedings of the National Academy of Sciences of the United States of America*. National Academy of Sciences, 110(38), pp. 15180–15188. doi: 10.1073/pnas.1308827110.
250. Wilhelm, S. *et al.* (2016) 'Analysis of nanoparticle delivery to tumours', *Nature Reviews Materials*. Nature Publishing Group, 1(5), pp. 1–12. doi: 10.1038/natrevmats.2016.14.
251. Willets, K. A. and Van Duyne, R. P. (2007) 'Localized Surface Plasmon Resonance Spectroscopy and Sensing', *Annual Review of Physical Chemistry*. doi: 10.1146/annurev.physchem.58.032806.104607.
252. Wolf, A. M. D. *et al.* (2018) 'Colorectal cancer screening for average-risk adults: 2018 guideline update from the American Cancer Society', *CA: A Cancer Journal for Clinicians*. American Cancer Society, 68(4), pp. 250–281. doi: 10.3322/caac.21457.
253. Wolpin, B. M. and Mayer, R. J. (2008) 'Systemic Treatment of Colorectal Cancer', *Gastroenterology*, 134(5), pp. 1296-1310.e1. doi: 10.1053/j.gastro.2008.02.098.
254. Wong, C. *et al.* (2011) 'Multistage nanoparticle delivery system for deep penetration into tumor tissue', *Proceedings of the National Academy of Sciences*. National Academy of Sciences, 108(6), pp. 2426–2431. doi: 10.1073/pnas.1018382108.
255. Worthington, P., Pochan, D. J. and Langhans, S. A. (2015) 'Peptide Hydrogels – Versatile Matrices for 3D Cell Culture in Cancer Medicine', *Frontiers in Oncology*. doi: 10.3389/fonc.2015.00092.
256. Worthley, D. L., Giraud, A. S. and Wang, T. C. (2010) 'The extracellular matrix in digestive cancer', in *Cancer Microenvironment*. Springer, pp. 177–185. doi: 10.1007/s12307-010-0053-4.
257. Xie, Y.-H., Chen, Y.-X. and Fang, J.-Y. (2020) 'Comprehensive review of targeted therapy for colorectal cancer', *Signal Transduction and Targeted Therapy* 2020 5:1. Nature Publishing Group, 5(1), pp. 1–30. doi: 10.1038/s41392-020-0116-z.
258. Xu, X. *et al.* (2012) 'Recreating the tumor microenvironment in a bilayer, hyaluronic acid hydrogel construct for the growth of prostate cancer spheroids', *Biomaterials*. doi: 10.1016/j.biomaterials.2012.08.061.
259. Yamada, K. M. and Cukierman, E. (2007) 'Modeling Tissue Morphogenesis and Cancer in 3D', *Cell*. doi: 10.1016/j.cell.2007.08.006.
260. Yamagata, M., Sanes, J. R. and Weiner, J. A. (2003) 'Synaptic adhesion molecules', *Current Opinion in Cell Biology*. Elsevier Current Trends, pp. 621–632. doi: 10.1016/S0955-

0674(03)00107-8.

261. Yamauchi, M. *et al.* (2012) ‘Colorectal cancer: A tale of two sides or a continuum?’, *Gut*. doi: 10.1136/gutjnl-2012-302014.
262. Yan, C. and Pochan, D. J. (2010) ‘Rheological properties of peptide-based hydrogels for biomedical and other applications’, *Chemical Society Reviews*. doi: 10.1039/b919449p.
263. Yang, P. H. *et al.* (2005) ‘Transferrin-mediated gold nanoparticle cellular uptake’, *Bioconjugate Chemistry*, 16(3), pp. 494–496. doi: 10.1021/bc049775d.
264. Yang, W. *et al.* (2019) ‘Gold nanoparticle based photothermal therapy: Development and application for effective cancer treatment’, *Sustainable Materials and Technologies*. Elsevier B.V., 22, p. e00109. doi: 10.1016/j.susmat.2019.e00109.
265. Yip, D. and Cho, C. H. (2013) ‘A multicellular 3D heterospheroid model of liver tumor and stromal cells in collagen gel for anti-cancer drug testing’, *Biochemical and Biophysical Research Communications*. doi: 10.1016/j.bbrc.2013.03.008.
266. Young, A. M. (Annie M., Hobbs, R. and Kerr, D. J. (2011) *ABC of colorectal cancer*. Wiley-Blackwell. Available at: <https://www.wiley.com/en-us/ABC+of+Colorectal+Cancer%2C+2nd+Edition-p-9781405177634> (Accessed: 11 November 2018).
267. Yu, M. K., Park, J. and Jon, S. (2012) ‘Magnetic nanoparticles and their applications in image-guided drug delivery’, *Drug Delivery and Translational Research*. Springer US, 2(1), pp. 3–21. doi: 10.1007/s13346-011-0049-8.
268. Yue, J. *et al.* (2017) ‘Gold Nanoparticle Size and Shape Effects on Cellular Uptake and Intracellular Distribution of siRNA Nanoconstructs’, *Bioconjugate Chemistry*. doi: 10.1021/acs.bioconjchem.7b00252.
269. Zhang, F. *et al.* (2007) ‘Gold nanoparticles decorated with oligo(ethylene glycol) thiols: Protein resistance and colloidal stability’, *Journal of Physical Chemistry A*. doi: 10.1021/jp074293v.
270. Zhang, Z. *et al.* (2010) ‘Conjugating folic acid to gold nanoparticles through glutathione for targeting and detecting cancer cells’, *Bioorganic and Medicinal Chemistry*, 18(15), pp. 5528–5534. doi: 10.1016/j.bmc.2010.06.045.